Impact of Macromolecular Design on Self-assembly Properties of Block copolymers: Effect of Tunable Chain Flexibility and Chain Topology

A Dissertation Presented for the

Doctor of Philosophy

Degree

The University of Tennessee, Knoxville

Kamlesh Ramesh Bornani

May 2017

Copyright © 2017 by Kamlesh Bornani

All rights reserved.

Dedication

This dissertation is dedicated to my loving parents, Ramesh and Sushma Bornani, my sister Monika Bornani, and my lovely niece Sia Bornani.

Acknowledgements

Foremost, I would like to express my sincere gratitude to my advisor Prof. S. Michael Kilbey II. His constant support and mentoring has helped me become a critical thinker, and an responsible researcher with improved problem-solving and communication skills. His open mindedness and availability for communication created a well-balanced environment for nurturing me as scientist. I will be forever grateful for his eagerness in providing guidance to deal with problems, both technical and personal. Under his strong mentorship, I feel confident as a polymer scientist, ready to tackle future challenges.

Second, I would like to acknowledge my family's valuable contribution through constant support and love they have provided in the past five years. Without their sacrifices and support, my aspiration to gain higher education (Ph.D.) would be have been impossible to achieve. Their help and presence, both financial and emotional in all these years I spent away from them have been extremely valuable in each and every step forward.

This acknowledgment would be incomplete without the mention of my colleagues here at UT. With them, I have had an opportunity to interact on both personal and professional level, which made these stressful years more bearable. My special thanks to Jesse Davis, Bethany Aden, W. Michael Kochemba and Xu Wang, with whom I shared a great rapport throughout graduate studies.

I extend my gratitude to Prof. Jimmy Mays and all the helpful people in his lab, including Kostas Misichronis, Weiyu Wang, Priyank Shah and Nam Goo Kang. Apart from their expertise,

they have never held back from sharing knowledge and helping me in various situations. Special thanks goes to Weiyu Wang, who agreed to synthesize materials that formed a major part of the characterization work I conducted in this dissertation.

Being part of the Kilbey group, I had ample of opportunities to interact and collaborate with experts at Center for Nanophase Material Sciences (CNMS). All the collaborators and staff were very helpful in providing access to the facilities and guidance at various times. These people include Bradley Lokitz, Balaka Barkakaty, David Uhrig, Jamie Messman, Deana Pickel, Suk-kyun Ahn and Juan Pablo Hinestrosa. I would like to make a special mention about Balaka, whose advice on both professional and personal life helped me get through some rough times. I wish her the very best in her future endeavors!

Some of our friends from UT and other universities have their share of professional contributions. Dr. John Dunlap of the Advanced Microscopy and Imaging Center at The University of Tennessee-Knoxville is gratefully acknowledged for his assistance with transmission electron microscopy training and imaging. Professor Paul Russo is thanked for helpful discussions on light scattering. Dr. Frederick Beyer at the Army Research Laboratories is acknowledged for inviting me to learn some TEM techniques. Professor Darrin Pochan from University of Delaware is also thanked for helpful discussions on Cryo-TEM sample preparation in the early stages of my graduate career.

These five years were a lot of fun, especially in the company of friends from various diverse cultures. Special mention to Jesse Davis for being there and providing encouragement during rough times which proved valuable, and also for some unforgettable memories we made

in our extra-curricular endeavors outside the lab! This acknowledgement would be incomplete without mentioning my group members, both past and present, including Chaitra Deodhar, Camille Kite, Dayton Street, Rachel Ramirez, Zach Siebers, Sina Sabury, Evan Boone, Jiadi Hou and Graham Collier. Thank you for all the support and making me feel at home.

Some friends with whom I shared good memories in Knoxville include Gurudatt, Rahul Soni, Bharadwaj Venkatesan, Ninad Pradhan, Kaveri Thakur, Snigdha Sewlikar, Guruanand Venkatesan, Chaitanya Mehta, Siddheshvar Bhela, Abhay Pande, Karan Kapoor, Ramya Rao Enganti and Samyuckta Kadiresan.

Finally, I would like to sincerely acknowledge the financial support from the National Science Foundation (Award #1512221) and U.S. Army Research Office (Award #59668CH) without which the research would not have been possible.

Abstract

The generation of well-ordered complex structures from constituent block copolymeric building blocks by the spontaneous process of self-assembly is useful in various technologies. The well-defined 3D structures are dictated by complex energetic interplays and their shape is controllable by both preparative conditions and macromolecular design. This dissertation work aims at exploring the effect of chain flexibility and chain topology design changes on phase behavior of block copolymers in solution. Further, we exploit the tunable flexibility of the semiflexible polymers in studying dispersion and controlling macroscale thermal properties in polymer nanocomposites.

The experimental design is based on two model systems: The first is based on polystyrene-b-poly1,3-cyclohexadiene (PS-b-PCHD). Here, the semiflexible nature of PCHD is tunable through alteration in the chain microstructure of the polymer backbone. As altered flexibility impacts the ability of chains to pack, which is shown to affect micelle morphology in solution. Further, we exploit the entropic contributions due to changes in chain configuration of PCHD (controlled through microstructure to control the dispersion of silica nanoparticles in matrices varying flexibility. Because we leave the monomer type unchanged, studying PCHD-based materials enables us to draw links between chain configuration and phase behavior. The second system is based on polystyrene-polyisoprene, (PS-PI), where multiple star copolymers were studied in a PI selective solvent. The study highlights how architecture and composition influence self-organization of the topologically-complex polymers in solution. The topological constraints introduced through architecture and composition were unable to induce any

morphological changes, however design variation was successful in inducing changes in micelle size.

These studies help to understand the self-assembly properties of semiflexible and topologically-complex systems and provide means to control micelle properties through macromolecular design. Additionally, the macromolecular design changes also provide an opportunity to control and enhance desired properties in polymer nanocomposites. Thus, the work conducted as a part of this dissertation is very valuable to understand design-structure-property relationships by providing insights into the physics principles operating at the nanometer length scale.

Table of Contents

Chapter 1: Introduction 1

1.1 Universality of the process of self-assembly 2

1.2 Objectives and motivation 4

1.3 Self-assembly of block copolymers (bcps) 7

1.4 Role of tunable flexibility and topological design on block copolymer self-assembly 12

1.4.1 Self-assembly of rod-coil diblock copolymers in selective solvents 12

1.4.2 Impact of chain topology on self-assembly of miktoarm star block copolymers 15

1.4.3 Impact of chain characteristics on energetics of polymer-inorganic hybrid systems 17

Chapter 2: Research Tasks and Characterizations 21

2.1 Details of semiflexible and miktoarm star block copolymer systems 22

2.2 Characterization of self-assembled structures 25

2.2.1 Light scattering 25

2.2.2 Data analysis 28

2.2.3 Transmission electron microscopy 37

Chapter 3: Impact of Chain Microstructure on Solution and Thin Film Self-assembly of PCHD-based Semiflexible/flexible Diblock Copolymers 40

3.1 Abstract 41

3.2 Introduction 42

3.3 Experimental section 45

3.3.1 Materials 45

3.3.2 Polymer solution preparation 47

3.3.3 Film preparation 48

3.3.4 Characterizations 48

3.4 Results and discussion 50

3.4.1 Micellization as a function of chain microstructure 63

3.5 Conclusions 67

Chapter 4: Solution Self-assembly of Polystyrene-Polyisoprene Miktoarm Star Copolymers: Effect of Architecture and Conformational Asymmetry 68

4.1 Abstract 69

4.2 Introduction 70

4.3 Experimental section 73

4.3.1 Synthesis of PS_n-PI_n miktoarm star copolymers 73

4.3.2 Characterization of self-assembled structures in n-hexane 75

4.4 Results and discussion 77

4.4.1 Solution behavior of miktoarm stars 77

4.4.2 Morphology studies 86

4.4.3 Impact of architectural design and composition on solution self-assembly of miktoarm stars 88

4.5 Conclusions 91

Chapter 5: Utilizing Chain Entropy to Control Dispersion and Thermal Properties of Polymer Nanocomposites based on Poly(1,3-cyclohexadiene) Polymers 93

5.1 Abstract 94

5.2 Introduction 94

5.3 Experimental section 98

5.3.1 Synthesis of poly(1,3-cyclohexadiene) (PCHD)-$SiCl_3$ end-capped polymer with different chain microstructures 98

5.3.2 Grafting of PCHD-$SiCl_3$ onto bare silica nanoparticles 100

5.3.3 Preparation of 5% w/w polymer nanocomposite (PNCs) 100

5.3.4 Characterization of the nanocomposite blends 101

5.4 Results and discussion 102

5.4.1. Effect of chain microstructure (flexibility) and molecular weight on glass transition temperatures of the polymer nanocomposite blends 102

5.4.2 Nanoscale organization of polymer grafted nanoparticles with chain flexibility and molecular weight 107

5.5 Conclusions 114

Chapter 6: Summary, Conclusions and Future Work 115

6.1 Summary and conclusions 116

6.2 Future work 119

List of References 122

Appendices 137

Appendix A – Chapter 4: Solution Self-assembly of Polystyrene-b-Polyisoprene Miktoarm Star Copolymers: Effect of Architecture and Conformational Asymmetry 138

A.1 Zimm plots of PS_n-PI_n miktoarm star copolymers in n-hexane 139

A.2 Calculation of the radius of the core, R_{core} and surface area per macromolecule, S at the interface of spherical micelles formed from PS_n-PI_n star copolymers 144

Appendix B – Chapter 5: Utilizing Chain Entropy to Control Dispersion and Thermal Properties of Polymer Nanocomposites based on Poly(1,3-cyclohexadiene) Polymers 147

B.1 TEM images of PCHD-grafted silica nanoparticles before and after annealing in matrices of PCHD and PS 148

Vita 152

List of Tables

Table 3-1. Molecular characteristics and glass transition temperatures of PS-b-PCHD copolymers.....47

Table 3-2. Summary of results from DLS and SLS measurements on PS-b-PCHD copolymers…….55

Table 4-1. Molecular characteristics of the PS_n-PI_n miktoarm star block copolymers as determiend by size exclusion chromatography (SEC) 75

Table 4-2. Solution properties and morphology of the self-assembled aggregates of PS_n-PI_n miktoarm star copolymers.....82

Table 4-3. Properties of micelles/aggregates of the self-assembled miktoarm stars. Calculated equivalent diblock, Q_{eq}, radius of the PS core, R_{core}, and area per macromolecular chain, S, occupied by the PI corona of the spherical micelles. 84

Table 5-1. Molecular characteristics of the graft and matrix homopolymers of PCHD and PS obtained from SEC. 99

Table 5-2. Thermal properties of PCHD-grafted polymer nanocomposites before and after 24 h of thermal annealing. 103

Table A-1. Summary the changes in the size of the core (R_{core} with different volume fractions of star copolymers in n-hexane. 146

List of Figures

Figure 1-1. Diagram of the self-assembly process in Tobacco Mosaic Virus. The building blocks that constitute protein molecules are pre-programmed to self-assemble into a protective outer coat for the virus' DNA. Image is obtained from reference # 6. 3

Figure 1-2. Various phases adopted by self-assembled block copolymers in bulk due to microphase separation of the two incompatible blocks. The figure reflects phase behavior of diblock copolymers as a function of macromolecular composition, f_B. The figure is obtained from reference # 35. 9

Figure 1-1. Phase diagram of A-B type diblock copolymer in a melt state illustrates that changing volume fraction of one block can induce order-order phase transitions in strong segregation limit. The figure was obtained from reference # 36. 10

Figure 1-4. Formation of spherical micelles by self-assembly of an A-B diblock copolymer in a solvent selective for the B block 10

Figure 1-5. Types of micelle structures adopted by rod-coil block copolymers in selective solvents, reflecting the impact created on morphologies due to packing of rod blocks. Adopted from an article by Olsen and Segalman, reference # 19. 14

Figure 1-6. Milner's theoretical phase diagram for miktoarm star copolymers which reflects a shift in phase boundaries as compared to the phase boundaries observed for diblock copolymers in bulk. The figure adopted from reference # 32. 16

Figure 1-7. The effect of matrix and graft flexibility on wetting/dewetting of polymer-grafted NPs. Increasing stiffness of graft and matrix chains reduces entropy losses associated with gain in mixing entropy, leading to better dispersion of polymer-grafted NPs as compared to flexible systems. The figure is adopted from reference # 53. 19

Figure 2-1. The cyclohexenyl rings of PCHD are connected via two different types of linkages, namely 1,4 and 1,2. The ratio of 1,4/1,2 linkages (chain microstructural ratio) controls the stiffness of the chain. 23

Figure 2-2. Six star copolymers of PS-PI studied in solution to understand the role of topology on self-assembly. The stars in the top row have same molecular weight of PS and PI blocks while the ones in the bottom row have twice the molecular weight of PI block. 24

Figure 2-3. The ALV/CGS-3 compact goniometer is a self-contained system with ALV-proprietary optical fiber based detector and ALV-5000/EPP correlator. The instrument pictured here was utilized to perform light scattering measurements. 27

Figure 2-4. Fluctuations in scattered intensity (left) are shown as function of measurement time, t at a given scattering angle (represented by the scattering wave vector, q). The straight line (black) represents the average intensity over the measurement time. The sketch on the right represents the decay in scattered intensity as function of lag time, τ. The figure is obtained from reference #s 60, 61 & 62. 28

Figure 2-5. Screen capture image showing correlation function $g_2(\tau)$-1 and time, τ, data points measured at various angles. The highlighted data in the image implies how data from the Origin workspace is selected and fit using a non-linear curve fit. 32

Figure 2-6. Screen captured windows where the appropriate fitting function – a double exponential fit has been customized. The image at the top is the window with the function and variables specified while the image on the bottom shows various parameters used to initialize the function. 34

Figure 2-7. Values of the amplitude of the decay rates, A_i, mean decay rates, Γ_i, obtained from fitting a double exponential decay to correlation functions generated for a sample show two different populations of scatterers. 35

Figure 2-8. Mean decay rates, Γ_i (left) and apparent diffusion coefficients, $D_{z,app}$ (right) for the two decay modes. 35

Figure 3-1. Representation of semiflexible poly1,3-cyclohexadiene (PCHD) with two different types of linkages (1,4 and 1,2-linkages) connecting the cyclohexenyl rings. 46

Figure 3-2. Light intensity second order autocorrelation functions (a) and hydrodynamic radii, R_h, distributions (b) of PS-b-PCHDs having different chain microstructure. The color coding by microstructure – blue for 50/50, red for 70/30, and black for 90/10 – is preserved throughout all of the figures. 52

Figure 3-3. Apparent diffusion coefficient, D_{app}, of PS-b-PCHD copolymers having different chain microstructure as a function of the scattering wave vector, q^2. Data for the low molecular weight PS-b-PCHD copolymers are shown in (a) and data for the higher molecular weight copolymers are presented in (b). Thes sense of the colors is same as in Figure 3-2. 54

Figure 3-4. Distributions of hydrodynamic radii, R_h, of PS (black curve, PCHD-OH (~90/10, green curve and mixture of PS and PCHD-OH (purple curve at 5 mg mL^{-1} in THF). 57

Figure 3-5. AFM images of PS-b-PCHD copolymers drop-cast to form thin films on clean silicon substrates. For an image of a given microstructure, the top image corresponds to the lower molecular weight PCHD while the bottom corresponds to higher molecular weight PCHD. Images A and B are for 90/10 microstructure at c = 5.0 mg mL^{-1}, which show the presence of worm-like structures. 70/30 microstructure block copolymers at c = 5.0 mg mL^{-1} show bulk polymer due to its existence as single chains in solution at c = 5.0 mg mL^{-1} in images C and D. Images E and F show ill-defined aggregates for 50/50 microstructure at c = 0.2 mg mL^{-1}. 59

Figure 3-6. TEM images of PS-b-PCHD copolymers drop cast on carbon film grids. Images were obtained at the same solution concentration used for obtaining AFM images. For a given microstructure, the top image corresponds to the lower molecular weight PCHD while the bottom image corresponds to higher molecular weight PCHD. Images A and B show spherical micelles formed for the block copolymers having 90/10 microstructure. Copolymers having 70/30 microstructure show thin film formation (Images C and D) and 50/50 microstructure show presence of ill-defined aggregates, as seen in images E and F. 60

Figure 3-7. The appearance of a second mode, represented in the apparent hydrodynamic radius, R_h, as non-selective poor solvent MeOH is added to solutions containing *S_4C_{11}.70.30* (a) and *S_4C_{17}.70.30* (b), suggests that the block copolymers having 70/30 microstructure in the PCHD blocks can be forced to aggregate. 63

Figure 3-8. Model structures for PCHD oligomers suggest a decrease in persistence length (l_p) as 1,2-content increases from 10% (90/10) to 50% (50/50). 65

Figure 4-1. (A) Second order light intensity autocorrelation functions of PS_n-PI_n miktoarm stars in n-hexane at c = 6 mg mL^{-1}. (B) and (C) show the distribution of hydrodynamic sizes. (B) depicts change in the distributions as a function of architecture for stars of symmetric composition and (C) shows distributions of compositionally asymmetric stars. The color schemes representing the star copolymers are: diblocks (n = 1; black), 4-arm stars (n = 2; green) and 8-arm stars (n = 4; red). 78

Figure 4-2. Apparent diffusion coefficient, $D_{app}(q)$, of PS_n-PI_n miktoarm stars copolymers as a function of the square of the scattering wave vector, q^2. Data for the symmetric stars are shown in (A) and data for the asymmetric stars are presented in (B). The sense of the colors is the same as in Figure 4-1. 81

Figure 4-3. Surface morphologies of PS_n-PI_n miktoarm star copolymers spin cast from n- hexane at a concentration, c of 6 mg mL^{-1}. In the top row, from left to right, the number of chains about the central junction increases while the composition is fixed for S/I = 1. The second row reflects the same increase in number of arms but the star composition is asymmetric, S/I = 0.5. The

impact of composition on morphology of the stars at a fixed number of arms manifests by comparing the images in the top (S/I = 1) and bottom (S/I = 0.5) rows. 87

Figure 4-4. Cryogenic transmission electron microscopy (cryo-TEM) images of aggregates of PS_n-PI_n stars vitrified in n-hexane using liquid N_2 as the cryogen. The top row shows images for stars of symmetric composition (S/I=1) and the bottom row presents images for asymmetric stars (S/I =0.5). 89

Figure 5-1. The three representative PNC sample images reflect the local reorganization due to thermal annealing of the samples. 108

Figure 5-2. Images acquired before annealing reflect the increase in dispersion of PCHD-grafted Si NPs in polymer matrices of increasing rigidity. The graft PCHD chain has a microstructure of 90/10. 109

Figure 5-3. Reflect the impact of varying PCHD graft flexibility on dispersion/aggregation behavior of PCHD-grafted Si NPs in a polymer matrix of constant flexibility. 111

Figure 5-4. Impact of matrix stiffness on distribution of nanoparticles in matrices of two extreme chain stiffness' (PS and PCHD). 111

Figure A-1. Zimm plot for PS_1-PI_1 (15k-15k) in n-hexane, a selective solvent for the outer PI blocks. Measurements were made at c = 7.5 and 10.0 mg mL^{-1} and a dn/dc value of 0.181 mL g^{-1} was used in the analysis. In addition to R_g and $M_{w,app}$ values reported in the dissertation, the second virial coefficient, $A_2 = 1.3\times10^{-8}$ mol dm^3 g^{-2} was determined. 139

Figure A-2. Zimm plot for PS_1-PI_1 (15k-30k) in n-hexane, a selective solvent for the outer PI blocks. Measurements were made at c = 7.5 and 10.0 mg mL^{-1} and a dn/dc value of 0.185 mLg^{-1} was used in the analysis. In addition to R_g and $M_{w,app}$ values reported in the study, the second virial coefficient, $A_2 = 3.2\times10^{-8}$ mol dm^3 g^{-2}, was determined. 140

Figure A-3. Zimm plot for PS_2-PI_2 (30k-30k) in n-hexane, a selective solvent for the outer PI blocks. Measurements were made at c = 7.5, 10.0 and 15.0 mg mL^{-1} and a dn/dc value of 0.187 mL g^{-1} was used in the analysis. In addition to R_g and $M_{w,app}$ values reported in the study, the second virial coefficient, $A_2 = 1.7\times10^{-8}$ mol dm^3 g^{-2}, was determined. 141

Figure A-4. Zimm plot for PS_2-PI_2 (30k-60k) in n-hexane, a selective solvent for the outer PI blocks. Measurements were made at c = 7.5, 10.0 and 15.0 mg mL^{-1} and a dn/dc value of 0.189 mL g^{-1} was used in the analysis. In addition to R_g and $M_{w,app}$ values reported in the study, the second virial coefficient, $A_2 = 2.3\times10^{-8}$ mol dm^3 g^{-2}, was determined. 142

Figure A-5. Zimm plot for PS_4-PI_4 (60k-60k) in n-hexane, a selective solvent for the outer PI blocks. Measurements were made at c = 15.0 and 20.0 mg mL^{-1} and a dn/dc value of 0.195 mL g^{-1} was used in the analysis. In addition to R_g and $M_{w,app}$ values reported in the study, the second virial coefficient, $A_2 = 5.5\times10^{-9}$ mol dm^3 g^{-2}, was determined. 143

Figure A-6. Zimm plot for PS_4-PI_4 (60k-120k) in n-hexane, a selective solvent for the outer PI blocks. Measurements were made at c = 7.5 and 15.0 mg mL^{-1} and a dn/dc value of 0.196 mL g^{-1} was used in the analysis. In addition to R_g and $M_{w,app}$ values reported in the study, the second virial coefficient, $A_2 = 9.5\times10^{-8}$ mol dm^3 g^{-2}, was determined. 144

Figure B-1. Images depicting the distribution of low molecular weight PCHD-grafted Si nanoparticles (90/10 chain microstructure in matrices of varying molecular weights and flexibility. 148

Figure B-2. Images depicting the distribution of high molecular weight PCHD-grafted Si nanoparticles (90/10 chain microstructure in matrices of varying molecular weights and flexibility. 149

Figure B-3. Images depicting the state of distribution of low molecular weight PCHD-grafted Si nanoparticles (70/30 chain microstructure in matrices of varying molecular weights and flexibility. 150

Figure B-4. Images depicting the distribution of low molecular weight PCHD-grafted Si nanoparticles (70/30 chain microstructure in matrices of varying molecular weights and flexibility. 151

Chapter 1: Introduction

1.1 Universality of the process of self-assembly

Self-assembly is the spontaneous organization of simple building blocks to form complex hierarchical structures. These structures have 3D order throughout compared to the constituent building blocks[1,3] and the ordering can occur in both systems, where the original simple components are either covalently linked or separate. Both short- and long-ranged interactions between parts or whole of the building blocks help stabilize the self-assembled structure at various length scales. Thus, the presence of these 3D hierarchical aggregates is found to exist universally, with examples of self-assembled objects existing in both living and non-living systems.[1-4] For example, various biomolecules critical to life such as ribosomes, proteins that are formed by folding of polypeptides, protein-lipid bilayers of a cell membrane, and helical nucleic acids are formed in nature by the process of self-assembly.[3,5] An example of self-asembly process is depicted in Figure 1-1. In non-living systems, forces operative at nanoscale lead to formation of interesting copolymer morphologies of technological importance, and at much longer length scales, galaxies form in space at the scale of thousands of kilometers.[1-5]

Examining the detailed steps involved in formation of useful 3D structure has led to applying these principles in material design and advancing various technologies.[7,8] Self-assembly process active in soft materials, especially block copolymers, lead to formation of microphase separated domains or supramolecular structures.[4,8,9] These structures are intriguing and have been successfully applied to a host of technologies. The applications of self-assembled block copolymers range from patterning surfaces for electronic circuitry,[10-13] membranes[16] for filtration and fuel cells, drug delivery systems[18] and oil remediation.[10-18]

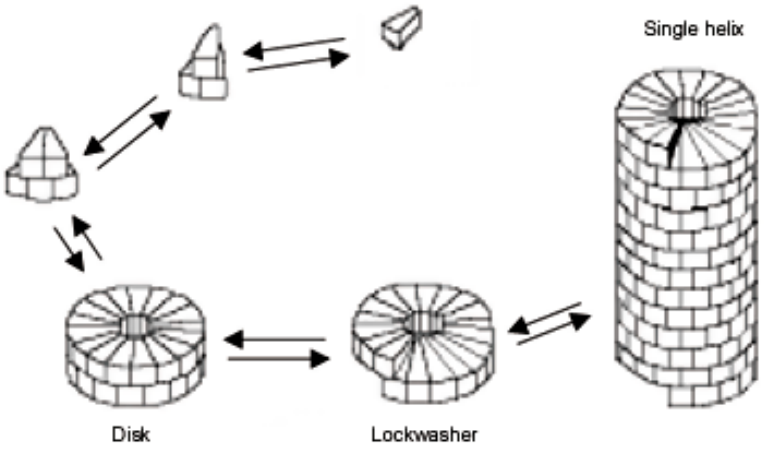


Figure 1-1. Diagram of the self-assembly process in Tobacco Mosaic Virus. The building blocks that constitute protein molecules are pre-programmed to self-assemble into a protective outer coat for the virus' DNA. Image is obtained from reference # 6.

In addition, the capacity of these materials to alter interfaces leads to these systems being used to reinforce or control dispersion in composites, alter surface properties or make polymeric coatings.[14,17] The main advantage of block copolymer systems is the ability to tune and control the micro-domain size through alteration of molecular characteristics. Moreover, changes in molecular characteristics provide the ability to assemble into hierarchical structures because polymer molecules, by virtue of their molecular weight and size, bring into play specific energetic interactions to create complex assemblies. These energetic interplays lead to phase behavior for block copolymers that is fundamentally very appealing and, therefore, studying the phase behavior as a function of macromolecular design is the main theme of this dissertation work.

1.2 Objectives and motivation

The goal of this dissertation is to enhance fundamental understanding of how macromolecular design variation, introduced through changes in conformational complexity – namely chain flexibility and topology – affects the self-assembly of block copolymers in solution and at surfaces. Further, I study the role played by tunable rigidity in influencing the dispersion of inorganic nanoparticles in a polymer matrix. This idea is applied to polymer-grafted nanocomposites (PNC) helps isolate the entropic contribution of polymer chains on dispersion by virtue of leaving the monomer type leaving unaltered.

The studies of phase behavior will be accomplished by investigating two model systems based on polystyrene-b-poly(1,3-cyclohexadiene) (PS-b-PCHD) and polystyrene-polyisoprene (PS-PI) miktoarm star copolymers. By studying two different systems, impact of conformational complexity on phase behavior will be successfully decoupled from rigidity and topology. It is important that the impact of these two chain characteristics be independently understood so strong links can be drawn between those distinguishing characteristics and phase behavior.

Chain rigidity for a polymer chain is described in terms of its persistence length, l_p. The rod-like character acquired by a polymer chain affects the arrangement of the chains in structures formed by self-assembly, and rigidity is a feature that distinguishes semiflexible block copolymer systems.[19] A majority of the work dedicated to evaluating the role of rigidity in block copolymer self-assembly has been focused on studying rod-coil block copolymers, including charged (polypeptides, DNA, etc) and neutral polymers. In these cases, stiffness of the chain is imparted due to functional groups with restricted rotation in the individual monomer units or due

to strong interactions (π-π interactions,[20-23,29] H-bonding[28]) between groups along the backbone. This chain stiffness, either intrinsic or acquired due to strong inter-chain interactions, causes the chain to have a specific orientation, which results in the aggregate structures formed adopting a more gradual curvature. Thus, packing constrains enforced by the intrinsic chain character drives the phase behavior of rod-coil systems to deviate from conventional block copolymer system phase behavior.[19]

A considerable amount of research effort has been dedicated towards understanding self-assembly of rigid polymers because a variety of unusual phases have been observed in theoretical and experimental studies.[19-31] These phases, however have not been directly linked to chain stiffness. The inability to directly link chain stiffness to phase behavior is challenging because studying the impact of chain flexibility generally involves changing the chemical type of the polymer or the chains become rigid because of strong associations between the chains. To overcome this challenge, entropy contributions to phase behavior needs to be isolated due to changes in chain conformation without manipulation of the chemical type. Poly(1,3-cyclohexadiene) (PCHD)-based copolymers provide an opportunity to tune rigidity without altering the monomer type. In this dissertation, the task of understanding the impact of chain flexibility is understood by examining solution properties and morphology of PCHD-based diblock copolymers in a selective solvent, THF. As described earlier PCHD-based diblock copolymers serve as the first model system. The ability to tune chain flexibility by controlling the addition of monomer at different positions of the growing anionic chain end provides unique opportunities to isolate the impact of conformational entropy that is brought about by the changes in chain microstructure.

The second important theme of this work is to understand the impact of chain topology on self-assembly of complex miktoarm star copolymers in selective solvent. Efforts dedicated in the scientific community toward studying various architectural combinations of A-B type have shown shifts in phase boundaries[32] and formation of aggregate structures different from traditional morphologies.[33,34] However, discrepancies in the molecular weights, composition range and limited type of architectures that were studied for a given system have made drawing direct conclusions on their phase behavior a challenging task. In part, these challenges remain because of limitations associated with synthesizing complex architectures and their limited solubility in different solvents. Here, out of the possible architectural types, I focus on A-B type star copolymers. Copolymers based on polystyrene-polyisoprene (PS-PI) have been used because the number of arms attached to the central junction point and the relative molecular weight of the arm can be varied in controlled fashion.

This dissertation work is heavily focused on characterizing the self-assembled structures in selective organic solvents adopted by the two model systems mentioned previously: The first system is based on PS-b-PCHD diblock copolymers. Here, PS will serve as the flexible block and PCHD's flexibility can be varied by changes in chain microstructure. Three different sets of diblocks with variation in chain microstructure have been synthesized and studied. For a given chain microstructure, the molecular weight of the PCHD chain is varied. For the second system, topological effects on self-assembly were explored through A-B, A_2-B_2, and A_4-B_4 star copolymers made of polystyrene and polyisoprene in n-hexane, a thermodynamically good solvent for the PI block. Morphological characterization of both systems will rely on tools such as light scattering (DLS and SLS), atomic force microscopy (AFM) and transmission electron

microscopy (TEM). Finally, studies of the semiflexible nature of PCHD on the dispersion and energetics of an organic-inorganic hybrid system will be pursued. Specifically, PCHD homopolymers with different chain microstructures or PS homopolymers will be grafted onto silica nanoparticles (Si NPs) and their dispersion in both PCHD and PS matrices will be studied. The impact of graft and matrix rigidity/flexibility on dispersion will be examined using TEM, and thermal properties will be evaluated using techniques such as differential scanning calorimetry (DSC) and thermal gravimetric analysis (TGA).

Thus, this thesis work involves investigation of phase behavior of block copolymeric systems where chain packing, influenced by the chain flexibility and topology, dictates the properties of the micelles and polymer nanocomposites. In total, this research work provides considerable insight into how conformational complexity impacts phase behavior.

1.3 Self-assembly of block copolymers (bcps)

The microphase segregated assemblies formed from block copolymer materials are unique in the sense that the covalent bond between the blocks prevents complete phase separation. The microphase-separated domains are rich in one type polymer block, and they have specific curvature and size that are controllable by varying molecular and experimental parameters such as composition, flexibility, relative block lengths and degree of incompatibility. Collectively the parameters influence how chains arrange themselves in phase-separated domains and thus, chain packing is a critical factor in influencing phase behavior.[19-34]

Chain packing and the degree of incompatibility between the two blocks dictate

morphology and properties of microphase separated block copolymers. The various morphologies resulting from microphase separation of A-B type diblock copolymers in bulk are presented in Figure 1-2. One of the early works highlighting the importance of pair-wise interactions and chain packing showed that the degree of incompatibility and volume fraction induces morphological transformation in bulk, as is shown by the phase diagram in Figure 1-3. This study conducted by Bates and Matsen[36] served as a keystone for exploring phase behavior of block copolymers.

While Figure 1-3 points to the importance of χ in a two phase system (binary blend or a diblock copolymer), the total interaction strength becomes complicated as a third component, usually a solvent, is added.[36] Selectivity of a solvent towards one of the block of an amphiphilic block copolymer makes the block interact strongly with the solvent, leading to formation of micelles in solution, as is shown in Figure 1-4. In addition to the Flory-Huggins interaction parameter, chain characteristics such as the degree of polymerization, relative composition, monomer type, processing pathway, pH and temperature are among the various factors through which micelle shape and size can be controlled. Typical micelle morphologies accessible through molecular parameters include spheres, wormlike, vesicles, bicontinuous rods, and short hollow tubes, for example.[18-34] One striking example of the ability of diblock copolymers to adopt a host of morphologies is seen in work by Lodge and coworkers, where PS-b-PI copolymers were self-assembled in both styrene and isoprene selective solvents[37-39]

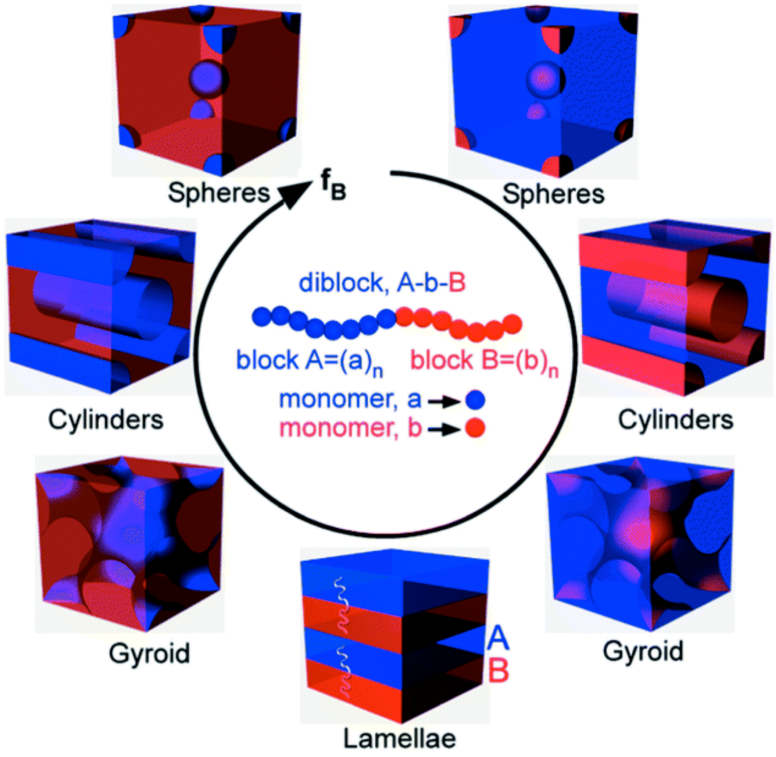


Figure 1-2. Various phases adopted by self-assembled block copolymers in bulk due to microphase separation of the two incompatible blocks. The figure reflects phase behavior of diblock copolymers as a function of macromolecular composition, f_B. The figure is obtained from reference # 35.

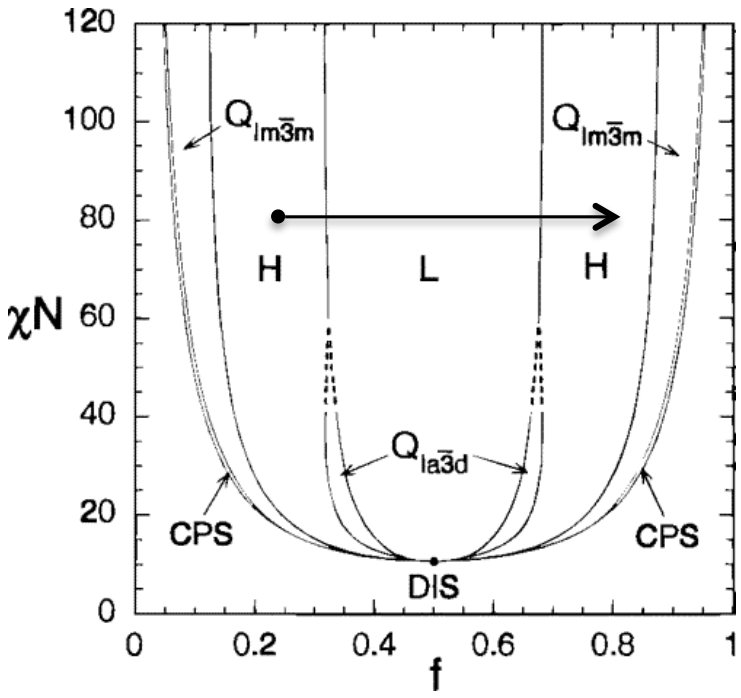


Figure 1-3. Phase diagram of A-B type diblock copolymer in a melt state illustrates that changing volume fraction of one block can induce order-order phase transitions in strong segregation limit. The figure was obtained from reference # 36.

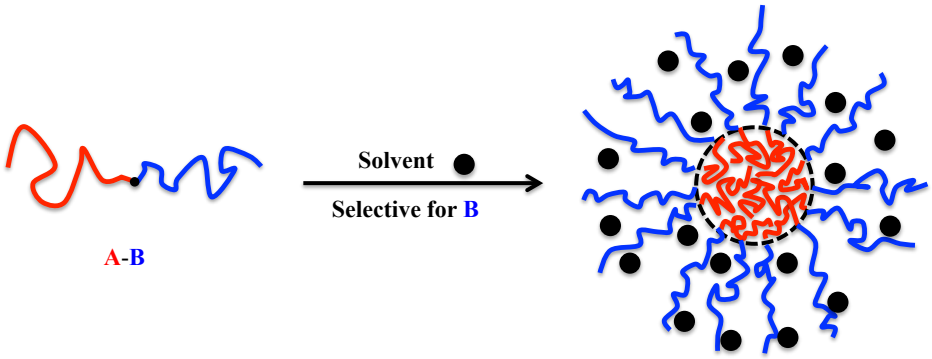


Figure 1-4. Formation of a spherical micelle by self-assembly of an A-B diblock copolymer in a solvent selective for the B block.

Strong selectivity of the solvent toward one block causes the block to interact strongly with the solvent, thus serving as a strong driving force for micellization. From a thermodynamic standpoint, formation of micelle is a direct result of reduction in free energy of the system. The overall free energy of micelle formation for A-B type diblock copolymer has three main contributing components as introduced by Zhulina and Birshstein:[40]

$$F_{micelle} = F_c + F_{cn} + F_{\text{int}} \tag{1.1}$$

Here, F_{micelle} is the free energy of the micelle, F_{c}, F_{cn}, F_{int} are the free energies of the core, corona and interface, respectively. Micelle formation is driven by the balance of these contributions to the overall free energy. The first term represents the free energy due to core formation. The selectivity of the solvent towards the corona block causes the solvophobic block (solvent hating) to aggregate, forming the micellar core. The second term describes the extension of solvophilic (solvent loving) corona block. Stretching limits the number of conformations a given corona chain will sample, making the micellar system pay an entropic penalty for stretching of the corona blocks. However, solvophilicity of the corona block (enthalpy) compensates the entropic penalty associated with corona stretching, lowering the overall free energy of the system. Formation of a micelle leads to creation of an interface, a region between core and corona blocks that increases the free energy of the system. As a result, a micellar system tends to minimize its curvature, with macromolecular design parameters, free volume restrictions and chain packing playing important roles. Different morphologies thus arise when $\Delta F_{\text{micelle}} < 0$, by virtue of the critical balance between the three energy contributions discussed above.[40]

Macromolecular design has a direct impact on chain packing, as it varies with persistence length of the chain, architecture and topological complexity. These parameters directly introduce geometrical constraints on packing of polymer chains, thus making them a crucial factor in determining phase behavior. As this thesis work is focused on studying the effect of chain rigidity and topological design on self-assembly, I discuss the importance of these influential parameters. The forthcoming section details self-assembly of rigid-coil block copolymers and miktoarm star copolymers.

1.4 Role of tunable flexibility and topological design on block copolymer self-assembly

1.4.1 Self-assembly of rod-coil diblock copolymers in selective solvents

Self-assembly of rod-coil diblocks is inherently different from coil-coil block copolymers due to effect of chain stiffness. Rigidity affects the conformational entropy and packing of the blocks. Polymers become stiff due to hindered rotation or restrictions in bending along the backbone. The presence of aromatic groups, π-π stacking and hydrogen bonding between chains causes the backbone to be oriented in a particular direction, resulting in a high persistence length (l_p) in comparison to a random coil.[2,19-31] As a result, formation of microphase-separated aggregates in rigid-flexible diblocks is a trade-off between interfacial energy, coil stretching and packing constraints, an additional contribution due to liquid crystalline defect energy, as pointed out by Olsen and Segalman.[19] Consequently, the liquid crystalline defects cause an increase in the free energy of the aggregate. To minimize the free energy, the rod-like blocks pack in a fashion that has gradual curvature in order to minimize the liquid crystalline defect energy. Compensating defect energy by arranging the rods in geometries of gentle curvature is typically

observed in cases of rod-selective solvents, with the rods packing on the outside of an aggregate. Similar to coil-coil block copolymer self-assembly, this can be understood in terms of free energy of micelle formation.

$$F_{micelle} = F_c + F_{cn} + F_{\text{int}} + F_{cd} \tag{1.2}$$

Here, an additional component, F_{cd}, describes the energy due to liquid crystalline defect energy introduced above. The structure of the micelles formed by rod-coil copolymers is strongly dependent on the block length and the solvent quality. Olsen and Segalman showed that in rod selective solvents, when the rods are short, the polymers tend to form bilayer vesicles, but form curved spherical or cylindrical micelles when the rod block is large relative to the coil. In case of coil selective solvents, the rods tend to segregate away from the solvent, leading to vesicles when the rod is larger compared to the coil and forming spherical or cylindrical micelles with shorter rod blocks. A representation of rod-coil self-assembly based on block length and solvent quality is shown in Figure 1-5.

In addition to the predictions made by Olsen and Segalman, theory[41] and experiments[19-31] have identified other morphological shapes exist for rod-coil block copolymers. This is mainly because a variety of rigid polymers studied acquire stiffness from the different type of interactions that may exist between segments of the polymer backbone. The specific nature of the interaction and rod-like character causes a shift in phase behavior of systems. A striking example of such a block copolymer system was highlighted in a study conducted by Jenekhe and Chen.[22] According to the authors, intermolecular hydrogen bonding interactions between

phenylquinoline groups of the diblock copolymer polystyrene-b-poly(phenylquinoline) (PS-b-PPQ) in CS_2 increased rod-like character of the polymer backbone. The hindered rotation of PPQ groups along the backbone was the main factor driving the formation of vesicular structures and also secondary 3D porous structure due to secondary hierarchical assembly of vesicles.[22]

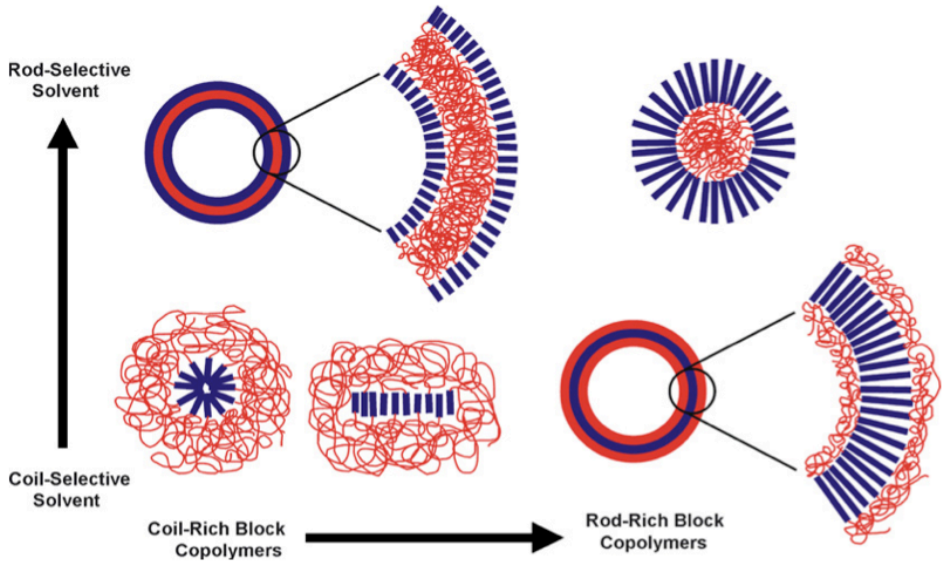


Figure 1-5. Types of micelle structures adopted by rod-coil block copolymers in selective solvents, reflecting the impact created on morphologies due to packing of rod blocks. Adopted from an article by Olsen and Segalman, reference # 19.

In CS_2, a coil solvent selective for PS block, the short PPQ rod blocks arrange on the inside of the vesicles in an orderly fashion, a deviation from the general prediction made by Olsen and Segalman.[19,22] Another example where intermolecular interactions between chain segments were the primary driving force for copolymer assembly was shown to occur by Surin et

al. In their work involving poly(9,9'-dioctylfluorine)-b-poly(ethylene oxide) copolymers (PF-b-PEO), long fibrils were reported to form due to strong (π-π) interactions between PF units, not due to solvent selectivity.[28] These predictions and experimental work reflect that an in-depth understanding of the fundamental phase behavior of rod-coil systems is lacking, especially the role played by intrinsic rod-like character in the absence of strong interactions. Thus, a polymer system where the flexibility of the chain (entropic contributions) can be examined without changing the chemical nature of the polymer (enthalpic contributions) will help in drawing links between phase behavior and rigidity of the polymer block.

1.4.2 Impact of chain topology on self-assembly of miktoarm star block copolymers

Considerable effort has been dedicated to studying self-assembly of block copolymers, highlighting the importance of topological design, especially the impact of architecture and composition, on the structure and properties of the aggregates. One of the early links between macromolecular design and nano-sized structures was established by Milner.[32] His studies of mitkoarm star copolymers showed that by increasing the number of arms at a single junction point while maintaining constant composition, the structures adopted by miktoarm star copolymers in bulk deviate from conventional microphase separated morphologies observed for A-B diblocks. As depicted in Figure 1-6, in the strong segregation limit, the phase boundaries shift towards a higher volume fraction for an A_2B star as compared to its linear analog of the same composition and stiffness. In Milner's study, the impact of changes in the number of branches, n_i and stiffness, l_i, is included in conformational asymmetry parameter, ε. A key aspect of Milner's work was demonstrating morphology manipulation through conformational asymmetry, ε, which captures the effect of architecture and stiffness. A key aspect of Milner's

work was demonstrating morphology manipulation through conformational asymmetry, If the number of arms attached to the core and/or stiffness of the blocks is changed (n_i or l_i, respectively), a morphological transition is observed for a given composition of the blocks. This seminal study highlighted the importance of geometric and free volume constraints enforced by tethering more arms at a central junction point, which are responsible for the rich phase behavior exhibited by miktoarm star copolymers.[32] Experimental verification of predicted morphologies for A_2B miktoarm star copolymers based on polystyrene (PS) and polyisoprene (PI) followed soon.[42-49] Similarly, complex phase behavior has been observed for miktoarm star copolymers in selective solvents. The details on these have been provided in introduction of Chapter 4.

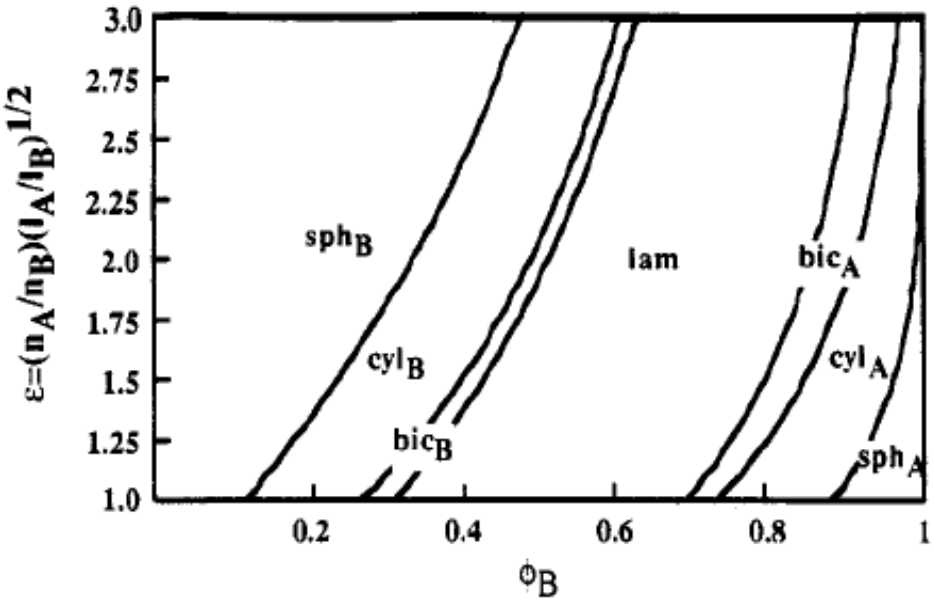


Figure 1-6. Milner's theoretical phase diagram for miktoarm star copolymers which reflects a shift in phase boundaries as compared to the phase boundaries observed for diblock copolymers in bulk. The figure adopted from reference # 32.

Drawing from works on self-assembly of rod-coil block copolymers and topologically-complex copolymers, I aim to study the impact of conformational complexity in block copolymers from a different approach. I independently studied the effect of chain flexibility on PCHD-based polymers and examine the influence of topological design on self-assembly of PS-PI miktoarm stars in solution. Further, the work described in this dissertation is extended to applying the unique ability of PCHD stiffness to control dispersion and properties of polymer nanocomposites. Here, the entropic effects are expected to dominate as the chain microstructure of PCHD will impact the dispersion of nanoparticles in polymer matrices and their properties. This concept will be studied by grafting flexible or semiflexible homopolymers onto the nanoparticles and blending them with homopolymers of different flexibility.

1.4.3 Impact of chain characteristics on energetics of polymer-inorganic hybrid systems

One key aspect of polymeric materials is their ability to modify surfaces, creating compatible interfaces for applications such as coatings, and thermal and mechanically reinforced composites, to name a few.[7,17,50-52] Grafting polymers onto inorganic nanoparticles (NPs) to modify surfaces provides ways to access properties currently limited by use of only soft materials. Combining hard and soft materials by dispersing surface modified inorganic nanoparticles in a polymer matrix provides an effective way to alter thermal or mechanical properties. One of the key challenges in inorganic-polymer hybrid systems is uniformly distributing a sufficient quantity of inorganic particles in the matrix in order to achieve the desired properties of a hybrid system. In particular, a large effort has been dedicated to grafting of flexible polymers onto nanoparticles, and examining how parameters such as graft polymer type, tethering density, and relative molecular weight affects dispersion of polymer-grafted NPs

in a polymer matrix[7,17,50-52]

While systems based on flexible polymer grafts have been studied extensively, systems based on semiflexible polymers have not been experimentally explored yet despite the dramatic role that restrictions in local chain conformations play on structure and dynamics.[7,17] One of the limitations in this pursuit is the lack of polymer systems whose rigidity can be tuned without altering the chemistry. Having a polymer in which the flexibility could be manipulated without changing monomer type would be a significant and compelling advantage. The motivation for this study is drawn from simulations conducted by Jayaraman and coworkers[53] showed that increasing the rigidity of the grafted polymer promoted better wetting of polymer-grafted nanoparticles by the matrix chains. In addition, the molecular weight and grafting density of the graft chains play critical roles in the wetting/dewetting behavior of nanoparticles. The authors attribute the wetting behavior of rigid grafts by the matrix chains to the reduced entropic penalty for stretching the rigid graft pays in comparison to flexible grafts of the same chemical identity.[53] Thus, chain rigidity can be used to alter dispersion, as shown in Figure 1-7.

This simulation study serves as motivation to investigate through experiments the role entropic contributions play in controlling dispersion and properties in polymer nanocomposites. A system based on PCHD-based materials is appropriate to conduct such a study, as the ability to tune chain microstructure without changing the monomer type helps minimize the effect of enthalpic interactions on dispersion. To proceed with the study, end-functionalized PCHD homopolymers of different chain microstructures, which as explained in Chapter 5 is tuned during synthesis, were grafted onto silica NPs. This allowed the role of flexibility to be examined

in semiflexible (PCHD) and flexible matrices (PS).

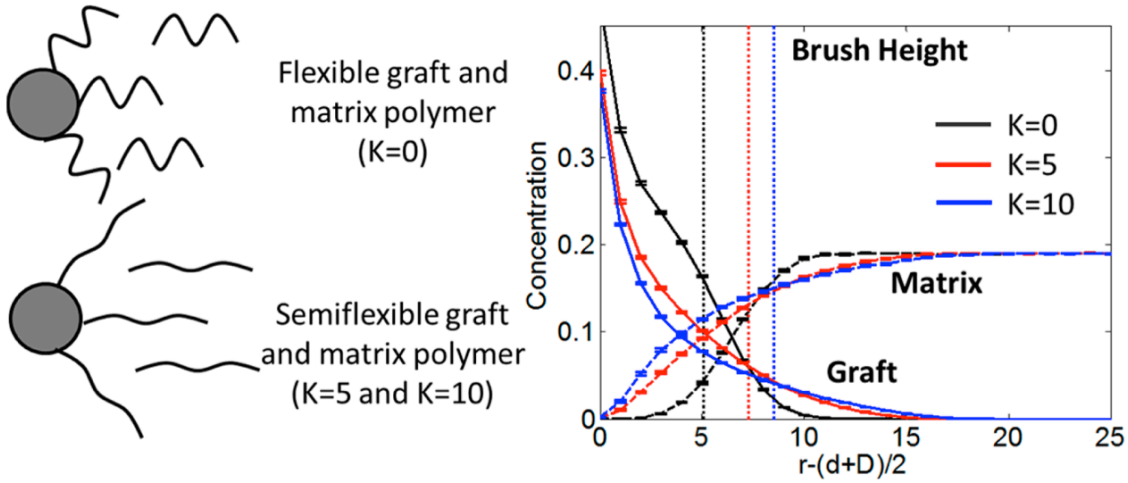


Figure 1-7. The effect of matrix and graft flexibility on wetting/dewetting of polymer-grafted NPs. Increasing stiffness of graft and matrix chains reduces entropy losses associated with gain in mixing entropy, leading to better dispersion of polymer-grafted NPs as compared to flexible systems. The figure is adopted from reference # 53.

The remainder of this dissertation is laid out as follows: the next chapter details the specific research tasks that were completed to achieve the goals highlighted above. Details concerning the synthetic methods, molecular characteristics, and the utility of the various characterization tools are also presented. Chapter 3 describes results of studies of solution self-assembly of PS-PCHD diblock copolymers. In Chapter 4, the role of topological design on solution self-assembly of PS-PI copolymers is examined. Chapter 5 describes a series of first-phase studies of polymer-grafted NPs using both flexible and semiflexible grafts and matrices.

This dissertation concludes with perspectives drawn from the entire body of work in Chapter 6. Additional supporting information is contained in two Appendices.

Chapter 2: Research Tasks and Characterizations

In this chapter I discuss the individual block copolymer molecular characteristics that were utilized to study the effect of chain flexibility and topology on self-assembly of block copolymers. Also, the principles and data analysis of various characterization techniques, such as light scattering, TEM and Cryo TEM, are discussed.

2.1 Details of semiflexible and miktoarm star block copolymer systems

As introduced in Chapter 1, the impact of chain flexibility and topological design on solution self-assembly is the main investigative theme of this work. The first theme is introduced through a system based on diblock copolymers composed of polystyrene-b-poly(1,3-cyclohexadiene) (PS-b-PCHD) in which flexibility of PCHD backbone is tuned without altering the monomer type. These copolymers will be used to understand how packing of semiflexible polymers impacts their self-assembly. In order to understand the effect of topological design, a system composed of polystyrene-b-polyisoprene (PS-b-PI) will be used. These copolymers have variation in the number of arms of each type and composition (using PI blocks of two different sizes), which will allow links between geometric constraints and solution phase behavior to be developed. Here, I discuss some synthetic details pertaining to both systems and then discuss the various techniques utilized to study phase behavior of these polymeric materials.

PCHD serves as the semiflexible block whose flexibility has been shown to be tunable without any changes in the chemical type.[54-57] Alteration in the flexibility occurs due to changes in chain configuration caused by linking of the repeat units at two different positions (1,4 and 1,2 positions of the repeat units) at the growing anionic chain end. The linking of 1,3-cyclohexadiene (1,3-CHD) monomer at either the 1,4-position or 1,2-position is shown in Figure 2-1. Precise

control over the chain microstructure is achieved by using different additives during the polymerization process. A significant number of efforts were directed at studying the type of reaction conditions that lead to changes in chain microstructure and, at the same time, correlating the noticeable differences in the physical properties with chain microstructures that were synthesized.[54-57] Therefore, in this dissertation work, three different chain microstructures (which reflect the ratio of 1,4 to 1,2 linkages): 90/10, 70/30 and 50/50, were prepared using a specific additive for the targeted chain microstructure. To achieve a chain microstructure ratio of 90/10 for PCHD, 1,4-diazabicyclo[2.2.2]octane (DABCO) was used during anionic polymerization and for 70/30 and 50/50 microstructures, the additive 1,2-dimethoxyethane (DME) was used in two different solvents.[54-57] These alter the rigidity of the polymeric chain, as reflected by the differences in their glass transition temperatures, T_g.[56] The materials used in the dissertation work were synthesized by collaborators from the Mays group. I would like to thank Xiajoun Wang for synthesizing the PS-b-PCHDs.

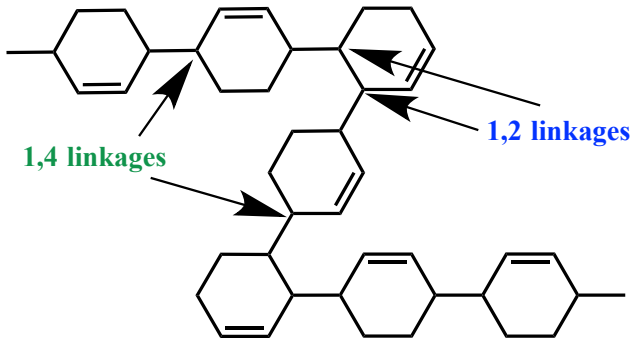


Figure 2-1. The cyclohexenyl rings of PCHD are connected via two different types of linkages, namely 1,4 and 1,2. The ratio of 1,4/1,2 linkages (chain microstructural ratio) controls the stiffness of the chain.

The investigation of the second polymer system involves six miktoarm star copolymers based on PS-PI. The star copolymers of PS-PI varying in the number of arms and molecular weight of the PI arms relative to PS were synthesized using high-vacuum anionic synthesis. These miktoarm stars were utilized for studying the phase behavior in solution. The polymers can be divided into two categories: one category of star polymers has the same molecular weights of the PS and PI blocks but have different architectures, such as diblock, 4-arm and 8-arm star copolymers. The second category of star copolymers consists of diblock, 4-arm and 8-arm star architectures, but the molecular weight of PI block is twice that of the PS block, as shown in Figure 2-2. These two systems are studied in thermodynamically selective organic solvents to help evaluate the role played by conformational complexity on solution structure and morphology of nanocomposites.

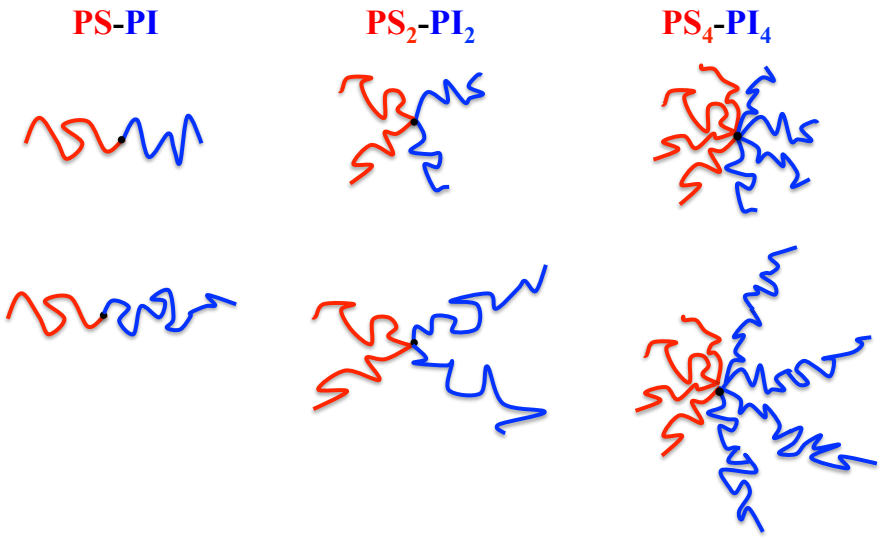


Figure 2-2. Six star copolymers of PS-PI studied to understand the role of topology on solution self-assembly. The stars in the top row have same molecular weight of PS and PI blocks, while the ones in the bottom row have twice the molecular weight of PI block.

2.2 Characterization of self-assembled structures

In this section, I discuss the various techniques employed to study the phase behavior of block copolymers. A major portion of the work examined phase behavior in solution (selective organic solvents), with one of the model systems (PS-b-PCHD) extended to studies of nanocomposites. The main methods utilized to study the systems in solution include light scattering and microscopy techniques.

2.2.1 Light scattering

Light scattering is a non-destructive way to analyze colloidal assemblies in solution. Describing their diffusion in solution can be utilized to estimate the size population. Also, due to the colloidal nature of solution, information such as apparent molecular weight, solvent quality and radius of gyration can be estimated.[58-60] In light scattering, two primary techniques to obtain size and shape characteristics of scatterers (aggregates) in solution exits, and these are referred to as dynamic light scattering (DLS) and static light scattering (SLS).

Both DLS and SLS involve the same fundamental phenomenon. An oscillating electromagnetic field (light wave) incident upon a solution is scattered without any change in the energy between the incident and scattered light. The temporal dependence of the scattered wave is related to the diffusion rate of the scatterers in solution. The rate at which particles diffuse is contained within and quantified by determining the mean decay rate, Γ, from which the apparent diffusion coefficient, $D_{app}(q)$, is determined. The Stokes-Einstein relation is used to relate the diffusion coefficient to the hydrodynamic radius, R_h, of the scattering species in their native

environment. Because the temporal fluctuation of scattered light is monitored to determine Γ, this technique is termed as DLS. The other variation of the scattering technique named SLS, is based on the same phenomenon but involves measuring the total scattered intensity over a fixed time. SLS is used to determine aggregate characteristics listed in the above paragraph. Both of these techniques are extremely useful for studying block copolymer assemblies in solution, in a non-destructive way. These methods are the basis for understanding aggregation behavior as a function of controllable, external parameters such as temperature, pH and salt concentration, and have been widely applied to polymeric and biological systems in solution.[58-62]

This chapter will focus on theoretical considerations and data fitting process for both DLS and SLS using an ALV system to perform light scattering measurements. Measurements were carried out on a four-detector, goniometer-based ALV system equipped with a linearly polarized 22 mW HeNe laser operating at a wavelength, λ, of 632.8 nm. The instrument is mounted on an optical table to reduce the effects of vibrations. The incident beam gets reflected by two mirrors and any increased scattered intensity that may occur is reduced by a liquid crystal attenuator before being analyzed by a built-in quadrant-photodiode equipped with a beam splitter plate. The laser light is then focused into the sample cell that is positioned in the center of the scattering cell, which is filled with toluene. The scattering cell is mounted on a motor-driven precision goniometer (±0.01°), which is equipped with four detectors interleaved by 34° from one another. This design allows multi-angle measurement of a sample at a given temperature. A picture of the ALV light scattering instrument is displayed in Figure 2-3.

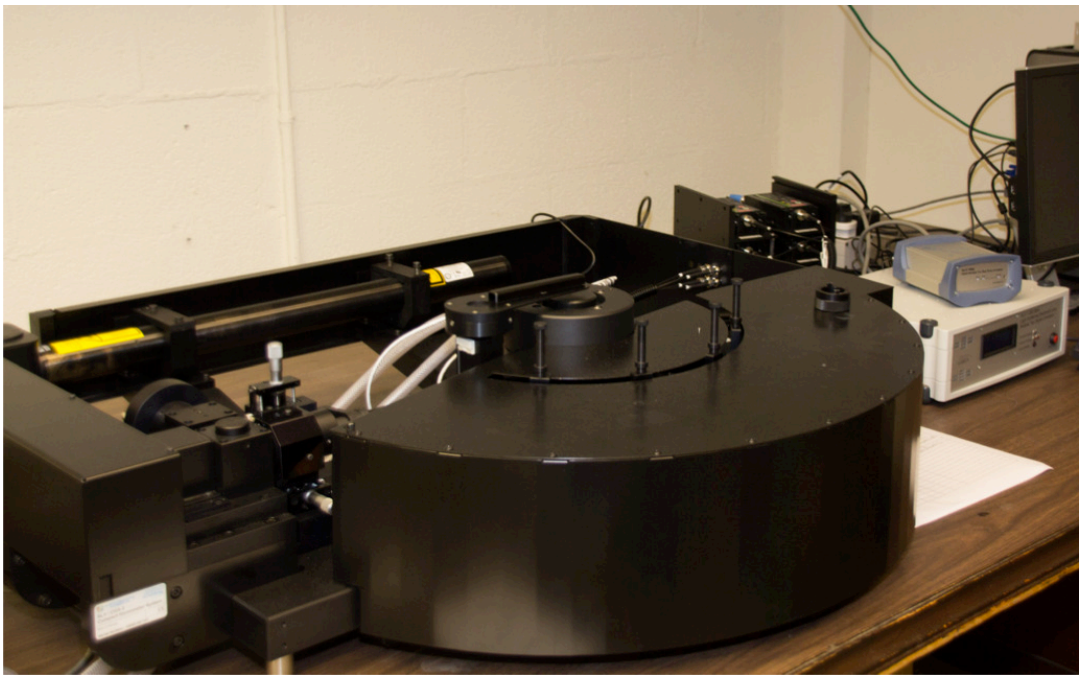


Figure 2-3. The ALV/CGS-3 compact goniometer is a self-contained system with ALV-proprietary optical fiber based detector and ALV-5000/EPP correlator. The instrument pictured here was utilized to perform light scattering measurements.

Experimental protocols for both DLS and SLS are different. Because light scattering measurements are conducted for two different block copolymer systems, I discuss the individual procedures in the chapters pertaining to each of those model systems. The following section discusses some general light scattering principles and some of the parameters involved during measurements and analysis of the obtained data.

2.2.2 Data analysis

Dynamic light scattering. The motion of scattering particles through the portion of the liquid being irradiated by the incident light gives rises to fluctuations in the scattered intensity, which is recorded. The fluctuations are temporal and result from Brownian motion of the particle, describing the motion of a particle in reference to other moving particles and solvent molecules. Displayed in Figure 2-4 are fluctuations in scattered intensity as a function of time at a given scattering angle.[60-62]

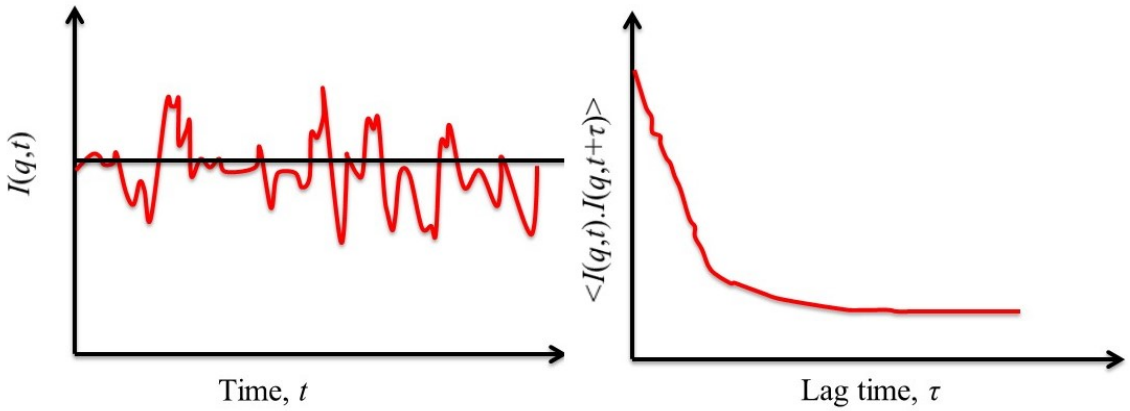


Figure 2-4. Fluctuations in scattered intensity (left) are shown as function of measurement time, t at a given scattering angle (represented by the scattering wave vector, q). The straight line (black) represents the average intensity over the measurement time. The sketch on the right represents the decay in scattered intensity as function of lag time, τ. The figure is obtained from reference #s 60, 61 & 62.

Displayed on the left of Figure 2-4 is the signal recorded by a photomultiplier as a function of time at a given scattering angle. The fluctuating signal is translated by a multichannel digital correlator into a mathematical construction – the light intensity autocorrelation function - which is displayed in the plot on the right of Figure 2-4. This translation is achieved by multiplying the time-dependent scattered intensity by scattered intensity after a short time interval, defined as the lag time or delay time, τ. The light intensity autocorrelation function, $<I(q,t)\cdot I(q,t+\tau)>$, whose dependence on delay time, τ, is calculated for various values of τ, ranging from (in our case 125 ns to several seconds. At very small τ, the intensity is strongly correlated, but at longer τ, because the Brownian motion is random, the correlation is lost. At a given scattering angle, the time-dependence of the light intensity autocorrelation function, $g_2(q,\tau)$, is related to the first-order electric field autocorrelation function, $g_1(q,\tau)$, by the Siegert relation:[60-62]

$$g_2(q,\tau) = 1 + g_1(q,\tau)^2 = \frac{\left\langle I(q,t)I(q,t+\tau)\right\rangle}{\left\langle I(q,\tau)^2\right\rangle} \tag{2.1}$$

Here $I(q,t)$ is the scattered light intensity at time t and $g_1(q,\tau)$ is the first-order electric field correlation function, which depends on the delay time τ and the scattering wave vector, q, which is determined from the scattering angle θ, λ, and the solvent refractive index, n: $q = (4\pi n/\lambda)\sin(\theta/2)$. The amplitude distribution of decay rates, $A(\Gamma)$, which provides insight into the population distribution of scatterers in solution, was extracted by analyzing the autocorrelation function obtained at each angle using the CONTIN algorithm. The method of regularization utilized by the algorithm satisfies the following expression:[63]

$$\left[g_2(\tau)-1\right]^{1/2} = g_1(\tau) = \int_0^\infty A(\Gamma)e^{-\Gamma t}\, d\Gamma \tag{2.2}$$

For the polymer solutions where CONTIN analysis showed one peak in the distribution of decay rates, the method of cumulants is used to determine the mean decay rate, or first cumulant, Γ_1, and the normalized variance, μ_2/Γ_1, at each scattering angle:[64]

$$\frac{1}{2}\ln\left[g_2(\tau)-1\right] = \Gamma_0 - \Gamma_1\tau + \frac{\mu_2}{2}\tau^2 \tag{2.3}$$

Γ_0 is a constant independent of τ. Solutions that exhibited two decay modes are analyzed using a double exponential distribution, as given by equation 2.4.

$$g_1(\tau) = A_1\exp(-\Gamma_1\tau) + A_2\exp(-\Gamma_2\tau) \tag{2.4}$$

In this expression, A_1 and A_2 are the relative amplitudes of each characteristic decay mode, Γ_1 and Γ_2. After obtaining the characteristic decay rate for the different modes, the apparent diffusion coefficient, D_{app}, is calculated using

$$D_{app}(q) = \frac{\Gamma_i}{q^2} \tag{2.5}$$

From $D_{app}(q)$, the value of the apparent z-average diffusion coefficient, $D_{z,app}$ is obtained by extrapolating $D_{app}(q)$ to $q = 0$, which removes contributions from polymer segmental motions and rotation fluctuations to $g_1(q,\tau)$. Once $D_{app}(q)$ values are obtained, the apparent hydrodynamic

radius, R_h, is calculated by using the Stokes-Einstein relation:[60-62]

$$R_h = \frac{kT}{6\pi\eta_0 D_{z,app}} \tag{2.6}$$

In this expression, k is the Boltzmann constant, T is the absolute temperature and η_0 is the solvent viscosity. To calculate the values of mean decay rates of different populations, fitting of the light intensity autocorrelation functions is carried out using equations 2.3 and 2.4. The steps for fitting are described below:

Step 1: After the measurements are complete, a regularization fit using 250 channels is performed on the correlations functions measured in DLS. The starting point on the function is chosen after the initial sampling time of 2.5 ns (time taken by correlator to begin interpreting the data) and the end point is the baseline of the correlation function at longer lag time. The data points for regularized fit of the correlation function and the amplitude distribution of the mean decay rates of the scatterers obtained are then exported as a CSV file. Because the goniometer system allows simultaneous measurement from four-detectors, every file has correlation function data from each of those detectors compiled into one data file. The data is then analyzed for all four individual angles using a script written by one of our collaborators, Prof. Masashi Osa. The details for using the script to understand and separate the correlation function and amplitude distribution data for individual angles, which generates a CSV file, has been described in the thesis work of Dr. Jesse Davis.[33] This section will spare those details and instead will focus on the steps that follow Dr. Davis' work. The CSV files are then imported to Origin 6.0 to fit the correlation function to obtain amplitude distributions and mean decay rates of the scatterers.

Step 2: The data comprising values for $g_2(\tau)$-1 and time τ, are copied into a new workbook in Origin for all 16 angles, as shown in Figure 2-5. The data is then fit by equation 2.4 using the script in step 1 if the amplitude distribution shows two decay modes. Presented in Figure 2-5 is an example of measured correlation function data at a given angle. The image on the right shows the highlighted data at a particular angle about to be fit by a non-linear method.

Before a fit can be performed, it is customary that a fitting function be created and tested before it can be applied to the selected data. Below the steps needed to create a fitting function are shown by demonstrating the use of equation 2.4, because the data presented here has two decay modes (a double distribution).

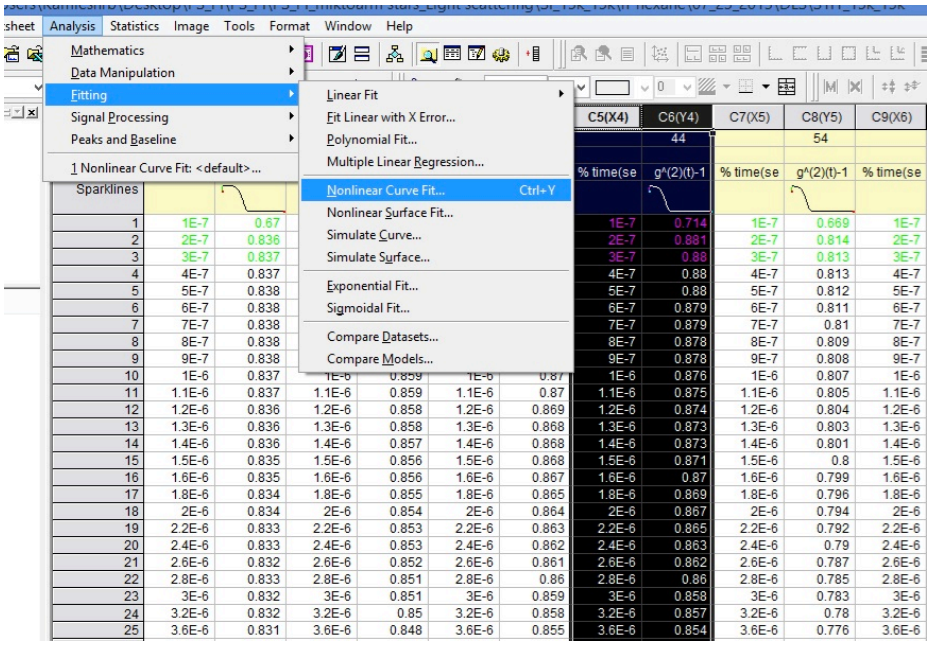


Figure 2-5. Screen capture image showing correlation function $g_2(\tau)$-1 and time, τ, data points measured at various angles. The highlighted data in the image implies how data from the Origin workspace is selected and fit using a non-linear curve fit.

Step 3: Figure 2-6 shows a window within Origin for creating custom data-fitting function named, in this case, a double exponential. The top image shows the double exponential function created in Origin based on variables in equation 2.4. The bottom image displays various initial values used to obtain the appropriate fit.

Step 4: After choosing and typing equation 2.4, initial values are selected by making an educated guess, and fitting process is allowed to begin. The Origin software performs a number of iterations and a value for the Chi-square is obtained. If the displayed fit and Chi-square values are found unacceptable, then the initial values of the variables are changed and the process is repeated. This process allows the fitting function to be applied to multiple data sets.

Step 5: After fitting sets of data from all sixteen angles, values of amplitude distribution and mean decay rates (displayed as G in Origin) are generated, as shown in the Figure 2-7.

Step 6: From the values obtained after fitting the data with a double exponential function, a graph of the mean decay rates versus the square of the scattering wave vector, q^2 is generated. By dividing the angle-dependent mean decay rates by q^2 the values for apparent diffusion coefficient, $D_{app}(q)$ are obtained using equation 2.5. The calculated values then generate a plot of $D_{app}(q)$ versus q^2 and linear fitting of the values is used to obtain the true z-average diffusion coefficient $D_{z,app}$ extrapolating by extrapolating to $q = 0$. The image generated for both fast and slow modes are shown in Figure 2-8.

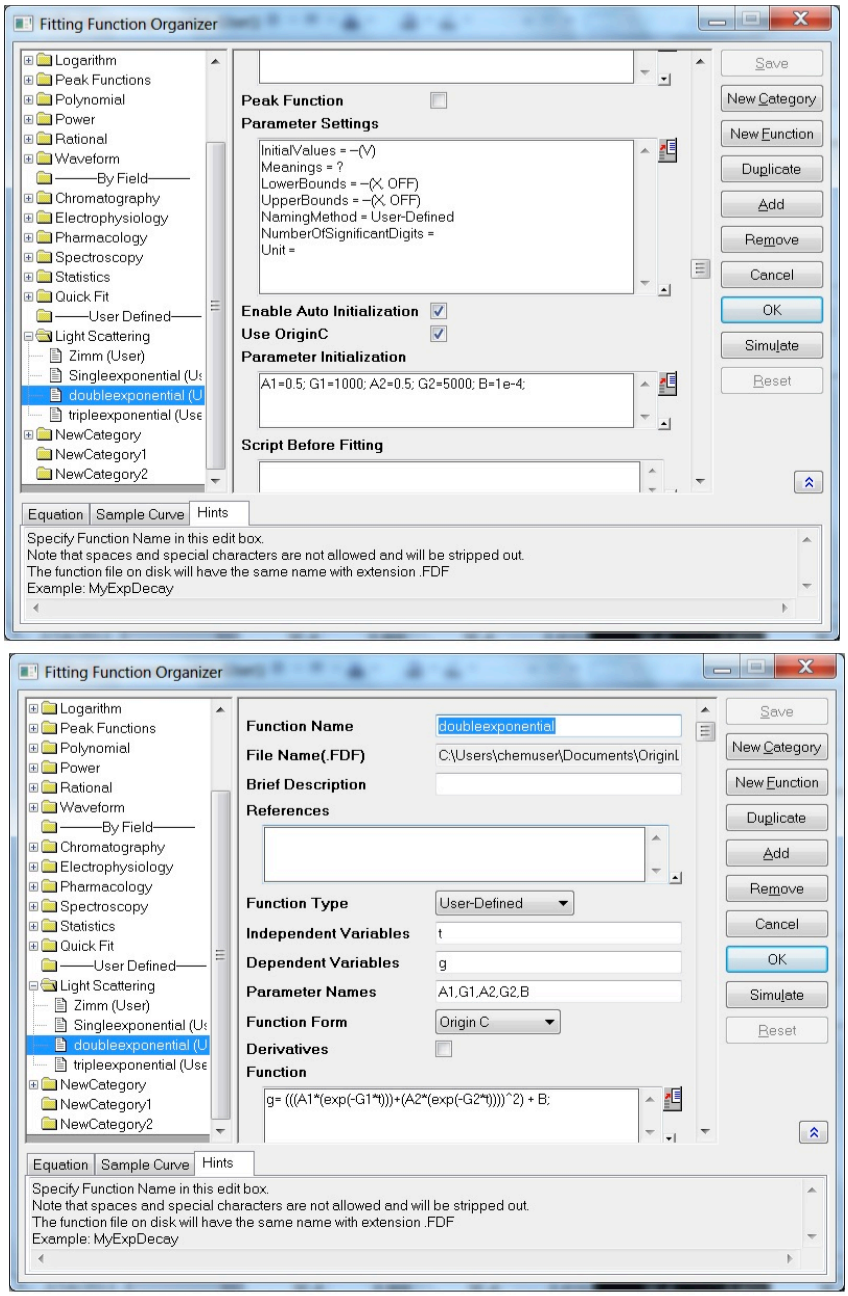


Figure 2-6. Screen captured windows where the appropriate fitting function – a double exponential fit - has been customized. The top image is the window with the function and variables specified while bottom image on the bottom shows various parameters used to initialize the function.

Nonlinear Curve Fit (Doubleexponential (User)) (4/24/2013 19:56:02)

Notes
Input Data
Parameters
Statistics
Summary

	A1		G1		A2		G2		B		Statistics	
	Value	Standard Error	Value	Standard Error	Value	Standard Error	Value	Standard Error	Value	Standard Error	Reduced Chi-Sqr	Adj. R-Square
20	0.67589	0.00712	96.14131	3.79532	0.24611	0.00703	3109.31071	163.72773	0.01883	0.00154	2.74329E-4	0.99787
28	0.6668	0.0034	238.45731	4.22694	0.24066	0.00335	6481.56927	158.28416	0.00177	6.10059E-4	4.67067E-5	0.99959
36	0.65578	0.00277	401.53232	5.80214	0.24826	0.00272	10587.6845	202.88374	5.84253E-4	4.65096E-4	2.84424E-5	0.99973
44	0.642	0.00217	595.54497	6.8172	0.25953	0.00212	15456.13979	221.10174	3.42946E-4	3.45397E-4	1.6227E-5	0.99983
54	0.63262	0.0039	885.98778	18.27987	0.27558	0.0038	22400.86448	539.90581	3.23304E-4	5.89257E-4	4.88111E-5	0.99948
62	0.61795	0.00375	1147.47491	23.18296	0.28824	0.00365	28704.37097	635.00619	5.23788E-4	5.42968E-4	4.23202E-5	0.99952
70	0.60143	0.00363	1458.81451	29.06649	0.30243	0.00352	35825.05654	727.04803	1.67924E-4	4.99268E-4	3.6468E-5	0.99956
78	0.58434	0.0035	1772.46555	34.88001	0.3169	0.00339	43008.93268	800.10427	2.05181E-4	4.60205E-4	3.14583E-5	0.99959
88	0.56804	0.002	2201.51123	25.29769	0.33248	0.00192	52912.36303	533.85002	2.01805E-4	2.51049E-4	9.51866E-6	0.99987
96	0.55206	0.00184	2557.69237	27.67465	0.34632	0.00177	60693.1534	537.93078	1.8083E-4	2.21089E-4	7.46636E-6	0.99989
104	0.53788	0.00176	2925.85241	31.04316	0.35796	0.00169	68690.19384	562.97036	1.49137E-4	2.04035E-4	6.42308E-6	0.9999
112	0.04458	0.10032	1297.08144	7459.84876	0.89298	0.09992	10744.72199	798.63467	2.28454E-4	7.00176E-4	7.07632E-5	0.99929
122	0.49245	0.01098	3510.65183	250.02891	0.37662	0.01052	79412.93676	3772.07875	-0.00104	0.00113	1.984E-4	0.99627
130	0.47997	0.00677	3859.54937	172.28683	0.38479	0.00648	85373.92375	2422.74843	6.5028E-5	6.6284E-4	6.91662E-5	0.99862
138	0.46846	0.00715	4107.08717	197.81012	0.39309	0.00684	90247.70732	2633.14449	5.40182E-5	6.78526E-4	7.28063E-5	0.99849
146	0.45866	0.00752	4280.49259	221.94868	0.39839	0.00719	94112.88771	2849.16224	7.96373E-5	6.99893E-4	7.76988E-5	0.99831

ANOVA

Figure 2-7. Values of the amplitude of the decay rates, A_i, mean decay rates, Γ_i, obtained from fitting a double exponential decay to correlation functions generated for a sample that displays two different populations of scatterers.

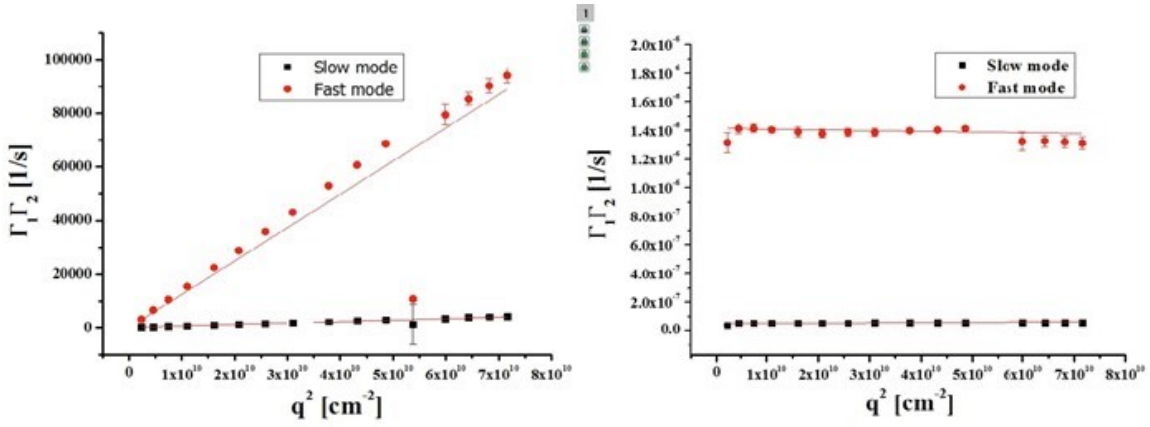


Figure 2-8. Mean decay rates, Γ_i (left) and apparent diffusion coefficients, $D_{app}(q)$ (right) for the two decay modes.

Thus, by following these steps, diffusion coefficients size distributions, and the hydrodynamic radii, R_h of each population of scatterers are calculated.

Static light scattering. Static light scattering measurements are made using the same four-detector ALV goniometer system. The measurements are made at 16 angles and several concentrations. Before any measurement is carried out, a solvent file is measured under the same conditions of temperature and angular range used for sample solution measurements. This solvent file "cancels out" any contributions scattering from thermal fluctuations of solvent, while a "standard file" corrects for scattering from the liquid bath containing toluene. Measurement of the solution to create a "solution file" is carried out first. Before the instrument begins recording any scattered intensity, dark counts are recorded to eliminate any contributions from the stray or surrounding light. For a SLS measurement the total average intensity is recorded by repeating the measurements three times. Each run lasts for 10s, recording the scattered intensity at every angle for a solution of given concentration. In order to obtain good Zimm plots, it is important to impose a constraint on the variation in the average intensity from the three runs. If the variation is greater than 5%, the measurement is discarded and the cycle of three runs is once again repeated. Under given experimental situations, if the measurement variation does not meet the 5% criterion, then a fresh solution for measurement is prepared. After satisfying the variance criterion, the average value of scattered light intensity is used to construct Zimm plots using the ALV software. I will not highlight these steps because I used the ALV software to construct the Zimm plots and also because the process used to construct Zimm plots is available in any polymer physics textbook.

2.2.3 Transmission electron microscopy

Transmission electron microscopy involves using a beam of electrons to irradiate a soft material such that the electrons are transmitted through the sample. An image is formed because some of the electrons in the sample are scattered by thin sections of the sample and the rest reach the photoluminescent detector. Assuming the film is of uniform thickness, contrast in TEM therefore arises due to differences in electron density and mass density (packing of polymer chains). TEM can be applied to study polymer morphologies in blends, composites and solution.[65]

Depending on the state of the sample being imaged, there are various challenges in sample preparation and imaging of the material. The methods for imaging of blends and nanocomposites have been well-described in the literature. In polymer blends, selective staining of a particular component, or a block in case of block copolymers, is often used to create contrast, allowing the morphology to be imaged. Nanocomposites based on electron-dense inorganic nanoparticles (Si, Fe, Ti) have contrast between the carbon-based matrix and inorganic filler. Challenges in sample preparation and imaging are common when attempting to determine the morphological characteristics of micellar systems in solution using cryo-TEM.[65] Due to high vapor pressure of organic solvents, under high-vacuum conditions of the column and imaging with the electron beam focused on small region of sample, the solvent evaporates, destroying the state of the micelle structure. An alternate approach involves physical fixation of the assemblies in solution. This is achieved by rapidly plunging the liquid into a suitable cryogen (based on compatibility of cryogen with the solvent) to vitrify the solvent and the micelle. The structures

are then directly measured while taking care to avoid exposing a given area to the electron beam for a long period of time.[65]

As stated earlier, cryo-TEM requires utmost care while preparing sample, as the vitrification involve multiple steps to obtain a uniform vitrified film of appropriate thickness that allows imaging with maximum contrast. The polymer structures that are imaged using cryogenic conditions can be classified into two types: water-based and organic-based samples. Water-based samples, i.e micelles formed from self-assembly of amphiphillic block copolymers, are frozen using liquid ethane as cryogen. The process of vitrifying samples using liquid ethane is more efficient due to higher freezing rate of liquid ethane compared to liquid nitrogen. Therefore, the popular choice for imaging structure in various solvents that are not hydrocarbon in nature is liquid ethane. For solvents with issues of solubility with a cryogen, vitrification of the sample is carried out using liquid nitrogen. Despite the lower freezing rates, good images with sharp contrast can be obtained by optimizing various sample preparation steps.[65]

In essence, TEM work demands a thin film to obtain images with contrast, at even high resolution. For the block copolymer systems investigated in this dissertation work, both regular and Cryo work was performed for morphological characterization of micelles as well as for imaging silica nanoparticles in polymer nanocomposites. For imaging PS-b-PCHD based structures, thin films were prepared from THF solvent. As THF in particular has a very high vapor pressure, performing cryogenic preparations to obtain a thin and uniform film on the grid is very challenging. From the literature it is known that THF by itself cannot be easily vitrfied[65] unless mixed with a supporting polar solvent such as water. Because, this dissertation work

focused hydrocarbon-based block copolymers, water was not used in any of the solution studies. To circumvent the problem of inappropriate vitrification associated with THF, samples were prepared on carbon film grids by drop-casting the sample and allowing it to air dry. For the second system involving PS-PI star copolymers, Cryo-TEM was done using liquid nitrogen. My process made sure that any inconsistences that could arise due to solubility of n-hexane in liquid ethane as a cryogen are completely avoided which helps to ensure uniformity of the vitrified samples. The lacey carbon grid (used for Cryo work) and carbon film grids were imaged using Libra 200X TEM microscope in the electron microscopy facility at UT. Details of sample preparation are discussed in Chapter 4.

In this chapter, I have provided detailed information relevant to the characterization techniques used in my thesis work. It is also necessary to point out that atomic force microscopy was also utilized in this thesis work, but only as a supplementary technique to image morphology on silicon wafers. Light scattering and TEM are central to studying the systems described in this thesis work.

Chapter 3: Impact of Chain Microstructure on Solution and Thin Film Self-assembly of PCHD-based Semiflexible/flexible Diblock Copolymers

This chapter describes work published in *Soft Matter* **2015**, *11*, 6509-6519. I characterized all of the diblock copolymers discussed in this work. Other coauthors include Dr. Xu Wang and Dr. Jesse Davis. Prof. Jimmy W. Mays, Dr. Xiaojun Wang and Dr. Weiyu Wang, who provided the polymer samples, and Prof. S. Michael Kilbey II, advised this work.

3.1 Abstract

Self-assembly of semiflexible/flexible block copolymers in a selective solvent is examined using a set of diblock copolymers where the chain microstructure of the semiflexible block is manipulated in order to vary chain stiffness. Conceptually, the reduced conformational space of the semiflexible block is anticipated to alter the way the chains pack, potentially changing the structure of self-assembled aggregates in comparison to flexible diblock copolymer analogs. Semiflexible/flexible diblock copolymers comprised of polystyrene-block-poly(1,3-cyclohexadiene) (PS-b-PCHD) having systematic changes in chain microstructure, as captured by the ratio of 1,4/1,2-linkages between cyclohexenyl repeat units, and molecular weight of the PCHD blocks were synthesized using anionic polymerization. These diblocks were dissolved in tetrahydrofuran (THF), which is a preferential solvent for PS, and the structures formed were examined using laser light scattering and complementary imaging techniques. Results show that PS-b-PCHD copolymers with a chain microstructure of 90% 1,4-/10% 1,2-linkages between cyclohexenyl repeat unit (referred to simply as 90/10) are able to micellize, forming spherical structures, while diblocks of 70/30 and 50/50 1,4-to-1,2 ratios remain as single chains and ill-defined aggregates, respectively, when dissolved in THF. With inferences drawn from simple structural models, we speculate that this self-assembly behavior arises due to the change in the

chain configuration with increasing content of 1,2-links in the backbone. This renders the chain with higher 1,2-content incapable of swelling in response to solvent and unable to pack into well-defined self-assembled structures.

3.2 Introduction

Self-assembly of amphiphilic block copolymers in selective solvents provides a way to generate molecular ensembles with a variety of interesting morphologies and characteristic dimensions that span from nanoscopic to mesoscopic length scale.[1,66,67] Self-assembled aggregates based on block copolymers have garnered significant interest for their utility in biomedical applications and as surface modifiers.[34] For example, diblock and triblock copolymer micelles have been used as drug delivery vehicles, with the core carrying the hydrophobic drug and the corona providing solubility and biocompatibility, as well as functional groups that aid in targeting.[68,69] Block copolymer micelles in which the core carries colloidal metals or heavy elements such as bromine or iodine can be used as diagnostic agents.[34] Moreover, the ability of micelles to physically adsorb or covalently react with a given surface makes them an attractive basis for preparing reactive or functional coatings. For example, Kataoka and co-workers prepared a non-fouling surface by covalently modifying an amine-containing polypropylene surface with a poly(ethylene glycol)-block-poly(lactic acid) micelle, whose PEG corona chains were end-functionalized with a reactive acetal group.[34,70]

To advance these applications and develop other potential uses, it becomes important to understand the links between chain properties and morphology of the aggregates/micelles. Parameters such as block lengths,[72-74], chain architecture,[32,42-49] flexibility,[76] solvent selectivity[75]

and temperature[77] are generally well-understood in relation to their impact on aggregation, micelle size and shape. It is known that chain stiffness impacts micellization due to the packing constraints, resulting in aggregates with more gradual interfacial curvature because rigid or stiff chains have fewer conformational states as compared to flexible chains.[19] While spherical, cylindrical, or vesicular structures are generally observed when flexible–flexible block copolymers (bcps) self-assemble in a selective solvent, unusual morphologies such as hollow spheres,[78] fibrillar structures,[28] bilayer filaments,[80] disc-shaped micelles,[30] to name a few, are observed in rod–coil systems. Olsen and Segalman point out that the rigidity of the rod-like block has a significant influence on the structure because, the aggregate must balance the penalty for ‘‘liquid crystalline’’-like defects when packing rod-like blocks and the curvature of the interface.[19] Consequently, the micelle morphologies formed from bcps containing stiff blocks tend to have a more gradually curved interface, depending on the relative block lengths and solvent selectivity.[19, 79-81]

In this regard, several studies have been carried out to demonstrate impact of coil to rod-like transitions on micelle morphology in solution. Particularly, the work by Ray et al.[78,79] on amphiphilic block copolymers with one of the blocks being polypeptide, show reversible transition from spherical to vesicle to disk-like micellar structures as the solution pH changes. Similarly, Nolte and co-workers found that the size of bilayer vesicles formed by self-assembly of PS-block-poly((isocyano-L-alanyl-amino-ethyl)-thiophene) (PS-b-PIAT) increased upon switching from a coil selective solvent, $CHCl_3$, to a tetrahydrofuran (THF)/water mixture, a rod selective solvent. In $CHCl_3$, the shorter solvophobic PIAT rods packed densely in the bilayer interior, leading to a smaller vesicle size. Vesicles formed in the THF/water mixture were of

larger size than those formed in $CHCl_3$ because the organization of the rigid PIAT blocks dictates the gradual curvature of the structure.[29] Because of the persistence length of helical structure, helix-forming poly(amino acid)s are often thought of as model semiflexible polymers. For example, Klok and co-workers demonstrated that a pH triggered helix–coil transition in the poly(L-glutamic acid) (PGA) blocks of polybutadiene-block-poly(L-glutamic acid) (PB-b-PGA) diblock copolymers caused a morphology change. Specifically, increasing the pH caused the ionization of the carboxyl group, which triggered the helix-to-coil transition of the PGA blocks.[80] The changes in the secondary interactions due to pH makes the polypeptide conformationally flexible, ultimately resulting in morphologies that differ in size.[80-82]

Although these studies highlight the impact of chain packing due to stiffness on micellar structures, none clearly link the origin of their phase behavior to intrinsic chain characteristics like stiffness. Moreover, many research studies employ polyelectrolytes with ionizable groups along their backbone, such as carboxylic acid and amino groups.[29,78-84] These electrolytic groups change their degree-of-dissociation in response to pH changes and added salt, bringing into play short-ranged Columbic interactions and H-bonding in addition to weak long-ranged van der Waal forces. With a greater number of intermolecular interactions governing the self-assembly process, it becomes difficult to clearly draw connections between chain character and its self-assembled structure. Further, it becomes imperative to point out that in conducting such experiments, changes in the chemical type of the polymer changes the effective interaction parameter.

In this dissertation the role rigidity plays on self-assembly is examined using a series of

polystyrene-block-poly(1,3-cyclohexadiene) (PS-b-PCHD) copolymers in THF, which is slightly selective for PS. In this pursuit, the ability to tune the rigidity of the PCHD block by using synthesis conditions to carefully control the ratio of 1,4/1,2 linkages between consecutive cyclohexenyl rings, without changing the monomer type, is a distinctive feature. The self-assembly of PS-b-PCHD copolymers having three different PCHD chain microstructures, namely 1,4/1,2 ratios of 90/10, 70/30 and 50/50, is studied in solution and thin films. Light scattering is used to determine the size of the aggregates in THF and microscopy techniques, namely atomic force microscopy (AFM) and transmission electron microscopy (TEM), are used to image the morphology of these systems.

3.3 Experimental section

3.3.1 Materials

Diblock copolymers comprising PS as the flexible block and PCHD as the semiflexible block were synthesized via anionic polymerization using custom-built, all-glass reactors with break seals by following procedures published elsewhere.[54-56] The PS block was synthesized first by initiating styrene in benzene, followed by crossover to initiate polymerization of 1,3-cyclohexadiene monomer (1,3-CHD) in presence of the appropriate additive. To achieve the targeted PCHD chain microstructure, particular combinations of initiator and polar additive were employed. Initiator/additive systems of sec-BuLi/1,4-diazobicyclo[2.2.2]-octane (DABCO) in benzene used to produce PCHDs having ~90% 1,4-content (1,4/1,2 ratio of 90/10). Similarly, sec-BuLi/1,2-dimethoxyethane (DME used to obtain ~70% 1,4-content (1,4/1,2 ratio of 70/30) and the use of n-BuLi/N,N,N',N'-tetramethylethylenediamine (TMEDA) in benzene yielded

PCHD with ~50% 1,4-content in the backbone.[54,55] The samples were characterized by a combination of size exclusion chromatography (SEC), ^{1}H NMR spectroscopy, and elemental analysis. The molecular characteristics of the block copolymers are summarized in Table 3-1 and a schematic showing PCHD chain microstructure is presented as Figure 3-1. Throughout this Chapter, I capture the block sizes and microstructure using a string of characters: for example, the name given to first polymer in Table 1, *S_4C_{11}.90.10*, identifies it as having a PS block of 4 kDa, a PCHD block size of 11 kDa with a chain microstructural ratio of 90/10 (1,4/1,2 ratio).

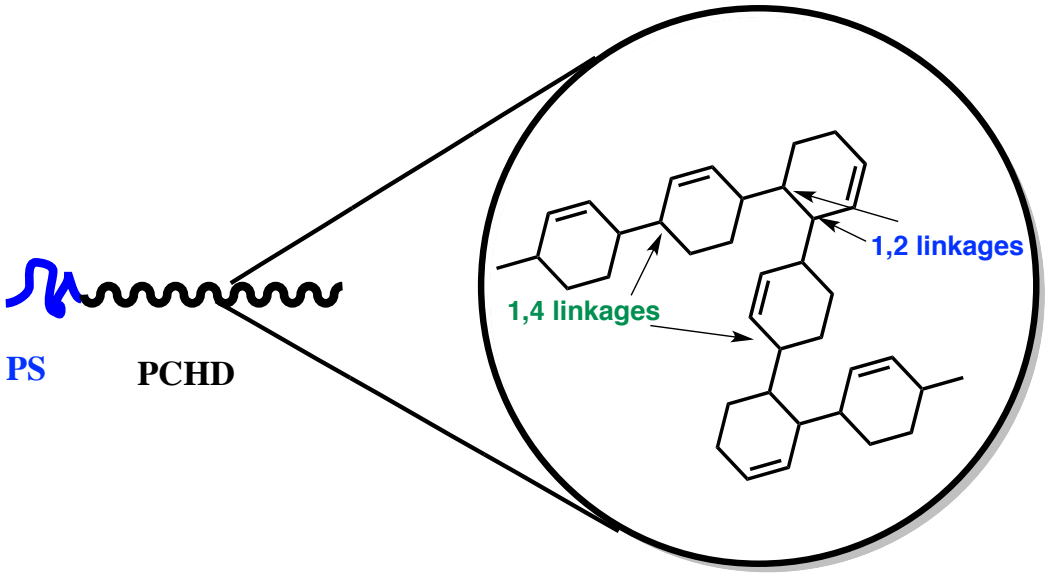


Figure 3-1. Representation of semiflexible poly(1,3-cyclohexadiene) (PCHD) with two different types of linkages (1,4 and 1,2-linkages) connecting the cyclohexenyl rings.

Table 3-1. Molecular characteristics and glass transition temperatures of PS-b-PCHD copolymers.

Sample ID	PS[a] M_n (g mol^{-1})	PDI	PS-b-PCHD[a] M_n (g mol^{-1})	PDI	1,4/1,2 ratio of PCHD	St/CHD (m/m, St %)[b]	Glass transition temperature T_g (°C)
S_4C_{11}.90.10	3800	1.08	14000	1.07	90/10	1/2.98	104
S_4C_{15}.90.10	3800	1.08	18000	1.17	90/10	1/5.26	116
S_4C_{11}.70.30	4100	1.07	15000	1.19	70/30	1/2.34	124
S_4C_{17}.70.30	4100	1.07	21000	1.24	70/30	1/5.45	133
S_5C_{11}.50.50	4500	1.07	15000	1.19	50/50	1/2.80	121
S_5C_{17}.50.50	4500	1.07	21000	1.17	50/50	1/4.75	135

[a]Obtained from SEC [b]Molar ratio of repeating units and weight percentage of styrene in PS-*b*-PCHD determined by ^{1}H-NMR.

3.3.2 Polymer solution preparation

Solutions were prepared gravimetrically by dissolving the diblock copolymer in THF, which is slightly selective for PS at room temperature. Because these solutions were eventually used for laser light scattering measurements, several precautions were taken to minimize

contamination by dust. The scintillation vials were cleaned prior to their use by washing with laboratory grade detergent, rinsing with copious amounts of water, and drying with a stream of dry nitrogen. Prior to making solutions THF was filtered through 0.22 μm PTFE filters to ensure that it was dust free. After the solutions were made, the vials were sealed with a Teflon lined cap and ultrasonicated until the polymer dissolved (visually). The solutions were allowed to equilibrate at room temperature for at least one week.

3.3.3 Film preparation

Diced silicon substrates (1 cm × 1.2 cm), obtained from Silicon Quest, were rinsed with deionized water and then were heated in a ‘‘piranha acid’’ solution (a 1:3 v/v mixture of 30% H_2O_2 and 98% H_2SO_4) for about 30–45 minutes (until no bubbles evolved). The piranha acid mixture was allowed to cool to room temperature before the wafers were removed. The silicon wafers were rinsed with copious amounts of distilled water and then dried using a stream of dry N_2 gas. The wafers were immersed for 24 hours in a previously prepared solution containing the PS-b-PCHD copolymer to allow the polymer chains (or their aggregates) to deposit (self-assemble on the surface. The wafers were removed from the solution and then dried in air.

3.3.4 Characterizations

Light scattering The details about the ALV instrument used to record scattering data is described in Chapter 2. For PS-b-PCHD diblock copolymer system, approximately 1.5 mL of the polymer solution was transferred in clean, dust-free 10 mm borosilicate glass cuvettes and capped before the measurement. The data for light scattering were recorded at a temperature of

25 ±0.1°C in THF with solvent viscosity, η of 0.456 cP for THF. The scattering angles used for measurements here range from 20° to 146° and a counting time of 3000s was used at each angle when acquiring data, in order to obtain statistically reliable data and enhance the signal-to-noise ratio. Information about the dynamic process is obtained by correlating the scattered intensity measured at each detector using ALV 7000 multiple tau digital correlator. Details on data analysis of dynamic light scattering measurements is described in Chapter 2.

Static light scattering (SLS) experiments also were conducted using the ALV instrument using toluene as the standard. The intensity at each angle was calculated as the average of $I(q)$ measured three times for 10s each. If the average count rate for any measurement vary by more than 5%, the measurements are repeated until the 5% criterion is satisfied. The measured scattered intensity of the solution at a single concentration and the corresponding amplitude of the decay modes obtained from dynamic light scattering for the same solution, were utilized to obtain an apparent radius of gyration, R_g of the large aggregates via a signal splitting process described later.[86]

Differential scanning calorimetry. The glass transition temperature of each of the block copolymers was measured using a TA Instruments Q1000 differential scanning calorimeter (DSC). A small amount of copolymer, approximately 3–12 mg, was weighed in a standard DSC pan using a microbalance and then sealed with a lid. Each sample was subjected to two heat–cool cycles, using the first cycle to erase the thermal history of the sample. On the first cycle, the temperature is lowered to -40 °C, ramped to 200 °C at a heating rate of 20 °C min^{-1}, and then lowered to 0 °C at a rate of 20 °C min^{-1} where it is held for 10 min before commencing the

second cycle. On the second cycle, the sample is heated to 200 °C at a rate of 10 °C min^{-1} and then lowered to 0.1 °C at a rate of 10 °C min^{-1}. The glass transition temperature (T_g) of the sample was calculated using TA Instruments supplied Universal Analysis software. T_g values were taken to be midpoint of the curve between the extrapolated lines that define the baselines of the rubbery and the glassy regions of the second heating curve.

Atomic force microscopy. AFM images were acquired using a Veeco Instruments Nanoscope IIIa multimode atomic force microscope in tapping mode using silicon cantilevers from Applied NanoStructures, Inc. (Mountain View, CA).

Transmission electron microscopy. TEM images were acquired using a Zeiss Libra 200 MC transmission electron microscope that is equipped with a Gatan UltraScan US1000XP CCD camera. To prepare a sample for TEM, 20 mL of the polymer solution was drop cast onto a carbon film grid. Excess fluid was blotted with a filter paper before the grid was allowed to dry in air. The sample grid was mounted on Gatan 915 double tilt holder with help of a copper anti-twist washer and a Beryllium hex ring and then introduced into the column and imaged.

3.4 Results and discussion

The molecular characteristics and glass transition temperature, T_g, of each of the PS-b-PCHDs examined are summarized in Table 3-1. The T_g values increase with increasing 1,2-content of PCHD in the backbone, and the values appear to plateau at about 50% 1,2-content, which suggests that the addition of 1,2-links in the backbone restricts chain movements. Similar thermal behavior has been reported for homopolymers of PCHD, where trends show that the

highest T_g values are observed for 50/50 microstructures and the lowest values for the 90/10 chain microstructure. Also, I note that the values reported in Table 3-1 are lower than those reported by Natori and Sato, and only one T_g is observed for PS-b-PCHDs studied here.[56,57] This suggests that the short oligomeric PS blocks are miscible with PCHD blocks and act as a plasticizer, which decreases the T_g. The fact that T_g increases as more 1,2-linkages are incorporated suggests that PCHDs having higher 1,2-content are more conformationally restricted, requiring more thermal energy (per unit mass) to cause a transition from a glassy state to a rubbery state. I posit that as the 1,2-content in the PCHD block increases, the chain crosses over itself more frequently, making it more conformationally restricted. Thus, when judged based on T_g only, 90/10 is perceived as the least rigid and 50/50 as the most rigid.

Dynamic light scattering measurements were used to examine the self-assembly behaviors of the semiflexible/flexible block copolymers in THF. Figure 3-2a shows examples of the light intensity autocorrelation functions obtained at a particular scattering angle for the PS-b-PCHD copolymers of different microstructure and molecular weight. Different concentrations, c, were used in acquiring these data because the solubility of PCHD diminishes as the 1,2-content increases: the copolymers having 90/10 and 70/30 microstructures were measured at c = 5.0 mg mL^{-1} but the samples having 50/50 microstructure were measured in the range of c = 0.170–0.185 mg mL^{-1} because of their limited solubility in THF. For *S_4C_{11}.90.10* copolymer (black curve, the shape of the correlation function implies the presence of more than one size scatterer in solution. However, the presence of more than one population is ascertained only after fitting the correlation functions to multiple exponential fits and obtaining their amplitude distribution rates. This provides insight into size distribution of scatterers, as presented in Figure 3-2.

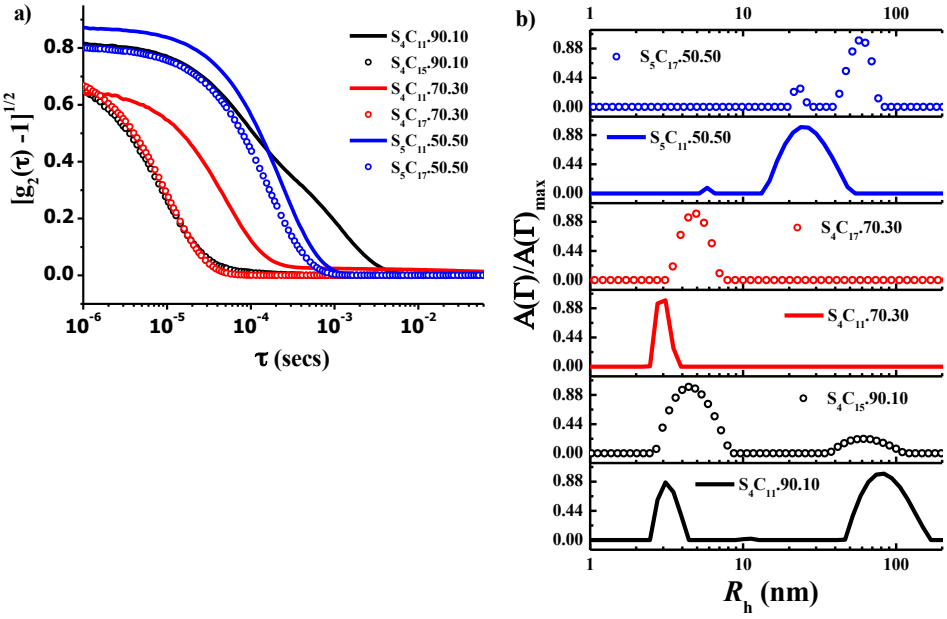


Figure 3-2. Light intensity second order autocorrelation functions (a) and hydrodynamic radii, R_h, distributions (b) of PS-b-PCHDs having different chain microstructure. The color coding by microstructure – blue for 50/50, red for 70/30, and black for 90/10 – is preserved throughout all of the figures in this Chapter.

Block copolymers with 90/10 and 50/50 microstructure show two decay modes, indicating two distinct populations of scatterers. While it may be tempting to describe the large scatters as micelles (in other words, well-defined systems resulting from microphase segregation), additional characterizations are necessary. As a result, I use the more general term ‘‘aggregate’’ at this juncture and focus on analyzing characteristic sizes determined from DLS measurements to gain insight into those populations.

In the case of *S4C11.90.10* and *S4C15.90.10*, the fast modes have radii <10.0 nm, (characteristics radius of = 5.0 nm) which is comparable to the size of a worm-like chain calculated using the Benoit–Doty equation.[86] The results indicate that the population having small size is due to the presence of single chains. However, in case of 50/50 microstructure any contribution that would be assigned to single chains was not observed. *S5C11.50.50* has a fast mode (R_h = 11 nm, calculated from $D_{z,app}$) that is almost double the size calculated for single chains, indicating presence of small aggregates made up of a few chains. For *S5C17.50.50*, the fast mode has an R_h = 30 nm, almost half the size of the slow mode showing an R_h = 60 nm. For the copolymers having a 70/30 microstructural ratio, analysis of the autocorrelation function suggests that there is only a single decay mode, corresponding to a population of scatterers having an R_h = 5.0 nm, which is similar to the size calculated for a worm-like chain.

To obtain information about the aggregate shape, the q-dependence of the apparent diffusion coefficients is calculated from the characteristic mean decay rates of the respective modes. Figure 3-3a and 3-3b show the apparent diffusion coefficient, D_{app} as a function of q^2 for each decay mode observed for the PS-b-PCHD copolymers. D_{app} for the slow modes of both

S_4C_{11}.90.10 (Figure 3-2a) and *S_4C_{15}.90.10* (Figure 3-2b) show no angular dependence, suggesting that the aggregates are spherical. The copolymers having 50/50 microstructure also show no angular dependence of D_{app} on q^2. The apparent z-average diffusion coefficient, $D_{z,app}$ is obtained by extrapolating $D_{app}(q)$ to $q^2 \rightarrow 0$.

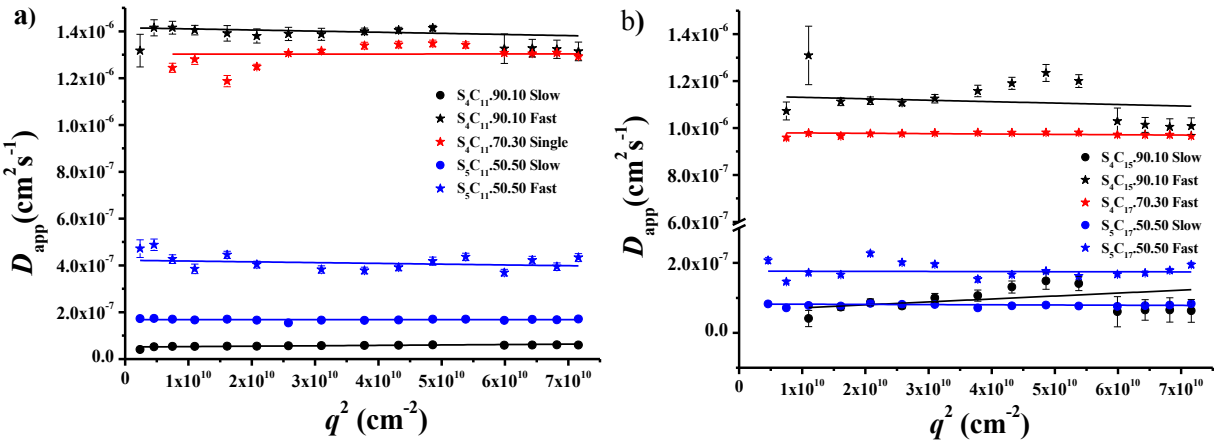


Figure 3-3. Apparent diffusion coefficient, D_{app}, of PS-b-PCHD copolymers having different chain microstructure as a function of the scattering wave vector, q^2. Data for the low molecular weight PS-b-PCHD copolymers are shown in (a) and data for the higher molecular weight copolymers are presented in (b). The sense of the colors is the same as in Figure 3-2.

The hydrodynamic radii are calculated by substituting the value of $D_{z,app}$ in the Stokes–Einstein relation and the values are summarized in Table 3-2. To measure the radius of gyration, R_g, of the aggregates, SLS measurements on PS-b-PCHD copolymers were performed. However, the copolymers having 90/10 and 50/50 microstructures in the PCHD blocks have populations of scatterers of more than one size and, as a result, the total average scattered light intensity measured represents contribution from the fast and the slow modes.

Table 3-2. Summary of results from DLS and SLS measurements on PS-b-PCHD copolymers.

Sample ID	Concentration c (mg mL^{-1})	$R_{h,app}$ (nm)	$R_{g,app}$* (nm)	$R_{g,calc}$** (nm)
S_4C_{11}.90.10	5.65	Slow: 91.5 Fast: 3.4	55*	4.7
S_4C_{15}.90.10	5.79	Slow: 72.6 Fast: 4.3	31*	5.3
S_4C_{11}.70.30	5.33	4.1	-	5.3
S_4C_{17}.70.30	4.86	4.9	-	5.4
S_5C_{11}.50.50	0.185	Slow: 28.4 Fast: 11.7	22*	4.9
S_5C_{17}.50.50	0.170	Slow: 62.0 Fast: 29.8	65*	5.6

* Apparent radius of gyration of the slow mode obtained by signal splitting. ** $R_{g,calc}$ of the PS-*b*-PCHD was obtained using $R_g = (R_{g,PS} \times R_{g,PCHD})^{1/2}$. R_g for PS was calculated using $R_g = Nb^{\upsilon}$, where υ is the Flory's solvent quality parameter (υ = 3/5 in a good solvent, THF). R_g for PCHD was calculated using the Benoit-Doty equation for a worm-like chain. Here, the persistence length, L_p was experimentally determined to be 0.65 nm for PCHD (90/10) in THF and contour length, L, calculated to be 53, depending on the molecular weight of the polymer.[86]

In order to accurately estimate the radius of gyration, R_g, eliminating the contribution of the fast mode to the total average scattered intensity is essential. The process of isolating the signal contribution of the slow mode from the total scattered light intensity was reported by Sedlak, which assumes that the slow mode is angularly dependent and the fast mode is angularly independent.[85] The normalized amplitudes of fast $A'_f(\theta)$ and the slow modes $A'_s(\theta)$ are obtained using

$$A'_s(\theta) = \frac{I(\theta)/I_B(\theta)}{1 + A_f(\theta)/A_s(\theta)} \tag{3.1}$$

and

$$A'_f = \frac{I(\theta)/I_B(\theta)}{1 + A_s(\theta)/A_f(\theta)} \tag{3.2}$$

where $A'_f(\theta)$ and $A'_s(\theta)$ are normalized excess scattering amplitudes of the two dynamic modes, $A_f(\theta)$ and $A_s(\theta)$ (where subscripts 'f' and 's' stand for fast and slow modes, respectively), assuming that $I(\theta)/I_B(\theta) = A_f(\theta) + A_s(\theta)$, I_B is the scattered intensity of the solvent. Dimensionless ratios $A_s(\theta)/A_f(\theta)$ and $A_f(\theta)/A_s(\theta)$ are calculated from amplitude of the characteristic decay rates of the slow and the fast modes. By plotting the ratio of the normalized amplitude of the slow mode at $q = 0$ and that at a given q value as a function of q^2, the value of R_g can be extracted from the slope of graph of the following equation:

$$\frac{I(\theta)}{I(\theta = 0)} = 1 + \frac{1}{3} R_g^2 q^2 \tag{3.3}$$

In order to confirm that the aggregation in block copolymers was not a solubility issue, a PS homopolymer (M_n = 4000 g mol^{-1}) and a PCHD homopolymer of 90/10 chain microstructure (M_n = 4000 g mol^{-1} having a hydroxyl end-group) were mixed in THF and dynamic light scattering measurements were performed. Figure 3-4 shows the distribution of hydrodynamic size for the mixture (PS + PCHD–OH homopolymers) overlaps that of the individual homopolymers, with sizes <10 nm confirming the presence of single chains only. Thus, the fact that larger sizes are seen in light scattering measurements of the PS-b-PCHD copolymers in THF confirms micellization and suggests that additional structural information can be gained by imaging the aggregates formed in solution.

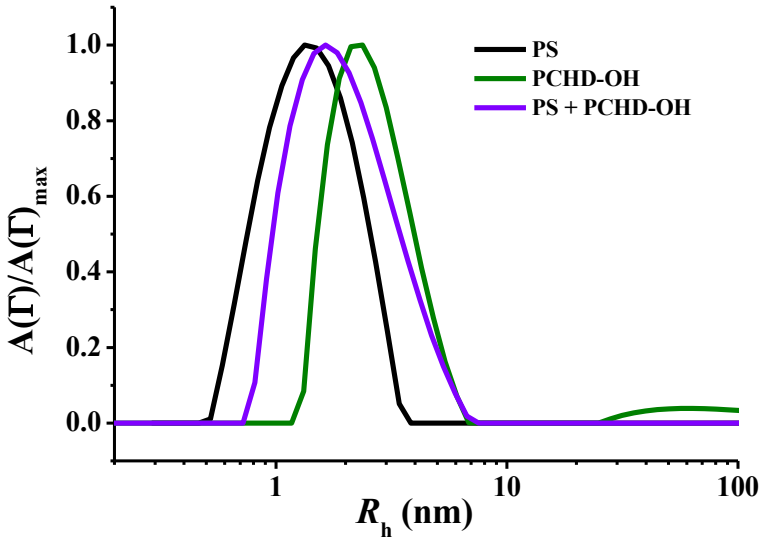


Figure 3-4. Distributions of hydrodynamic radii, R_h, of PS (black curve, PCHD-OH (~90/10, green curve and mixture of PS and PCHD-OH (purple curve at 5 mg mL^{-1} in THF).

AFM and TEM were used to examine the aggregate structures of the block copolymers having 90/10 and 50/50 chain microstructures. Films were cast from the same solutions that were utilized for light scattering, and AFM images of PS-b-PCHDs cast onto silicon substrates are presented in Figure 3-5. For $S_4C_{11}.90.10$ and $S_4C_{15}.90.10$ worm-like structures are seen in images A and B; these appear to be a string of spherical micelles because neither of the hydrophobic PS or PCHD blocks have an attractive preference for the hydrophilic silica. Consequently, as the solvent THF evaporates from the surface, the local concentration of the spheres increases, leading to formation of worm-like structures. It should also be noted that the local concentration of polymer is high because THF does not wet silicon – a significant portion of the substrate surface is bare and featureless, while areas where polymers deposit are densely covered. These effects also manifest in AFM images of the 70/30 copolymers. As seen in images C and D, copolymers S_4C_{11} and S_4C_{17} with 70/30 microstructure, show no distinct morphology. Rather, they appear to form a disordered polymer thin film. The thin film formation can be attributed to the presence of single chains (no micellization), even at the relatively high concentration of c = 5.0 mg mL^{-1} used in the DLS and SLS measurements. From images E and F, we observe ill-defined aggregates for the $S_5C_{15}.50.50$ and $S_5C_{17}.50.50$ copolymers, respectively. The density of polymeric structures is much lower (in comparison to images A–D) because the solution concentration is significantly lower.

Regular TEM images obtained by drop casting these PS-b-PCHD copolymers on a carbon film substrate reflect structures that are similar to the AFM images, except that we observe distinct spheres instead of worm-like structures for $S_4C_{11}.90.10$ and $S_4C_{15}.90.10$ as seen from the TEM images in Figure 3-6 (A and B). In top half of the image A of Figure 3-6, some

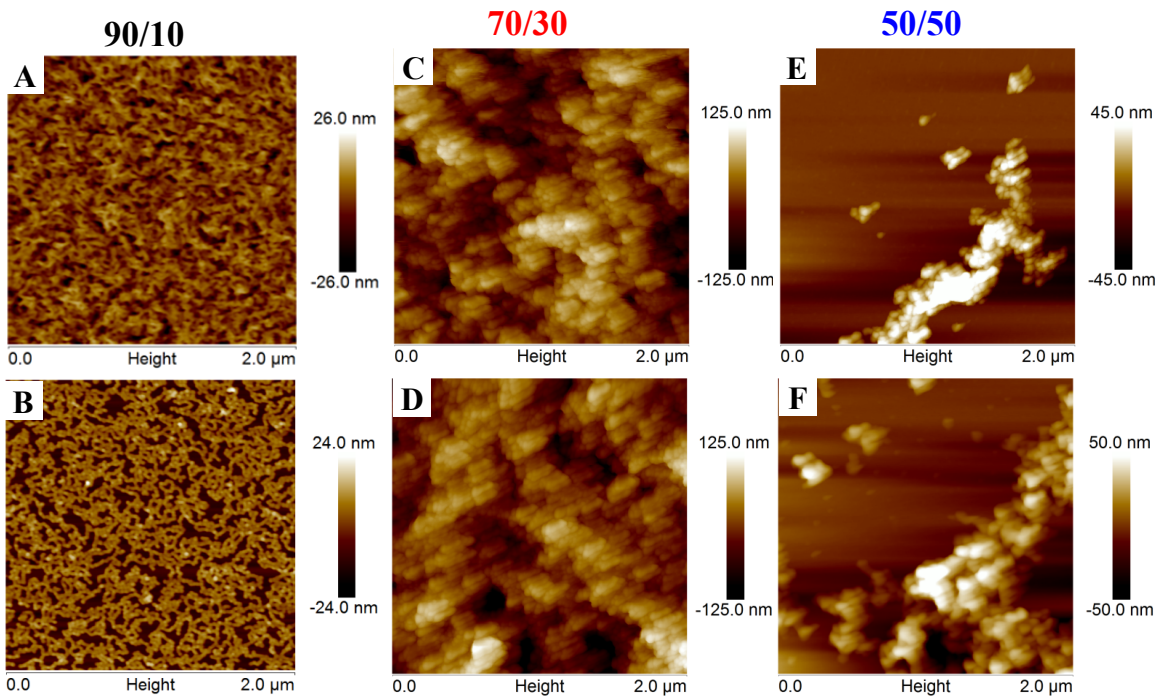


Figure 3-5. AFM images of PS-b-PCHD copolymers drop-cast to form thin films on clean silicon substrates. For an image of a given microstructure, the top image corresponds to the lower molecular weight PCHD while the bottom corresponds to higher molecular weight PCHD. Images A and B are for 90/10 microstructure at c = 5.0 mg mL^{-1}, which show the presence of worm-like structures. 70/30 microstructure block copolymers at c = 5.0 mg mL^{-1} show bulk polymer due to its existence as single chains in solution at c = 5.0 mg mL^{-1} in images C and D. Images E and F show ill-defined aggregates for 50/50 microstructures at c = 0.2 mg mL^{-1}.

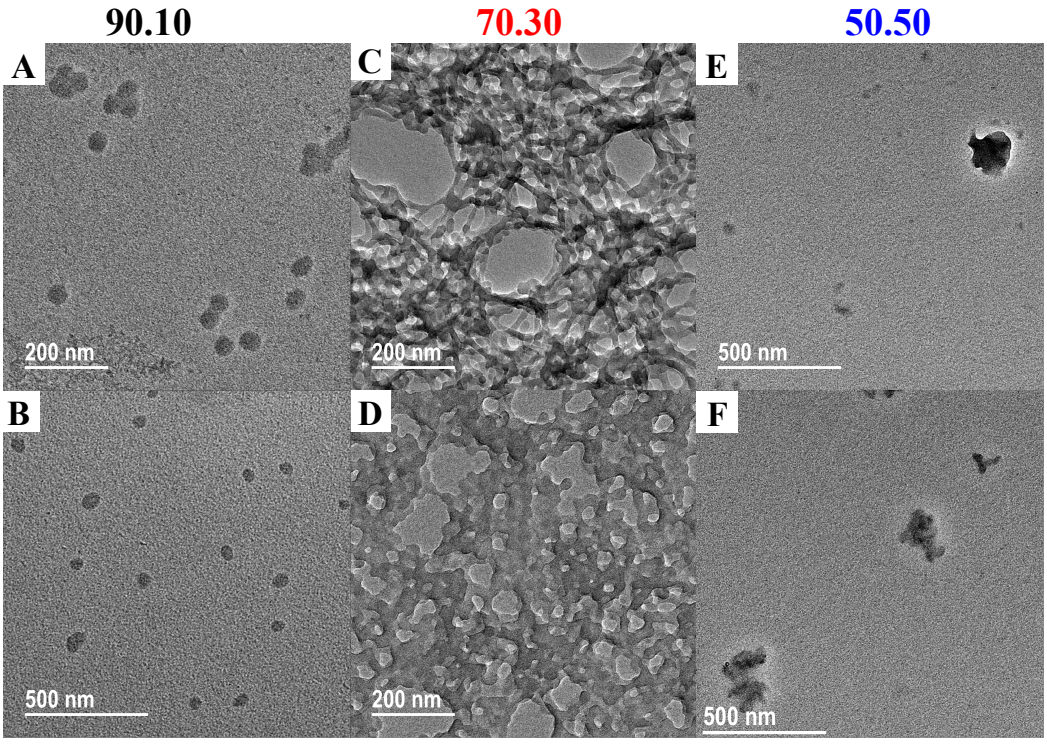


Figure 3-6. TEM images of PS-b-PCHD copolymers drop cast on carbon film grids. Images were obtained at the same solution concentration used for obtaining AFM images. For a given microstructure, the top image corresponds to the lower molecular weight PCHD while the bottom image corresponds to higher molecular weight PCHD. Images A and B show spherical micelles formed for the block copolymers having 90/10 microstructure. Copolymers having 70/30 microstructure show thin film formation (Images C and D) and 50/50 microstructure show presence of ill-defined aggregates, as seen in images E and F.

fused spheres are observed. These are likely due to an increase in concentration of spherical micelles the solvent evaporates during air drying as well as the relatively high concentration of polymer in the solution (~5.0 mg mL^{-1}) that was used to make the films for imaging.

Although we observe worm-like structures in AFM and spheres in TEM, we attribute these morphological differences surface and solvent evaporation effects. As noted earlier, THF does not wet the silicon substrate, and neither PS nor PCHD spread on the hydrophilic silicon substrate, either. Generally speaking, morphological changes that drive block copolymer systems away from their equilibrium morphology during thin film formation by solvent casting are known to occur, with kinetic (i.e., solvent evaporation rate and thermodynamic (e.g., surface energy, solvent type, and polymer concentration) effects[87-95] having significant influence. For example, simulations[89,90] and experiments[91-94] have shown that the formation and orientation of cylindrical domains in microphase segregating block copolymers depends on the rate of solvent evaporation from the film. Studies of micellar systems also demonstrate morphological changes upon solvent evaporation and drying to form thin films.[93-94] An early work by Krausch and coworkers demonstrated that polystyrene-b-poly(4-vinylpyridine) micelles coalesce to form worm-like structures, a behavior they attributed to local concentration that cause the spherical micelles to fuse as the solvent leaves the film.[92] Based on these studies and noting that the DLS studies signal micellar objects and TEM image A shows some indication of micelles coalescing on the hydrophobic carbon film grid, we speculate that the formation of worm-like structures observed in AFM images of 90/10 copolymers is caused by the dewetting and fusion during film formation on hydrophilic silicon.

Also similar to the AFM results, TEM images of films of 70/30 and 50/50 copolymers

cast onto carbon film grids show the presence of disordered thin films (C and D) and ill-defined aggregates (E and F), respectively. While the scale of the structures in the AFM and TEM images for the 70/30 copolymers may suggest the presence of large structures, the DLS results are definitive: Figure 3-2 shows a single decay mode corresponding to single chain sizes (at the high concentration of ≈5.0 mg mL^{-1}). As a result, when the solvent evaporates, a thin film is formed. Due to dewetting on the hydrophilic silicon substrate, the film is thick and without clear structural features. On the carbon film grid used for TEM imaging, areas of the surface are covered with a film that is too thick to image, but other areas showing a disordered, dried film (C and D) are readily found.

With DLS measurements, AFM and TEM imaging all showing that copolymers with 70/30 chain microstructure are unable to aggregate in THF, we examine whether the addition of a non- solvent methanol (MeOH) could force the system to aggregate. Small amounts of MeOH were added to solutions of *S_4C_{11}.70.30* and *S_4C_{17}.70.30* to promote aggregation. After each MeOH addition, the solution was allowed to equilibrate for at least one day before dynamic light scattering measurements were performed. The apparent R_h values (obtained from the apparent z-average diffusion coefficient, $D_{z,app}$, found by extrapolating the apparent diffusion coefficients to $q = 0$) as a function of the amount of MeOH added are presented in Figure 3-7 (a and b). The results show that when only a small amount of MeOH is added, only single decay mode is observed for both of the 70/30 block copolymers, suggesting that in these conditions, there are only single isolated chains in solution. Increasing the amount of MeOH added led to aggregation. This is confirmed by the appearance of a second decay mode in DLS measurements (data not shown) at 10 vol % and 7 vol % MeOH for *S_4C_{11}.70.30* and *S_4C_{17}.70.30*, respectively, which

when analyzed, corresponds to R_h values significantly larger than single chain sizes, as observed in Figure 3-7. Thus, aggregation could be forced by gradually increasing the quantity of MeOH, and we suspect that while MeOH is a poor solvent for both of the blocks, it is likely poorer for the high molecular weight PCHD blocks as compared to the low molecular weight PS blocks.

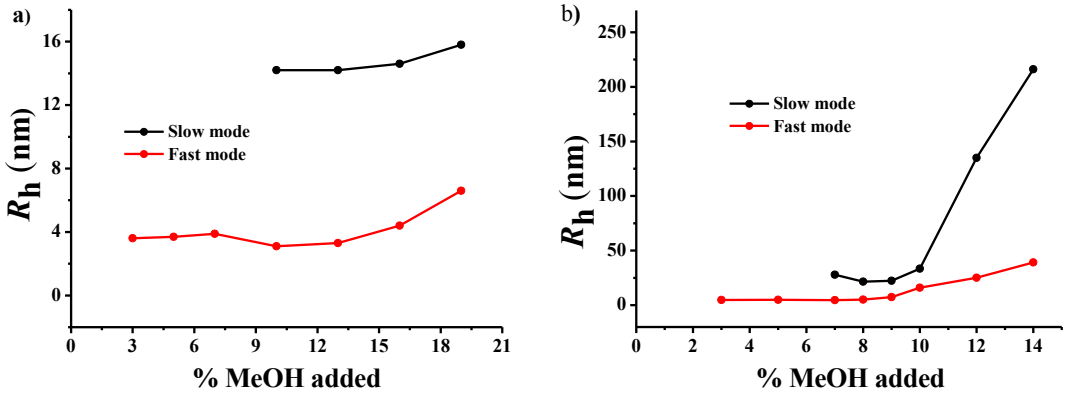


Figure 3-7. The appearance of a second mode, represented in the apparent hydrodynamic radius, R_h, as non-selective poor solvent MeOH is added to solutions containing *$S_4C_{11}.70.30$* (a) and *$S_4C_{17}.70.30$* (b), suggests that the block copolymers having 70/30 microstructure in the PCHD blocks can be forced to aggregate.

3.4.1 Micellization as a function of chain microstructure

The fact that only *$S_4C_{11}.90.10$ and $S_4C_{15}.90.10$* copolymers, both of which have 90/10 microstructures, form spherical micelles is a distinctive result. Under the assumption that the

PCHD–solvent interaction energy (on a per site basis) does not change with microstructure, we speculate that spherical micelle formation is facilitated by the ability of the PCHD chains of 90/10 microstructure to organize due to rod-like interactions between PCHD chains in the core of the micelle. This shape-driven interaction arises because 1,4-linkages along the backbone give the chain a rod-like configuration, perceived as a greater effective persistence length. On the other hand, increasing the number of 1,2-linkages causes the chain to cross itself as the chain contour is traced out, disrupting the ability of the chains to pack, as observed in case of the 70/30 and 50/50 microstructures. However, even though the chemical composition of the copolymer remains constant, one could argue that enthalpic effects could also be a driving force (in addition to the rod-like nature of PCHD chain that drives micellization in only one of the chain microstructures). Because the solubility of PCHD homopolymers with either 90/10 or 70/30 chain microstructures is as high as ~10 mg mL^{-1} in THF, we believe that rod-like interactions of the 90/10 microstructure enables microphase segregation of the PS and PCHD blocks. In principle, both PCHD and PS are soluble in THF, however, the fact that we see micelles in the 90/10 microstructure and also miscibility of low molecular weight PS when blended with PCHD homopolymer suggests that in solution, interaction between the semi-rigid, rod-like PCHD blocks is the main factor that drives self-assembly (spherical micelle formation). To provide additional clarity to the importance of shape-governed interactions on micelle formation, we constructed structural models of PCHDs having 90/10, 70/30 and 50/50 microstructures. While these static structures do not capture dynamical motions, they provide perspective on the effective persistence length of the chain as a function of the chain microstructure. As seen in Figure 3-8, the models seem to suggest that as the 1,2-content increases, the effective chain persistence length decreases.

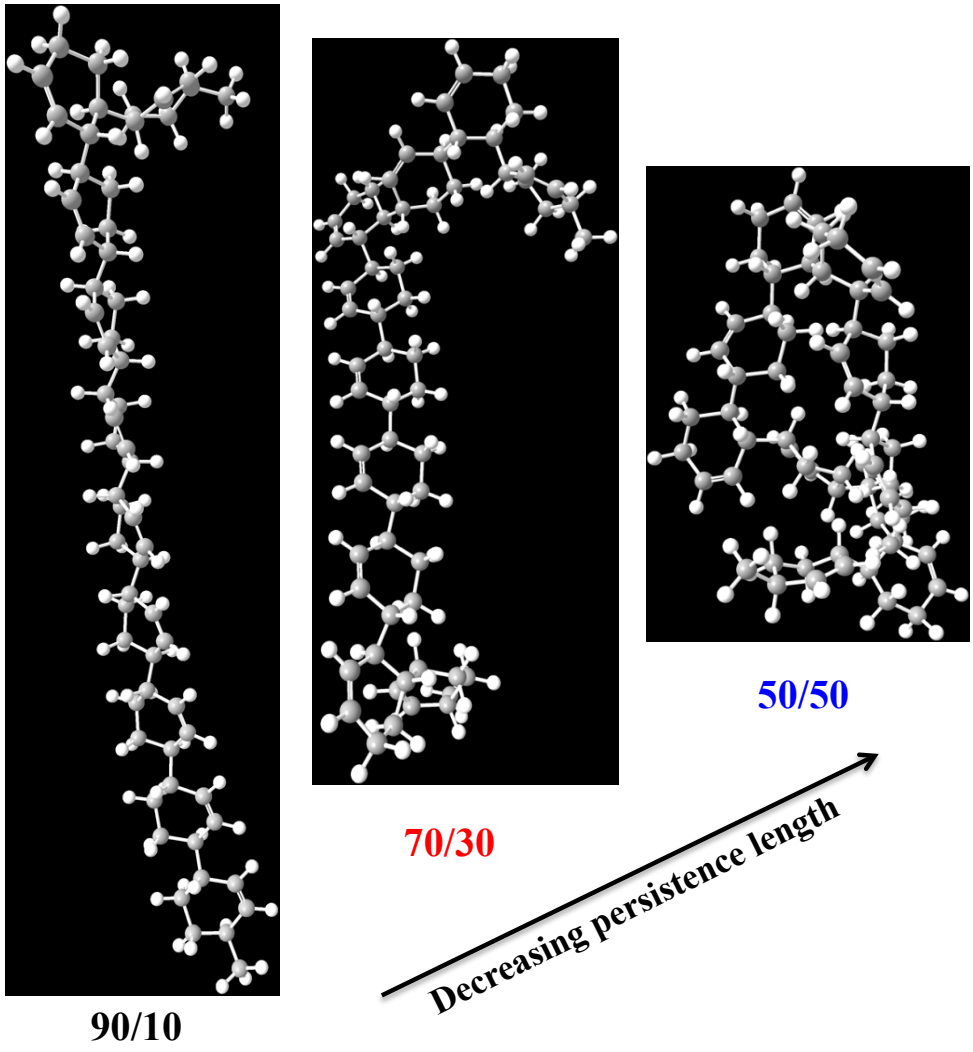


Figure 3-8. Model structures for PCHD oligomers suggest a decrease in persistence length (l_p) as 1,2-content increases from 10% (90/10) to 50% (50/50).

In constructing this model, it is known that 1,4-addition onto the growing polymer anion could be either cis or trans, while 1,2-addition is a trans addition.[94] These findings are based on results from Jagur-Grondinski and co-workers[94], who showed that creating a 1,4-linkage by monomer addition at the chain end could occur in either cis or trans fashion, making the polymer atactic overall. Assuming overall atacticity of the chain regardless of cis or trans addition for 1,4 -linkages, I drew the chemical models without considering any particular stereochemistry. On the other hand, when the chain grows by adding a repeat unit through a 1,2-addition, trans addition dominates because of the steric hindrance. Also, 1,3-cyclohexadiene has two double bonds as a part of cyclic ring system, making half-chair as the most preferred conformation. During the addition of a repeat unit to the end of the growing polymer anion, sampling of another conformation by the monomer while being added at the chain end is highly restricted. From geometric arguments, 1,2-linkages in the PCHD backbone tend to reduce the persistence length of the chain because consecutive bond vectors are nearly opposed. Consequently, due to the perceived rod-like configuration of the 90/10 blocks, it is possible for the PCHD blocks to arrange themselves in a fashion that promotes self-assembly into a micellar structure by reducing defect energy. This reduction in the defect energy helps to compensate for the entropic penalty for stretching the selectively solvated PS corona chains and the creation of an interface between the blocks. As the effective rod-like configuration decreases with increasing 1,2-content, the shape-driven packing becomes more difficult, leading to either no aggregation or ill-defined aggregates. In the case of the 50/50 chain microstructure, ill-defined structures are obtained due to reduced solubility of the polymer in THF. I posit that the high 1,2-content leads to a sterically-hindered configuration due to the chain crossing itself along its contour path, making it difficult for solvent molecules to penetrate, interact and swell the chain.

Nevertheless, the notion of 90/10 chain microstructure having a more rod-like character as compared to other microstructures is somewhat contradictory to the notion that T_g values measured for the block copolymers provide insight into stiffness. The copolymers with 90/10 have the lowest T_g values as compared to 70/30 and 50/50 copolymers. It is believed that even though T_g values increase with increasing 1,2-content, they are indicative of only the restricted chain movements but not necessarily indicative of high persistence lengths.

3.5 Conclusions

The self-assembly behavior of a series of PS-b-PCHD copolymers was explored in THF, a solvent slightly selective for PS. The microstructure of the PCHD blocks was carefully tuned with anticipation that it would lead to a change in chain rigidity without changing the chemical nature of the polymer and, therefore, the nature of the intermolecular interactions that govern phase behavior. PS-b-PCHDs with 90/10 PCHD microstructural ratios form spherical micelles, while 70/30 and 50/50 microstructural ratios exist as single chains and ill-defined aggregates, respectively. It is speculated that rod-like configuration of 90/10 microstructure, as compared to 70/30 and 50/50 and as shown by chemical models, facilitates organization of PCHD chains, allowing spherical micelles to form. The rod-like configuration enables the chains to pack in a fashion that reduces the defect energy and compensates for the entropic penalty paid by the extended PS corona chains (due to solvent selectivity) and creating an interface between the blocks. These behaviors clarify the link between the intrinsic chain rigidity and its impact on the self-assembly in PCHD-containing block copolymers. Certainly, microstructure has important implications on chain configuration and packing in soft matter ensembles, and the results also indicate that the classic definition of persistence length and stiffness do not go hand-in-hand.

Chapter 4: Solution Self-assembly of Polystyrene-b-Polyisoprene Miktoarm Star Copolymers: Effect of Architecture and Conformational Asymmetry

4.1 Abstract

Solution phase behavior of architecturally-complex block copolymers is ambiguous as the current systems lack systematic variation in their molecular characteristics. In this study, we explore how topological complexity, introduced through systematic changes in architecture and composition, impacts micelle formation of miktoarm star block copolymers. The solution properties and morphology of nanoscopic aggregates formed from anionically-synthesized polystyrene-polyisoprene (PS-PI) miktoarm star copolymers is investigated in n-hexane, a thermodynamically good solvent for PI. Light scattering measurements are used to determine the hydrodynamic size and aggregation number, and surface and solution morphologies were imaged using atomic force microscopy and cryogenic transmission electron microscopy. All block copolymers formed spherical micelles, though changes in micelle size with the number of arms and length of the solvated PI block was observed. An "equivalent diblock" model is found to be useful for capturing this trend, and from that model I speculate the sharp core/corona interface resists any broadening in order to compensate for the entropic penalty paid due to corona chain stretching, rather than allowing a change in the aggregation number of the spherical micelles. Thus, these studies of the self-assembly of PS-PI miktoarm star copolymers establish a strong experimental correlation between topological constraints in chains and micellar properties. Thus, introducing controlled changes in macromolecular design through variation of copolymer architecture and composition provides additional avenues for manipulating micelle properties, advancing their applicability in areas such as drug delivery, environmental remediation and template synthesis of nanomaterials.

4.2 Introduction

Controlling the size and shape of micelles formed by microphase separation of amphiphilic block copolymers in a selective solvent is critical for tuning micelle properties, which enables their technological application.[1,66,67] The ability to precisely control or modify the size or shape of micelles adopted due to packing of chains in the phase segregated core-corona domains enables their applicability in technologies such as transport of hydrophobic drugs, emulsification of solutions, and surface modification, to name a few.[34,96-99] Parameters such as block size, composition, architecture and solvent selectivity provide the desired control over size, morphology and aggregation number (number of chains that constitute a micelle. Moreover, these parameters directly impact geometric and free volume restrictions that contribute significantly toward the packing of polymer chains within the micellar structure.[96-99] Theoretical studies[32,100] and experimental evidence[101,102] show that due to topological differences, architecturally-complex block copolymers are more complex in their microphase segregation behavior in comparison to their linear counterparts. As a result, there is growing interest in exploiting topological design, which is aided through advances in synthetic strategies and efficient coupling chemistries, as a way to access complex architectures.

One class of simple geometrically constrained, but topologically sophisticated materials is miktoarm star copolymers, where the polymer chains are geometrically constrained by virtue of being attached to the central junction point. In a theoretical treatment based on a single chain model, Milner first demonstrated the impact of geometric constraints on stretching of chains in the melt phase, comparing blocks that are elastically similar and holding the total volume

fraction of the two blocks constant.[32] It was observed that order-order transition (OOT) boundaries of an A_2B star copolymer shifted to a higher volume fraction when compared to phase behavior of linear AB diblock. This shift arises due to a constraint enforced by the junction point that causes two chains of the A polymer to stretch differently in the strong segregation limit.[32] This elegant example has served as touchstone, motivating myriad studies of melt phase behavior of architecturally-complex copolymers.

Studies of self-assembly of miktoarm star copolymers in solution have provided a plethora of interesting structures, which may or may not be accessible through assembly of linear diblock copolymers.[42-44,48,102,103] Lodge and coworkers showed that multi-compartment phase-separated structures, such as hamburger-shaped micelles, toroids, segmented cylinders and ribbon-like structures, for example,[102] were formed by self-assembly of ABC terpolymers having arms of poly(ethyl ethylene), poly(ethylene oxide) and poly(perfluoro propylene oxide). These results are stimulating because of the unusual structures formed, and they provide conceptual motivation for the idea that other block types having different intermolecular interactions would diversify the type of structure formed. However, topologically-complex block copolymers based on neutral polymers, like polystyrene (PS) and polyisoprene (PI) remain important model systems that are distinctly useful for studies linking macromolecular design characteristics and solution phase behavior.[43-47,103,104] A number of efforts have been dedicated to examining the self-assembly behavior of PS/PI miktoarm stars in a PI-selective solvent. By performing light scattering measurements, micelle formation was observed, with sizes and aggregation numbers largely controlled by length of the non-solvated PS blocks that form the micelle core.[43,44,103,104] Hadjichristidis and coworkers also examined the micellization behavior of PS_8PI_8 miktoarm star

copolymers in n-decane, another PI selective solvent. The ρ-ratios (defined as R_g/R_h, the ratio of the radius of gyration, R_g, to the hydrodynamic radius, R_h) suggested that elongated spherical structures were observed for compositionally symmetric stars while stars with longer PI blocks formed more spherical structures.[103] These studies bring out subtle complexities in phase behavior introduced by varying the composition and architecture, which affects the shape and size of the micelles or aggregates.

The topological design of block copolymers imparts geometric constraints that influence stretching and packing of chains. These effects can manifest at the core-corona interface, thereby altering the interfacial curvature and causing micelle-forming systems to adopt a different morphology. For example, Borsali et al.[47] observed a non-spherical shape and higher aggregation number for micelles formed from cyclic PS/PI block copolymers in n-heptane as compared to the analogous linear polymers at the same composition and molecular weight. Cyclization causes a topological restriction that limits stretching of the PI corona blocks, resulting in giant worm-like structure so that the PS core chains are sufficiently shielded from contact with the solvent.[47] With the view that the free energy of a micelle is a balance between the penalty for chain stretching, the cost of creating an interface, and the energetic gain due to non-solvated blocks minimizing contact with solvent, restrictions in chain stretching due to topological design has the potential to alter the free energy of micelle formation considerably.[48]

While all of the studies highlighted above conceptually demonstrate the utility of chain topology as a way to vary self-assembled structures, most involve linking multiple block chemistries or remain limited in the number of architectures explored. In this study, we aim to

understand the links between macromolecular design and structure in solution for a set of miktoarm star copolymers whose architecture and has been systematically varied at two different compositions. The study specifically addresses the impact of topological restrictions on solution self-assembly of A_n-B_m copolymer systems.

In this study, a set of six A_n-B_m miktoarm star block copolymers composed of PS and PI chains attached to a central multichlorosilane core, are studied in n-hexane, a PI-selective solvent. To systematically study the impact of branching, the number of arms of PS and PI are kept equal with n = m = 1, 2 and 4, yielding a series consisting of diblocks, 4-arm and 8-arm star copolymers, respectively. Because the number of arms of both PS and PI blocks are kept equal, we denote the miktoarm stars as PS_n-PI_n. To study the effect of compositional asymmetry, another set of star copolymers are synthesized in which the molecular weight of the PI block is doubled while keeping the molecular weight of PS arm constant. After self-assembly of the stars in n-hexane, sizes of the aggregates in solution are measured using light scattering techniques, surface and solution morphologies imaged using atomic force microscopy (AFM) and cryogenic transmission electron microscopy (cryo-TEM), respectively.

4.3 Experimental section

4.3.1 Synthesis of PS_n-PI_n miktoarm star copolymers

The materials characterized in this study were obtained as a part of the collaborative effort with the Mays group. The synthesis was successfully completed by Dr. Weiyu Wang. Synthesis of each miktoarm star copolymers was carried out in a custom-made glass apparatus

equipped with break-seals. The glass apparatus is washed with n-BuLi and rinsed with benzene to scavenge all of the water and any impurities. All chemicals were purified and ampuolized by methods detailed elsewhere.[49,105] Anionic polymerization was used to synthesize the star copolymers with polymerizations initiated by sec-BuLi in benzene. The PS_1-PI_1 diblock copolymers were synthesized sequentially, with polymerization of styrene first, followed by crossover to isoprene. All polymers were purified by precipitation into degassed methanol. For the 4-arm and 8-arm stars, a multichlorosilane linking agent that attaches the polystyryl lithium anion, $PSLi^-$ and polyisoprenyl lithium anion $PILI^-$ arms to the core linker was used. PS_2-PI_2, the 4-arm star copolymer, was created by first adding 2 equivalents of polystyryl lithium anion, $PSLi^-$ into a benzene solution containing $SiCl_4$. Completion of the linking reaction, verified using size exclusion chromatography (SEC), is indicated by appearance of a second peak at a shorter retention time (and concomitant decrease in the "arm" peak). Following this, 2.2 equivalents of $PILi^-$ is added, driving the syntheses of 4-arm mikto star copolymer to completion. In order to synthesize the 8-arm star copolymer, PS_4-PI_4, the linking agent $Si[CH_2CH_2Si(CH_3)Cl_2]_4$ ($SiCl_8$) was first made by hydrosilylation of tetravinylsilane with dichloromethylsilane, as outlined by Uhrig and Mays.[104] To a benzene solution containing $SiCl_8$, 4 equivalents of $PSLi^-$ were added and the evolution of the 4-arm product was again monitored by SEC. Excess $PSLi^-$ was then added to drive the formation of 8-arm star to completion. The excess $PSLi^-$ was removed later by solvent fractionation using a toluene-methanol mixture.[105] The molecular characteristics of the miktoarm stars are presented in Table 4-1.

Table 4-1. Molecular characteristics of the PS_n-PI_n miktoarm star block copolymers as determined by size exclusion chromatography (SEC).

Sample ID	Total number of arms	Target M_w (kg mol^{-1})	M_w (kg mol^{-1})	S/I[a]	PDI
PS_1-PI_1	2	15-15	16.9 -16.3	1	1.04
PS_1-PI_1		15-30	16.9 - 30.3	0.5	1.03
PS_2-PI_2	4	30-30	28.6 - 30.9	1	1.07
PS_2-PI_2		30-60	34.6 - 74.8	0.5	1.06
PS_4-PI_4	8	60-60	62.9 - 74.8	1	1.07
PS_4-PI_4		60-120	62.9 - 116.8	0.5	1.06

[a]Refers to compositional asymmetry, expressed as the ratio of PS:PI.

4.3.2 Characterization of self-assembled structures in n-hexane

Dynamic light scattering. Light scattering measurements were performed using a four-detector ALV goniometer system described previously in Chapter 2. For the PS_n-PI_n stars, data was recorded for approximately 1.5 mL of dilute polymer solutions having a concentration, *c* of 6 mg mL^{-1} and equilibrated for at least one week at room temperature. The solutions were contained in Teflon capped, dust-free 10 mm borosilicate glass cuvette. The measurement time for every sample was 300s at each angle, with measurements taken at 16 angles. The toluene bath contained in the VAT that maintained the sample temperature at 25±0.1 ºC throughout the measurement.

Static light scattering. Static light scattering measurements were made using the same four-detector ALV goniometer system described earlier. Zimm plots were constructed using data obtained at 16 angles and several concentrations. For each solution of a given concentration, the scattered intensity was measured for 10s at every angle. The measurement at each angle is repeated three times and the constraint that the variation in the measured scattered intensity be less than 3% is imposed. Any variation above this threshold required the measurement be repeated until the criterion is met. The average value of scattered light intensity is used to construct Zimm plots using the ALV software. The Zimm plots are shown in the Appendix A.

Atomic force microscopy. A Veeco Instruments Nanoscope IIIa multimode atomic force microscope was used to image polymer films in tapping mode using silicon cantilevers (purchased from Applied NanoStructures, Inc., Mountain View, CA). Uniform polymer films were prepared by spin coating the polymer solution onto diced silicon substrates of 10mm × 12mm (obtained from Silicon Quest) that were cleaned using piranha acid. Details of the silicon wafer cleaning procedure are outlined in a previous publication.[106] 50 μL of the polymer solution was pipetted on the clean silicon substrate and spun for 2 mins at 2000 rpm to obtain a uniform coating of polymer nanostructures, which were then imaged.

Cryogenic transmission electron microscopy. Vitrification of the self-assembled polymer aggregates in n-hexane was carried out in a GATAN's controlled environment vitrification system (CEVS). 10 μL of the sample solution was syringed onto a lacey carbon grid (mesh size of 200) held in place using tweezers. To slow the evaporation of n-hexane during the vitrification process, the sample solution was previously cooled to 4 °C in a refrigerator and immediately cast

onto the grid. Following this, the sample was blotted using absorbable pads for 5.0s and then plunged into a cup of liquid nitrogen at -175 °C. The grid was allowed to remain submerged in liquid nitrogen for two minutes and then transferred, under liquid nitrogen, to previously cooled Gatan Ultra 626 cryo-holder and stage. Imaging under cryo conditions was performed using Zeiss Libra 200 MC (200 keV) transmission electron microscope that is equipped with a Gatan UltraScan US1000XP CCD camera.

4.4 Results and discussion

4.4.1 Solution behavior of miktoarm stars

The self-assembly characteristics of PS_n-PI_n miktoarm star copolymers was investigated in n-hexane, a thermodynamically good solvent for the PI block, at a concentration, *c*, of 6 mg mL^{-1}. The star copolymers formed nanoscopic sized aggregates, as indicated from DLS measurements. Figure 4-1A shows the light intensity autocorrelation functions for all six star copolymers. The correlation functions are analyzed by applying a multi-exponential fit to yield the normalized amplitude distribution of the mean decay rates, which provides information about the population distribution of scatterers in solution. The normalized amplitude distribution of mean decay rates, shown in Figures 4.1B and 4.1C, reflect the impact of topology for compositionally symmetric and asymmetric stars, respectively. The distributions for diblock copolymers PS_1-PI_1 (15k-15k and 15k-30k) are narrow and have the smallest (average size. Broader distributions are seen for the 4-arm star PS_2-PI_2 (30k-30k) and 8-arm stars, PS_4-PI_4 (60k-60k and 60k-120k) and a shift in the population distribution of scatterers towards larger size is evident, with sizes almost doubling upon doubling the number of arms attached to the central

Figure 4-1. (A) Second order light intensity autocorrelation functions of PS_n-PI_n miktoarm stars in n-hexane at c = 6 mg mL^{-1}. (B) and (C) show the distribution of hydrodynamic sizes. (B) depicts change in the distributions as a function of architecture for stars of symmetric composition and (C) shows distributions of compositionally asymmetric stars. The color schemes representing the star copolymers are: diblocks (n = 1; black), 4-arm stars (n = 2; green) and 8-arm stars (n = 4; red).

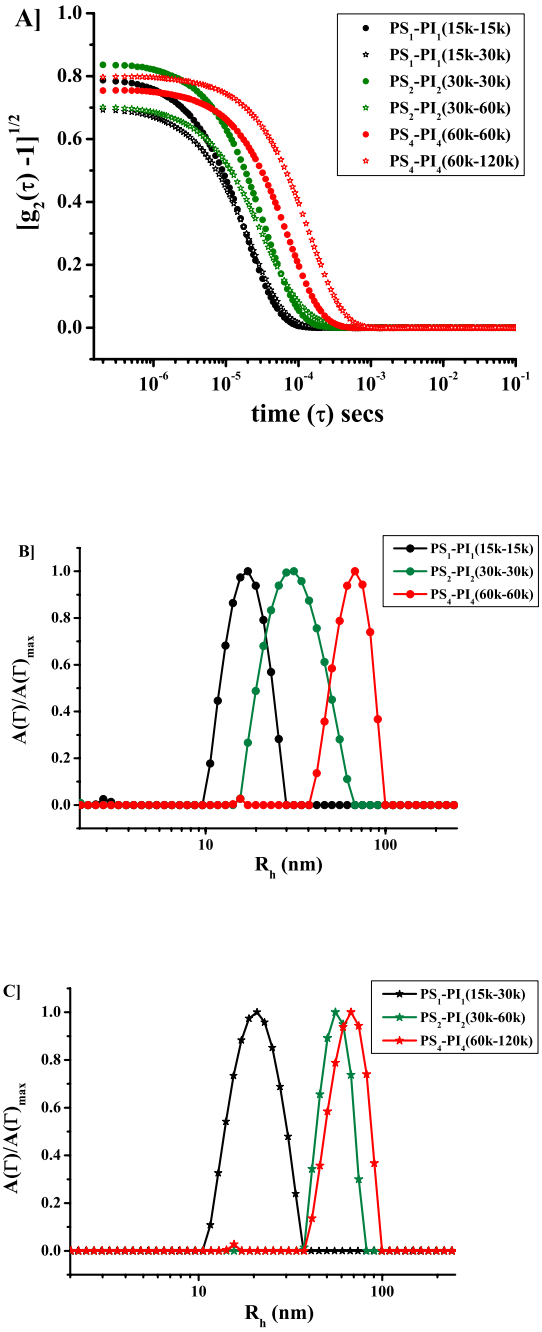


Figure 4-1 continued

core. These trends are quite striking for the "symmetric" stars having S/I=1 and generally hold for the "asymmetric" stars, likely due to the fact that the MW of the PI arms of PS_2-PI_2 (30k-60k) star is substantially greater than the target molecular weight.

A single population of scatters are observed in solution for each star allowing the mean decay rate, Γ, of the scattering species to be extracted by applying a double exponential fit. By applying a double exponential fit to the scatterer population, I am able to verify that any distribution that would be attributed to very small sized scatterers is due to noise. This approach eliminates any misinterpretation from assuming and using a single exponential fit only. From the angularly-dependent mean decay rates, the value of the angularly-dependent apparent diffusion coefficient, D_{app}, is calculated. By plotting $D_{app}(q)$ as a function of q^2, the shape of the aggregates can be inferred. As shown in Figure 4-2A, independence of $D_{app}(q)$ on q^2, indicates that spherical aggregates are formed upon self-assembly of the compositionally symmetric diblock, 4-arm stars and 8-arm stars. Figure 4-2B shows similar behavior for the asymmetric stars.

The z-average diffusion coefficient, $D_{z,app}$, at c = 6 mg mL^{-1} is obtained by extrapolating $D_{app}(q)$ to $q^2 \rightarrow 0$. This is an apparent diffusion coefficient by virtue of being determined at finite concentration, and the corresponding apparent hydrodynamic radii, $R_{h,app}$ is calculated using Stokes-Einstein relation. These data, summarized in Table 4-2, capture the effect of architecture on the size of the micellar aggregates. Aggregate size doubles when the number of arms double for the symmetric star copolymers: $R_{h,app}$ = 17 nm for PS_1-PI_1 (15k-15k), $R_{h,app}$ = 29 nm for PS_2-PI_2 (30k-30k) and $R_{h,app}$ = 62 nm for PS_4-PI_4 (60k-60k).

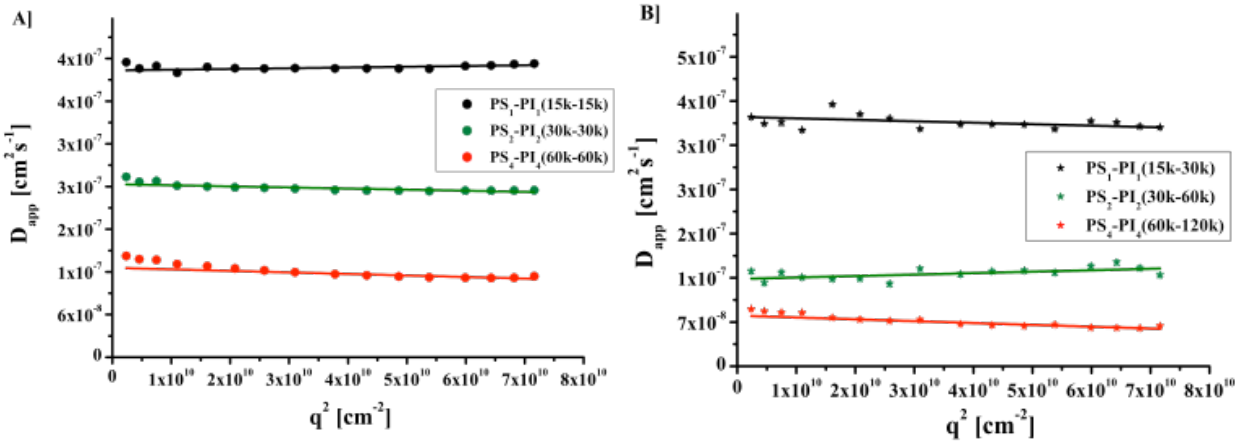


Figure 4-2 Apparent diffusion coefficient, $D_{app}(q)$, of PS_n-PI_n miktoarm stars copolymers as a function of the square of the scattering wave vector, q^2. Data for the symmetric stars are shown in (A) and data for the asymmetric stars are presented in (B). The sense of the colors is the same as in Figure 4-1.

Table 4-2. Solution properties and morphology of the self-assembled aggregates of PS_n-PI_n miktoarm star block copolymers.

Sample ID	Star M_w (kg mol^{-1})	$R_{h,app}$ (nm)	$R_{g,app}$ (nm)	ρ-ratio	Surface Morphology[a]	Solution Morphology[b]
PS_1-PI_1	15k-15k	17	22	1.17	W	S
PS_1-PI_1	15k-30k	17	20	1.17	W	S
PS_2-PI_2	30k-30k	29	25	0.87	W	S
PS_2-PI_2	30k-60k	51	44	0.87	W	S
PS_4-PI_4	60k-60k	62	65	1.04	S	S
PS_4-PI_4	60k-120k	96	59	0.61	S	S

Morphologies of the aggregates were imaged using AFM[a] in tapping mode and Cryo-TEM[b], respectively. The letters 'W' and 'S' refer to "worm-like" and "spherical" morphologies, respectively.

The compositionally asymmetric stars, however, have hydrodynamic sizes that increase by a different factor as the arms are doubled: The size triples, from an $R_{h,app}$ = 17 nm for PS_1-PI_1 (15k-30k) to an $R_{h,app}$ = 51 nm for PS_2-PI_2 (30k-60k), and then doubles to a value of $R_{h,app}$ = 96 nm as one moves to the 8-arm star copolymer PS_4-PI_4 (60k-120k). To further evaluate the trends in aggregate size with architectural and compositional variation, characteristics such as apparent radius-of-gyration, $R_{g,app}$ and ρ-ratio of were evaluated using static light scattering measurements.

Both architecture and composition increase the apparent radius of gyration, $R_{g,app}$, mirroring trends seen with $R_{h,app}$ data, as can be seen from the data presented in Table 4-3. Further, the ρ-ratios that reveal the distribution of mass in an aggregate were calculated for all of the star copolymers. The ρ-ratios of the diblocks are ~1.0, suggesting vesicles or oblate ellipsoids or a softer PS core with presence of solvent molecules. The aggregates formed from the 4-arm star copolymers, have ρ-ratios ~0.8, indicating the presence of hard spheres. This is also observed in case of asymmetric 8-arm stars. The values of ρ-ratios presented here are just suggestive of aggregate shape. A number of factors such as noise, exponential fitting and broad hydrodynamic distributions contribute to deviations in these calculated values. Therefore, later in the dissertation I provide complementary evidence in the form of microscopic images to confirm the interpretations from scattering.

Further, to understand the arrangement of chains within these aggregates, we quantitatively determine the packing density of chains at the core-corona interface by calculating the aggregation number, Q, radius of the core, R_{core} and interfacial surface area occupied by the PI corona chains, S, for all of the star copolymers. The value of Q is calculated from Zimm analysis of SLS measurements, while R_{core} and S are calculated using the Zhulina and Borisov's model for spherical micelle in a selective solvent, as shown in Appendix A. The obtained values after calculations are summarized in Table 4-3.

Trends in aggregation number for compositionally symmetric and asymmetric stars show a decrease in the number of chains per micelle as the number of arms increases. This seems reasonable with the view that 4-arm and 8-arm stars are comprised of 2 and 4 linear equivalent

Table 4-3. Properties of micelles/aggregates of the self-assembled miktoarm stars. Calculated equivalent diblock, Q_{eq}, radius of the PS core, R_{core} and area per macromolecular chain, S, occupied by the PI corona of the spherical micelles.

Sample ID	Star M_w (kg mol^{-1})	$M_{w,app}$ [a] (g mol^{-1})	$R_{g,app}$ [a] (nm)	Aggregation number, Q [a]	Calculated equivalent diblock chains, Q_{eq}	R_{core} [b] (nm) with φ_{core} = 0.8	Area per PI chain at the interface S (nm^2)
PS_1-PI_1	15k-15k	1.9×10^6	22	64	64	7.2	10
PS_1-PI_1	15k-30k	2.3×10^6	20	51	51	5.4	14
PS_2-PI_2	30k-30k	2.1×10^6	25	35	70	7.4	20
PS_2-PI_2	30k-60k	2.5×10^6	44	25	50	6.7	22
PS_4-PI_4	60k-60k	2.6×10^6	65	22	88	8.0	38
PS_4-PI_4	60k-120k	3.2×10^6	59	18	72	7.5	40

[a]Determined from Zimm analysis of SLS data. [b]Radius of PS core calculated according to Zhulina et al.[40,106]

diblocks, respectively, stitched together at a central junction point. This re-definition of the macromolecular "building block" of the micelle allows us to recast how we think about the number of chains that constitute a micelle by computing Q_{eq} – the aggregation number based on equivalent diblock copolymers: Q_{eq} = nQ. The Q_{eq} forming the micelle should increase proportionally with the number of arms even though the Q decreases. This is witnessed for example in case of the symmetric 4-arm star, where Q is approximately one half Q value of the diblock but their Q_{eq} values are approximately equal. Similarly, Q of the 8-arm star is one third the Q of the diblock, while their Q_{eq} values are similar. In fact, given the sensitivities inherent in the extrapolations used in the Zimm analysis of SLS data and their impact on $M_{w,app}$, the agreement is quite good.

As discussed earlier, the increase in aggregate size for asymmetric stars of a given composition follows a different trend, which may be attributed to the differences in stretching of the corona chains, especially near the interface. As seen from Table 4-3, the radius of the PS core, R_{core}, shows minor changes across the stars that are studied. This suggests that the PS core is highly collapsed and the topological constraints enforced by the central junction point causes the PI corona arms to be more stretched, which reflected in the number of chains occupying a given area at the interface.

The increase in surface area per macromolecule, S, with the number of arms confirms that core sizes remain constant and primary contribution to increase in the aggregate size is from stretching of PI arms at the interface. As for the diblocks, the aggregation number is smaller for the asymmetric 15k-30k as compared to the symmetric 15k-15k, with their micelle sizes being

almost the same. The PI corona swells considerably and, in order to compensate for the entropic penalty due to stretching, the aggregation number is reduced and the core tends to be more collapsed. A similar effect is observed in the case of the 8-arm star copolymers. Evidently, the collapse of the core due to strong selectivity of n-hexane and PI chain stretching are an important factors that influence size.

4.4.2 Morphology studies

The aggregates formed in n-hexane were imaged by AFM and cryo-TEM. Both worm-like structures and spherical micelles were seen in AFM images of the films cast on silicon substrates, while only spherical micelles were seen in cryo-TEM images.

As seen in the AFM images presented in Figure 4-3, the diblocks (n=1) and 4-arm star copolymers (n=4) of symmetric and asymmetric compositions adopt worm-like morphologies. These structures are believed to result from fusion of spherical micelles as the solvent evaporates during the spin coating process. The micelles formed from the symmetric and asymmetric 8-arm star copolymers, PS_4-PI_4, remain as spheres on the surface with their structure unaffected by solvent evaporation. These star copolymers are topologically constrained due to highest number of polymer arms (degree of branching) amongst the star copolymers that have been studied. The PI corona chains of the micelle are highly extended, as would be suggested by the area per PI arm. This extension strongly shields any intermicellar hetero-contacts between PS cores of neighboring micelles, thus prohibiting interpenetration of the corona chains required for the fusion of spheres into worm-like structures. The impact of shielding by the swollen PI corona is

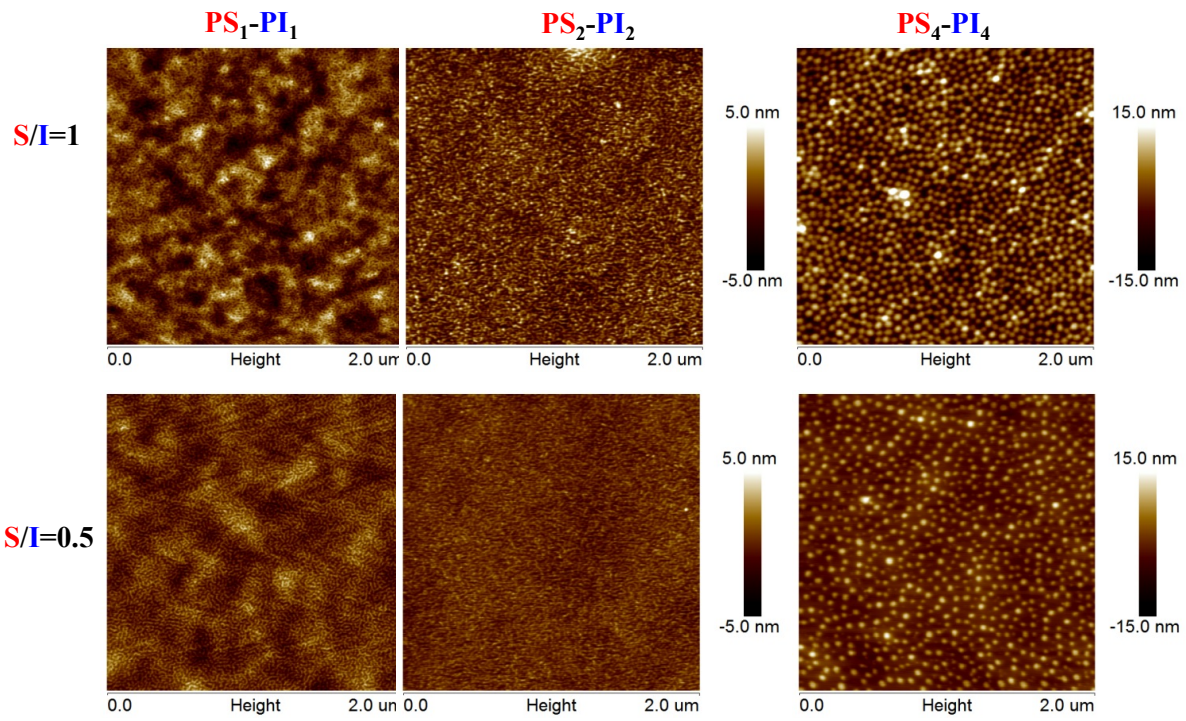


Figure 4-3. Surface morphologies of PS_n-PI_n miktoarm star copolymers spin cast from n-hexane at a concentration, *c* of 6 mg mL^{-1}. In the top row, from left to right, the number of chains about the central junction increases while the composition is fixed for S/I = 1. The second row reflects the same increase in number of arms but the star composition is asymmetric, S/I = 0.5. The impact of composition on morphology of the stars at a fixed number of arms manifests by comparing the images in the top (S/I = 1) and bottom (S/I = 0.5) rows.

exaggerated particularly in case of PS_4-PI_4 (60k-120k) because of the high molecular weight of the PI arms.

To confirm that formation of worm-like structures is a result of fusion of spherical micelles, I imaged the morphology by vitrifying the polymer solution under cryogenic conditions. Images obtained using cryo-TEM, which are presented in Figure 4-4, clearly show that spherical micelles are formed for all six of the PS_n-PI_n star copolymers. The trend of increasing size with n, previously described based on the hydrodynamic behavior of stars, is also reflected in these images, showing the effect of chain topology on micelle structure. Consistently, micelles formed by self-assembly of the 4-arm stars are seen both on the grid as well as in the holes where solvent has been appropriately vitrified. This is mainly due to high solution concentration that was utilized for cryogenic microscopy. For the 8-arm star copolymer, large, well-separated spherical micelles are seen on the grid. Evidently, both architecture and composition affect the size, but these variations do not induce any morphological change in the micelle shape.

4.4.3 Impact of architectural design and composition on solution self-assembly of miktoarm stars

By using scattering and imaging techniques, it is observed that micelle morphology remains unchanged but micelle size increases with number of arms for both symmetric and asymmetric miktoarm star copolymers. Here, I discuss the factors responsible for both of our observations.

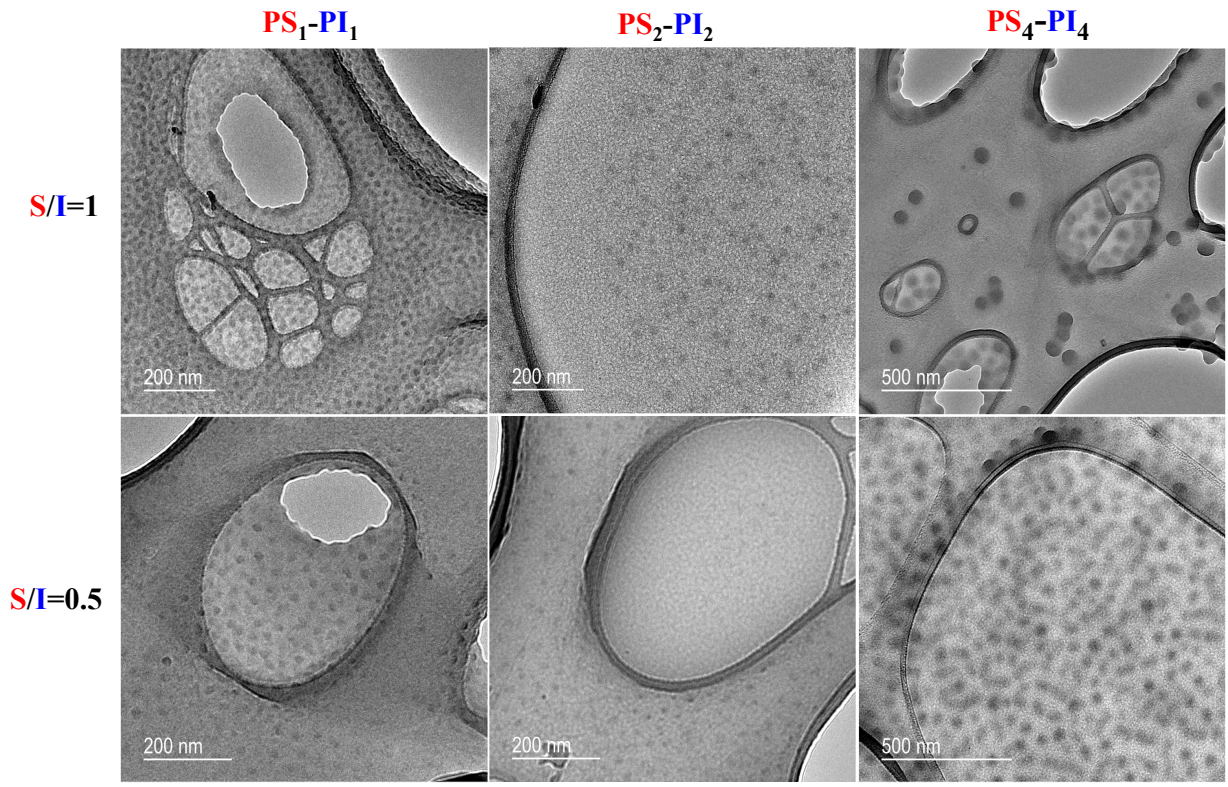


Figure 4-4. Cryogenic transmission electron microscopy (cryo-TEM) images of aggregates of PS_n-PI_n stars vitrified in n-hexane using liquid N_2 as the cryogen. The top row shows images for stars of symmetric composition (S/I = 1) and the bottom row presents images for asymmetric stars (S/I = 0.5).

Impact on micelle morphology. All of the star copolymers form spherical micelles and no structural transformation is observed as the central core becomes more crowded by introduction of more arms or by doubling PI arm sizes. There are two main contributions that prevent any morphological transformation of spheres. First, the geometric constraint on the corona-forming PI arms appears to force PI chain segments closer to the core-corona interface to be more stretched. PI stretching increases the entropic cost paid by the micellar system. Second, poor selectivity of PS for n-hexane, causes the core to remain collapsed irrespective of change in architecture and composition. This is clearly observed from the calculations where the core size remains nearly constant. Under the influence of these two factors, morphological transformation would occur only when the entropic cost due to PI stretching is compensated by changing the interfacial curvature to acquire a different micellar shape. However, due to absence of any driving force that leads to compensation of entropic penalty, acquiring a morphological shape with a more gradual curvature does not occur.

An alternate view on morphological change with number of arms is that as n increases, a change in shape is possible if it destabilizes the micellar system. Destabilization occurs only when the architecture is changed for the core block.[40] Because I used centrosymmetric stars, the core block stabilizes and the corona block stretching destabilizes the micelle structure. The net result is no change in morphology with an increase in the number of arms of both PS and PI blocks. A similar effect is shown to occur for diblock and stars in theoretical study conducted on micellization of star copolymers, where increasing the length of the soluble block resulted in no morphological transformation.[40,107]

Impact on micelle size. Changes in micelle size are observed with manipulation of macromolecular design. The size variation is primarily an effect of chain stretching closer to the interface. Consider the case of symmetric stars: With increase in the number of arms attached to the central core, the aggregation number goes down. The increase in micelle size is again a contribution of chain stretching and collapsed PS core. As an example, the 4-arm and 8-arm star copolymers are essentially composed of equivalent diblocks (two and four diblocks, respectively) stitched together at the junction point. Second, is that the PI corona arms of stars are more stretched at the interface as compared to PI arms of the diblock copolymers. This is evident in the trend of core sizes presented in Table 4-3, where the core sizes values are close for the copolymers, suggesting that chain stretching contributes significantly towards increase in micelle size. This is also reflected in the surface area per PI corona chain, *S*, calculated from the radius of the core. On comparing the diblock and 8-arm copolymers, the 8-arm stars clearly have the highest area/chain suggesting that geometric constraints enforced by the central junction point causes the PI chains to be more stretched, causing an increase in the micelle size. A similar explanation holds true for asymmetric stars, where increasing n makes the micelle size bigger.

4.5 Conclusions

The effects of molecular architecture and block composition on solution self-assembly of miktoarm star copolymers based on PS_n-PI_n were explored in a PI selective solvent, n-hexane. All of the star copolymers studied formed spherical micelles, with no morphological transformation occurring due to changes in architecture and composition of the stars. Topology constraints cause the corona-forming PI blocks to be more stretched near the core-corona

interface. The strong selectivity of the solvent prevents any possible broadening of the interface, but the size is impacted by changes in macromolecular design of the stars. The introduction of more arms attached to the central core causes the strong stretching of the PI chains, increasing the micelle size. By exploring the self-assembly of model PS_n-PI_n stars in a PI selective solvent, that these studies demonstrate design changes of architecture and composition can serve as a tool to manipulate the self-assembled structures.

Chapter 5: Utilizing Chain Entropy to Control Dispersion and Thermal Properties of Polymer Nanocomposites based on Poly(1,3-cyclohexadiene) Polymers

This chapter describes work involving characterization of polymer nanocomposite based on PCHD homopolymers. Other coauthors who contributed to the work are Priyank Shah who synthesized the materials, Balaka Barkakaty, Weiyu Wang, Bradley Lokitz, David Uhrig, Jihua Chen, Jimmy Mays and S. Michael Kilbey II, who advised the work.

5.1 Abstract

Controlling dispersion of polymer-grafted nanoparticles (PGNPs) to enhance thermal properties has been extensively studied for symmetric systems. The energetic interplay that result from strong interactions between the graft and matrix chains leads to dispersion of the NPs. In symmetric systems, in which the chemical nature of the graft and matrix polymer is the same and their flexibility is varied, chain entropy contributions become significant in controlling dispersion. In this study, I demonstrate the effect chain flexibility and molecular weight of poly(1,3-cyclohexadiene) (PCHD) has on dispersion of PCHD-grafted silica nanoparticles dispersed in a chemically identical matrices of varying flexibility. It is found that increasing the rigidity and molecular weight leads to an increased wetting of PGNPs thereby improving dispersion. This outcome successfully shows that macromolecular design parameters affecting the chain configurational entropy govern distribution of NPs and serve as an effective tool to control macroscale thermal properties of nanocomposites.

5.2 Introduction

Adding inorganic nanoparticles (NP)s to a polymer matrix is a way to improve the properties of the binary system.[14,17,50] The property enhancement is a direct result of the degree

of control one can achieve over distribution of the inorganic filler in the matrix.[17,109] Usually, dispersion is achieved by modification of the NP surface, which alleviates the strong van der Waals interactions that drive NPs to aggregate and brings in a new set of interactions between the modified NP and the matrix polymer.[108-124] Using polymer chains as the surface-modifying agent, termed a "polymer graft", is an effective way to control the distribution at larger length scales and achieve desired enhancements in properties. For example, the mechanical stiffness and thermal properties of the polymer nanocomposites have been shown to improve for several polymeric materials when NPs are successfully modified by polymer chains.[17,52,53,108-110]

Increasing the miscibility between the two phases can be achieved by utilizing both enthalpic and entropic interactions between the polymer graft and the matrix polymer.[17,52,108,109] An example of enthalpic interactions leading to wetting of bare silica nanoparticles occurs when poly(2-vinylpyridine) (P2VP) is used as the matrix. In this system dispersion occurs because of strong H-bonding interactions between silica and the P2VP matrix.[109] Grafting chains onto nanoparticles reduces attractive particle-particle interactions, providing a useful strategy for achieving a well-dispersed nanocomposite. In this approach, the graft characteristics play a key role in regulating the compatibility between the graft polymer and the matrix polymer.

For PGNPs, altering the macromolecular characteristics provides a fundamental way of generating design-dispersion-property relationships. When the polymer grafted onto the NPs is chemically identical the matrix polymer, entropic interplays dominate the wetting/dewetting of the surface-modified NPs.[109,112,113] Various factors that affect the stretching of the polymer grafts (regarded as a brush) include grafting density,[114] nanoparticle shape,[115] molecular weight, and

polydispersity.[116-119] In particular, molecular weight has a profound impact on particle wetting/dewetting. In a moderately dense grafted polymer chain, it is observed that if the graft molecular weight is greater than the matrix molecular weight, autophilicity (wetting of NPs) occurs due to entropic gain associated with mixing of the graft and the matrix chains.[109] Here, chain stretching and entropy of mixing dominate the free energy of the system because enthalpic interactions, described by the Flory-Huggins interaction parameter, are insignificant because the chemical nature of the matrix and graft polymers is the same. Therefore, it is the gain in entropy that lowers the free energy of the binary system, driving the dispersion, as long as the NP surfaces are covered by brush chains.

In flexible systems, changes in graft chain conformation in the matrix environment are a significant factor influencing wetting/dewetting behavior. These changes in conformation are due to the ability of flexible polymers to adapt multiple conformations. In case of semiflexible polymers, the persistence length reduces the conformational freedom of the chain and the role of chain anisotropy becomes significant when the graft and matrix polymers differ in their flexibility.[53,120,121] A number of investigations have been focused on understanding the role semiflexible polymers play near interfaces and composites.[53,120-123] In composites containing bare nanoparticles and semiflexible polymers, persistence length effects due to conformational restrictions in the polymer chain strongly affect the wetting/dewetting behavior.[108,120-123]

In a recent simulation conducted by Jayaraman and coworkers,[53] importance of graft and matrix flexibility on dispersion was highlighted. Specifically, their study of systems where the matrix and graft were chemically identical pointed out that reducing the flexibility of the graft

led to more a dispersed state in comparison to reducing the flexibility of the matrix polymer. Using a coarse-grained model, wetting behavior was understood by comparing the concentration profile of segments of the matrix chains in the brush, and it was found that reductions in graft flexibility lead to increased wetting by matrix chains. This condition arises out of a critical balance between the gain in mixing entropy and losses in conformational entropy upon wetting. When the situation is reversed (matrix flexibility is decreased), conformational entropy loses of the matrix are not found to be as significant in comparison to changes in the flexibility of the grafted chains. This study clearly brings out the importance of entropic contributions arising out of the intrinsic nature of the semiflexible chain. However, this concept needs experimental validation, which can be achieved only when the flexibility of matrix and graft polymer can be tuned without varying the monomer type.[53] Understanding and experimentally verifying the role entropy plays in the spatial arrangement of nanoparticles in a polymer matrix is the motivation for this study.

In this study, I attempt to understand the role chain flexibility plays on dispersion by utilizing PCHD-based polymers, whose chain flexibility can be altered without changing the monomer type. For this work, flexibility of both the graft and matrix polymer was varied. For the grafted polymers, two different chain microstructures – 90/10 and 70/30 – are synthesized and molecular weight is varied for each microstructure. The molecular weights are chosen in such a manner they are above and below the "autophobic brush regime" discussed earlier.[109,112,113] Thus, with these studies, both the impact of graft flexibility and molecular weight on dispersion can be examined. Further, in order to understand the impact of matrix flexibility, same two microstructures are synthesized and their molecular weights are chosen such that they are in

between the molecular weights of the graft chains. Also, I extend the spectrum of matrices by using polystyrene, a flexible polymer, of two different molecular weights. To evaluate dispersion and its impact on thermal properties, transmission electron microscopy (TEM) and differential scanning calorimetry (DSC) were used.

5.3 Experimental Section

5.3.1 Synthesis of poly(1,3-cyclohexadiene) (PCHD)-$SiCl_3$ end-capped polymer with different chain microstructures

The materials for this project were obtained from the Mays group and synthesized by Dr. Priyank Shah. The poly(1,3-cyclohexadiene) end-capped with $SiCl_3$ was synthesized by anionic polymerization using the break-seal technique as follows: In a typical procedure, ~75 mL of dry benzene was transferred to a polymerization reactor by in-distillation. To this polymerization flask, a known quantity of the initiator, n-butyllithium (2.68 mmol) was introduced through a break-seal from an ampoule, followed by addition of the additive needed to achieve a targeted chain microstructure. In the case of synthesizing chains with 70/30 microstructure, DME (0.63 g, 6.99 mmol) was added at 0-5 °C. For PCHD with 90/10 chain microstructure, the additive DABCO was added at 20 °C. The polymerization was initiated by adding monomer 1,3-cyclohexadiene (10.6 g, 132.2 mmol) to the mixture of initiator and additive, and stirred for 6 h. For end-capping the PCHD with silyl chloride, silicon tetrachloride, $SiCl_4$ (2.55 g, 40.2 mmol) was introduced while the solution is being rapidly stirred. After allowing the reaction to procede for an hour, excess end-capping agent, $SiCl_4$ was distilled from the polymerization solution along with benzene. Previously, dried benzene was introduced to the polymerization flask to redissolve

the end-capped PCHD and the polymers were ampoulized and stored in a refrigerator. In case of synthesis of the matrix polymer PCHD without the silyl chloride end-cap, the reaction was terminated using dry methanol such that the carbanionic chain end abstracts a hydrogen atom, forming H-terminated PCHD. The molecular characteristics of the graft and matrix PCHD polymers are summarized in Table 5-1.

Table 5-1. Summary of molecular characteristics of the graft (G) and matrix (M) homopolymers of PCHD and PS.

Sample ID		Chain microstructure	SEC molecular weight M_n (kg mol^{-1})	PDI
1G	Graft PCHD-$SiCl_3$	90.10	5.5	1.10
2G		90.10	20	1.21
3G		70.30	3.5	1.10
4G		70.30	14	1.20
1M	Matrix PCHD-H	90.10	10	1.13
2M		70.30	11	1.15
3M	Matrix PS	-	2	1.06
4M		-	8	1.05

5.3.2 Grafting-to of PCHD-$SiCl_3$ onto bare silica nanoparticles

The $SiCl_3$ end-capped PCHDs were obtained in vacuum-sealed ampoules. Because I had a limited number of PCHD-$SiCl_3$ ampoules, the grafting reaction was attempted only once. Therefore, this study does not address the effect of grafting density on dispersion. Also, the trichlorosilanes are very sensitive to moisture. For the grafting reaction, a procedure similar to those used to graft alkyl silanes on silica NPs available in literature was followed. Because the silane reaction is very sensitive to moisture, the solutions were transferred inside a glove box with O_2 content of <0.5 ppm and H_2O content of <1.5 ppm. About 16 mL of 14 nm silica particles in MEK (obtained from Nissan Chemicals), were transferred to previously-dried 3-neck 250 mL flask containing a stir bar. 50 mL of anhydrous THF was transferred to the flask. After this addition, the ampoule containing PCHD-$SiCl_3$ in benzene was broken and its contents were transferred completely to the flask. The 3-arm flask was immediately sealed with rubber septa and connected to a reflux condenser. The contents of the flask were refluxed at 75°C and stirred for 24 h. After this time, the solution was centrifuged at 8000 rpm for 20 mins to recover the silica nanoparticles. The nanoparticles were redispersed in THF to remove any excess unreacted PCHD. This process was repeated three times to ensure removal of any adsorbed (non-grafted) polymer chains. The PCHD-grafted nanoparticles were dried under vacuum at ambient temperature for 24 h.

5.3.3 Preparation of 5 wt % polymer nanocomposites (PNCs)

To prepare the binary blend, PCHD-grafted Si NPs were mixed with matrix polymer at 5 wt % and dissolved in THF. The solution was allowed to stir for 48 hours for uniform

distribution of PCHD-grafted Si NPs in the matrix. The resultant blend solution was used to prepare samples for TEM and nanocomposite samples for thermal analysis. Different blends were prepared by varying the matrix polymer for a given PGNP to obtain sixteen different type of nanocomposites blend.

5.3.4 Characterization of nanocomposite blends

Nanocomposite blends in solid form were obtained by depositing 5 wt % PGNP/matrix solution in a clean glass vial. Characterization of the nanocomposites was carried out before and after annealing under vacuum for 24 h at 150 ˚C. To anneal the samples, the vacuum oven was flushed thrice with nitrogen and evacuated to remove air before starting the process of thermal annealing. Both the TEM grids and solid blend samples were subjected to annealing, and a total of 32 samples were investigated in this study.

Differential scanning calorimetry. The glass transition temperature of each of the polymer nanocomposites (PNCs) was measured using a TA Instruments Q2000 differential scanning calorimeter (DSC). A small amount of PNC, approximately 3–5 mg, was weighed in a standard DSC pan using a microbalance and then sealed with a lid. Each sample was subjected to two heat–cool cycles, using the first cycle to erase the thermal history of the sample. On the first cycle, the temperature is lowered to -40 °C, ramped to 200 °C at a heating rate of 20 °C min^{-1}, and then lowered to 0 °C at a rate of 20 °C min^{-1}, where it is held for 10 min before commencing the second cycle. On the second cycle, the sample is heated to 200 °C at a rate of 10 °C min^{-1} and then lowered to 25 °C at a rate of 10 °C min^{-1}. The glass transition temperature (T_g) of the sample was calculated using TA Instruments supplied Universal Analysis software. T_g values

were taken to be midpoint of the curve between the extrapolated lines that define the baselines of the rubbery and the glassy regions of the second heating curve. The T_g values for all sixteen PNC samples before and after annealing are summarized in Table 5-2.

Transmission electron microscopy. TEM images were acquired using a Zeiss Libra 120 MC transmission electron microscope that is equipped with a Gatan UltraScan US1000XP CCD camera. To prepare a sample for TEM, a drop of the PNC solution was drop cast onto a 400 mesh size carbon film grid. Excess fluid was blotted with a filter paper before the grid was allowed to dry in air. The sample grid was mounted on Gatan 915 double tilt holder with help of a copper anti-twist washer and a Beryllium hex ring and then introduced into the column and imaged with a 16X magnification with a scale bar of 100 nm.

5.4 Results and Discussion

In this study, the effect of altering the chain flexibility of both the graft and matrix polymers on dispersion of PCHD-grafted silica nanoparticles is examined. TEM and DSC were used to visualize the dispersion state and measure the glass transition temperatures, respectively. Here, the entropic changes associated due to mixing/demixing of PGNPs and the matrix are discussed.

5.4.1 Effect of chain microstructure (flexibility) and molecular weight on glass transition temperatures of the polymer nanocomposites

As seen from Table 5-2, all the PNC blends show an increase in glass transition temperature after thermal annealing for 24 h under vacuum. This can be attributed to local

Table 5-2. Thermal properties of PCHD-grafted polymer nanocomposites before and after 24 h of thermal annealing.

PNC Sample ID	Grafted-NP + matrix polymer[a]		T_g (˚C) before annealing	T_g (˚C) 24h annealing[b]
C1	1G + 1M	90/10 5.5k + 90/10 10k	101	118
C2	1G + 2M	90/10 5.5k + 70/30 10k	123	139
C3	1G + 3M	90/10 5.5k + PS 2k	36	46
C4	1G + 4M	90/10 5.5k + PS 8k	86	95
C5	2G + 1M	90/10 20k + 90/10 10k	111	134
C6	2G + 2M	90/10 20k + 70/30 10k	116	146
C7	2G + 3M	90/10 20k + PS 2k	38	57

Table 5-2 continued.

PNC Sample ID	Grafted-NP + matrix polymer[a]		T_g ˚C Before annealing	T_g ˚C 24h annealing[b]
C8	2G + 4M	90/10 20k + PS 8k	34	96
C9	3G + 1M	70/30 3.5k + 90/10 10k	107	131
C10	3G + 2M	70/30 3.5k + 70/30 10k	133	144
C11	3G + 3M	70/30 3.5k + PS 2k	46	56
C12	3G + 4M	70/30 3.5k + PS 8k	90	96
C13	4G + 1M	70/30 14k + 90/10 10k	111	125

Table 5-2 continued.

PNC Sample ID	Grafted-NP + matrix polymer[a]		T_g ˚C Before annealing	T_g ˚C 24h annealing[b]
C14	4G + 2M	70/30 14k + 70/30 10k	120	145
C15	4G + 3M	70/30 14k + PS 2k	52	56
C16	4G + 4M	70/30 14k + PS 8k	84	125

[a] Refer to Table 5-1 for characteristics of graft (G) and matrix (M) polymer. [b] Nanocomposites were annealed under vacuum at 150 ˚C

reorganization of nanoparticles in the matrix after thermal annealing as there is less free volume, and a higher temperature is need to cause the phase transition from rubbery state to a glassy state.

When the matrix rigidity is increased while holding the graft flexibility constant, an increase in T_g is observed. This is observed for nanocomposites which have PS as the matrix (more flexible) and PCHDs (more rigid), and is illustrated in case of C1 to C4, for example. Also, T_g for PNCs with PCHD as the matrix are higher, with matrices of 70/30 chain microstructure (most rigid) being higher in comparison to T_g values of PNCs made using PCHDs

of 90/10 chain microstructure as the matrix. This is observed by comparing C1 and C2. A possible reason for this could be that PGNPs in more rigid matrices, which have higher T_gs require more thermal energy to undergo the transition from glassy to rubbery states. Further, an impact of matrix molecular weight on T_g is also witnessed. In the case where PS matrices of 2 kDa and 8 kDa were used, a higher T_g is observed for the high molecular weight matrix (8 kDa) due to the dependence of T_g on molecular weight. The effect of molecular weight can be witnessed across all PNC samples in which matrix molecular weight is increased while the graft type is held fixed, and this seen by comparing PNC samples C7 and C8, C11 and C12, and C15 and C16.

When varying the graft chain flexibility and molecular weight while holding the matrix flexibility constant, an increase in T_g is witnessed once again. As an example, consider the T_g values of PNC samples C1, C5, C9 and C13. In all of these samples, the matrix is a PCHD of 90/10 chain microstructure while the graft polymers are 90/10 (C1 and C5) and 70/30 (C9 and C13) PCHDs. The impact of molecular weight on T_g is observed when graft molecular weight is increased: Comparing samples C1 and C7 (M_n of graft < M_n of matrix) along with C5 and C13 (M_n of graft > M_n of matrix) shows that a higher T_g is observed for 90/10 (less rigid) than for 70/30 (more rigid) for both molecular weights. I anticipate that more rigid graft chains result in better dispersion of PGNPs because higher entropy of mixing compensates for the loss of conformation freedom in chains of increased rigidity. As the graft becomes more flexible, the graft chain loses conformational freedom upon mixing with/wetting by matrix chains. This loss of configuration freedom is disfavored, leading to relatively more aggregated state. These behaviors were witnessed in the simulations performed by Jayaraman and coworkers.[53] In these

situations, as dispersion of the nanoparticles improves, higher T_g values are observed. Thus, in general, increasing the molecular weight of either the graft or matrix chains leads to increases in T_g values, which is in agreement with literature[53,109] Also, an increase in rigidity of both the graft and matrix polymers leads to higher T_g values as the system favors mixing (greater entropy) which compensates for any loss of conformational entropy of the grafted brush chains.

5.4.2 Nanoscale organization of polymer-grafted nanoparticles with chain flexibility and molecular weight

As seen in Figure 5-1, the nanoparticles are more distributed after annealing the PNC samples. The thermal energy supplied causes local reorganization of the nanoparticles, allowing them to equilibrate in the matrix. However, in many instances, annealing caused some unwanted changes in the grid structure, so oftentimes I make comparisons between "As cast" samples to provide explanations of behaviors. As an example, the reorganization upon thermal annealing can be observed for PNC samples C4, C7 and C10.

Effect of matrix flexibility on dispersion

As seen in Figure 5-2, the nanoparticles are more dispersed as flexibility of the matrix is increased for a graft of a given molecular weight and chain microstructure. This is observed for all of the samples (see Appendix B1) but to represent these results, I highlight the dispersion state of 90/10 PCHD grafted nanoparticles in matrices of increasing rigidity, including both the low and high molecular weight grafted 90/10 PCHDs. In Figure 5-2, it is clear that dispersion increases as the flexibility of the matrix decreased. This occurs because as the brush chains

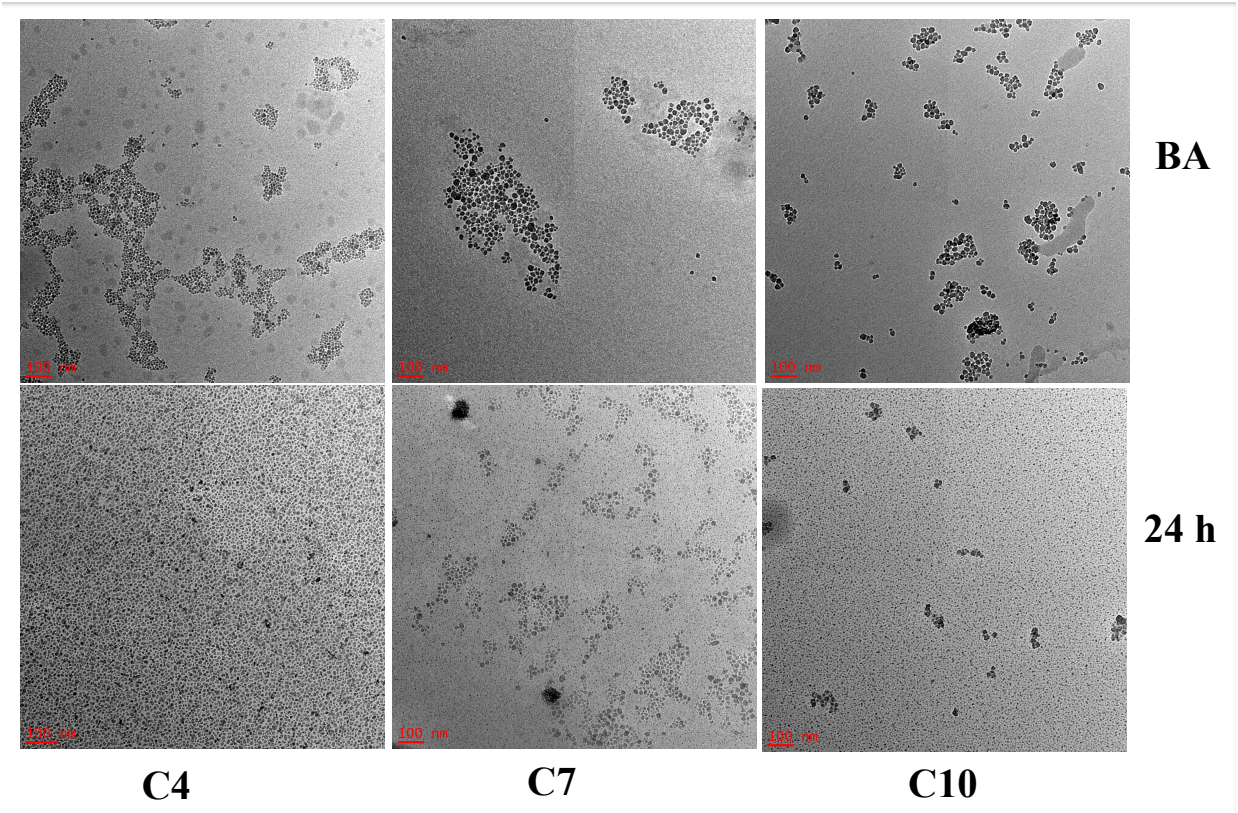


Figure 5-1. The three representative PNC sample images reflecting the local reorganization after thermal annealing for 24h. BA refers to “before annealing”. Refer to Table 5-1 for details on the make-up of PNC C4, C7 and C10.

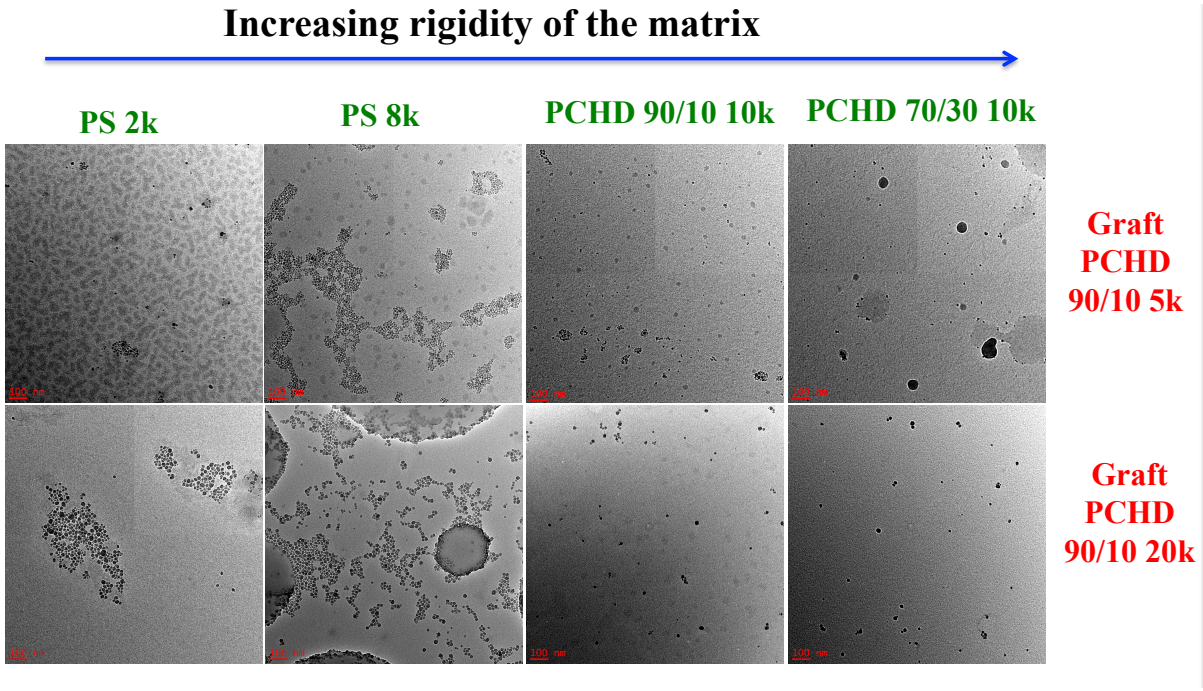


Figure 5-2. Before annealing images reflect the increase in dispersion of PCHD-grafted Si NPs in polymer matrices of increasing rigidity for a given grafted PCHD chain of 90/10 microstructure.

become stiffer, and mixing of the matrix chains in the brush-like graft chains occurs without any loss of configurational entropy of the grafted chains as matrix chains penetrate into the grafted layer. The penalty paid by these PCHD-grafted nanoparticles is reduced by wetting of the matrix chains, which results in overall entropy gain by mixing.

Effect of graft flexibility on dispersion

Similarly, when the graft flexibility (chain microstructure) is varied while keeping the matrix flexibility constant, changes in dispersion/aggregation behavior are observed. The images for NPs with the high molecular weight PCHD grafts are chosen to highlight this behavior, as this choice ensures that dispersion is favored due to the impact of molecular weight (of the matrix chains relative to the grafted chains).[109] It is seen that upon increasing the rigidity of the graft, there are profound the changes in dispersion that depend on the matrix type and molecular weight. As seen in Figure 5-3, there are basically no changes observed in dispersion when the graft rigidity is varied when PGNPs are blended with the most rigid matrix, a 70/30 PCHD matrix polymer (rightmost column of images in Figure 5-3). This may be because 70/30 PCHD chains have a sterically-hindered configuration due to kinks in the PCHD backbone, and their inability to change conformation promotes miscibility (mixing) between the brush and matrix chains. When the graft flexibility is varied with PCHD matrices of 90/10 microstructure, it is clearly seen from the images (second column from the right) that the stiffer graft (70/30 PCHD) is more miscible and nanoparticles are well dispersed. This is also observed when polystyrene matrices are used: The nanoparticles grafted with 70/30 PCHD chains polymer are better dispersed than those grafted with 90/10 PCHD chains.

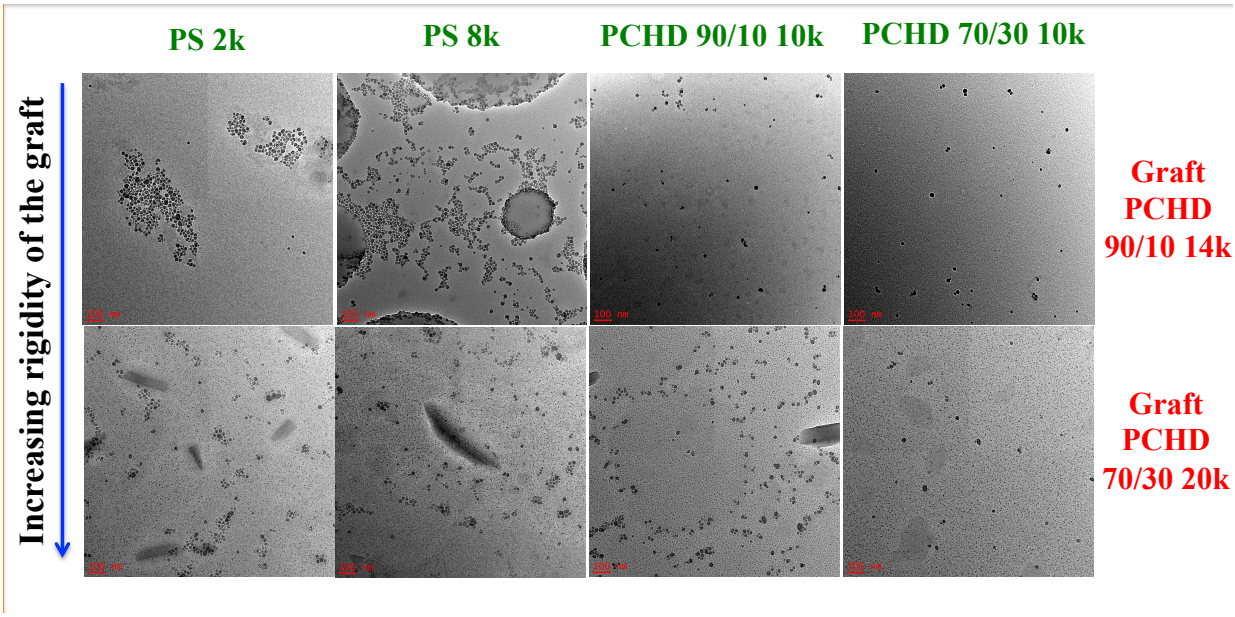


Figure 5-3. Impact of varying PCHD graft flexibility on dispersion/aggregation behavior of PCHD-grafted Si NPs in polymer matrices of different flexibility. These are images after annealing for 24 h.

Thus, increasing graft stiffness leads to improved mixing of the graft chains by matrix chains, thereby improving dispersion of the nanoparticles. These images also show that the matrix stiffness matters, as the differences in dispersion become profound when the matrix chains are more flexible. This is evident as one scans the rows of images in Figure 5-3 from left to right.

Effect of graft molecular weight on dispersion

It is well known from in the literature that when the graft molecular weight is larger than the matrix molecular weight for a chemically identical system, wetting of polymer-grafted nanoparticles is preferred. I observe a similar effect with the semiflexible systems investigated here. Presented in Figure 5-4 are TEM images of PNC samples in which the molecular weight of the grafted polymer is varied and these PGNPs are mixed with matrix polymers at opposite ends of flexibility spectrum.

In systems made with both low molecular weight PS (2k), a flexible chain, and a 10k 70/30 PCHD, better dispersion of the 70/30 PCHD-grafted Si NPs is observed with higher molecular weight grafts (M_n = 14k, bottom two images) as compared to the case when the molecular weight of the graft (M_n = 3.5k, top right images) is lower than molecular weight of the PCHD matrix (M_n = 10k). These changes in dispersion are also connected with changes in T_g discussed earlier.

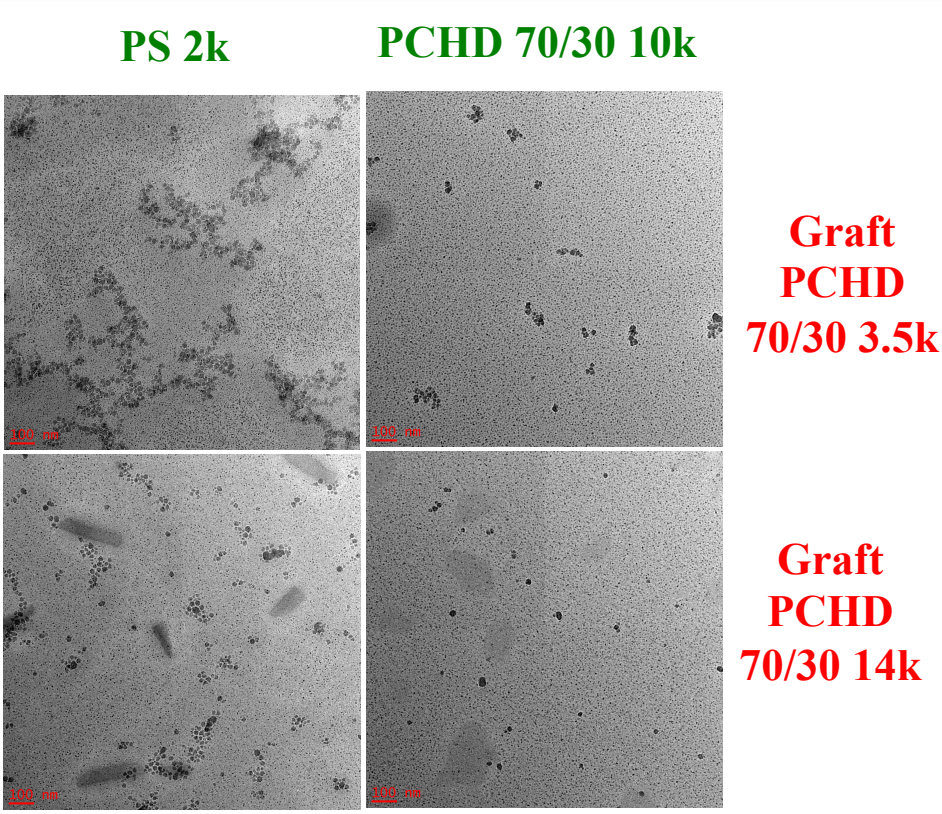


Figure 5-4. Distribution of 70/30 PCHD-grafted Si nanoparticles in matrices at two extremes in chain stiffness. PS is generally considered to be flexible, while 70/30 PCHD is semiflexible. These images show that PCHD graft molecular weight impacts dispersion/aggregation for PNC sample annealed for 24h.

Thus, all the factors discussed above namely, rigidity of the graft chains and matrix polymer, along with the molecular weight and thermal history impact the distribution of PCHD-grafted silica nanoparticles. My observations are in agreement with simulation studies conducted by Jayaraman and coworkers.[53]

5.5 Conclusions

I show that in a chemically identical matrix, entropic factors play a crucial role in the dispersion of polymer-grafted nanoparticles. In semiflexible systems, the graft flexibility has a profound impact on both dispersion and thermal properties. The tendency for dispersion can be attributed to a gain in entropy upon mixing which is favored because the conformational entropic penalty associated with the semiflexible grafted polymer chains is reduced by the fact that they have fewer conformational states. It was also proven experimentally that molecular weight of the graft and matrix polymers have an impact on dispersion. Moreover, thermal properties are impacted by all of the parameters evaluated in this study. This investigation is very significant as it has shown that variations in macromolecular design impact macroscale properties due to nanoscale organization. These fundamental studies of polymer nanocomposites provide new insights into how the interplay between matrix and graft flexibility and their molecular weights can be used to alter macroscale properties and dispersion.

Chapter 6: Summary, Conclusions and Future Work

6.1 Summary and Conclusions

The properties of the 3D structures formed by self-assembly of block copolymers has been harnessed for various technological applications. The ease of fabrication of desired 3D structures which are controllable through macromolecular design makes application of self-assembly processes an attractive tool for various applications. However, with advances in synthetic techniques and introduction of new monomer chemistries to the current arsenal of well-known soft materials, understanding and applying these principles on an individual basis remains a significant challenge. Therefore, my dissertation work has focused on linking macromolecular design parameters with structure-property relationships. For the work, hydrocarbon-based block copolymers were used which bring out the impact of weak interactions on self-assembly properties in solution and in nanocomposites.

This dissertation covered some of the most pressing questions related to the roles of polymer chain flexibility, branching and compositional asymmetry on self-assembly of diblock and miktoarm star copolymers. In this work, linear diblock copolymers of polystyrene-b-poly(1,3-cyclohexadiene) (PS-b-PCHD) were used to study self-assembly properties in solution. The polymers involved were six diblock copolymers with variation in PCHD chain microstructure (tunable flexibility) and molecular weight of PCHD blocks while PS molecular weight was held constant. Further, the effect of chain flexibility was extended to understanding the principles governing the dispersion of PCHD-grafted silica nanoparticles in polymer matrices and the resultant impact on thermal properties of the binary blend. Four different end-functionalized PCHDs, including two different chain microstructures (90/10 and 70/30 PCHD-

$SiCl_3$) of two different molecular weights, were grafted onto Si nanoparticles. Blends of the PCHD grafted-Si nanoparticles were prepared in matrices of varying flexibility. Static and dynamic light scattering, atomic force microscopy, and cryogenic and regular transmission electron microscopy with modifications to suit each polymer system, were used to examine self-assembled structures in solution and evaluate dispersion of nanoparticles in polymer nanocomposites.

The role of flexibility on chain packing was studied on a series of PS-b-PCHD copolymers in THF, a solvent slightly selective for PS. The microstructure of PCHD was varied using synthetic techniques involving additives during anionic polymerization that lead to changes in the ratio of 1,4/1,2 linkages in the PCHD backbone. This ability to alter chain rigidity without changing the chemical type, is reflected by the increase in glass transition temperatures, T_g. Investigating solution properties by using light scattering led to the understanding of how microstructure affects the ability of the PS-b-PCHD diblock copolymers to self-assemble. PS-b-PCHDs with 90/10 microstructural ratio form spherical micelles, while 70/30 and 50/50 microstructural ratios exist as single chains and ill-defined aggregates, respectively. My reasoning behind this observation is based on the premise that variations in chain microstructure lead to packing differences, which arise due to the chain configuration (rigidity). Only chains of 90/10 microstructure formed spherical micelles and I attribute this to the rod-like nature of 90/10. The rod-like chain configuration enables packing of PCHD blocks in a fashion that reduces the defect energy and compensates for the entropic penalty paid by the extended PS corona chains (due to solvent selectivity) and creation of an interface between the blocks. This work brings out the subtlety and critical importance of polymer chain packing on self-assembly.

In absence of other known factors, such as solvent selectivity, chain packing acts as a strong driving force for micellization. Further, this study brought out the concept of rigidity in a different perspective: The fact that 90/10 has the lowest glass transition temperature (least rigid) while adapting a rod-like configuration portrays that configuration and chain conformation typically described by Kuhn segment model of rigidity, can act as two different intrinsic chain parameters that govern polymer chain rigidity.

The second study involved examining the effects of macromolecular architecture and block composition on self-assembly of miktoarm star copolymers. These stars based on polystyrene-polyisoprene (PS-PI) were explored in PI selective solvent, n-hexane, and solution properties were determined using dynamic and static light scattering techniques. The main highlight of the study was that no morphological changes occur with changes in polymer design, although changes in spherical micelle size were witnessed with change in branching and composition. Here, light scattering served as critical tool in understanding the arrangement of chains and stretching of the PI corona blocks near the interface. The topological constraints due to branching and composition affects stretching and arrangement of the chains at the interface, with morphology remaining unaffected while chain stretching and arrangement influencing the aggregation number. Through a systematic study of six miktoarm stars, it was demonstrated that design changes in architecture and composition can manipulate the self-assembled structures formed in solution.

The last system involves extending studies of the role of flexibility on dispersion and thermal properties of inorganic-polymer hybrid systems I showed that the interplay between

chain stiffness and mixing are critical in governing nanoparticle organization in chemically identical nanocomposites and in cases where PCHD grafts (semiflexible) were used in PS (flexible) matrices.

In summary, through my research I have studied the importance of conformational complexity in governing self-assembly of block copolymers by isolating entropic and geometric factors. Further, these factors are controllable through careful design of polymer backbone, enabling influence over properties of stiff and thermally stable soft materials. My work has been central in revealing the influence of chain packing and rigidity on physics that ultimately operate and impact the formation of self-assembled ensembles, which dictate mesoscale structure and macroscale properties.

6.2 Future Work

By generating new insights into the influence of chain flexibility on packing of chains and architecture and composition on stretching near the interface, this work has shown that are many challenges that still need to be addressed. To address these challenges and help drive the application of these soft materials, the following set of studies are recommended:

I. Because chain microstructure altered the chain flexibility of PCHD, another system where similar variations in microstructure can be induced would be beneficial for corroborating phenomenon observed with PCHDs. Further, a polymeric material with a broader range of microstructure ratios and improved solubility in a wide selection of solvents will not only facilitate imaging structures in solution (using cryo-TEM), but also allows solution

properties to be more widely varied. Also, because the molecular weight used in this work were limited (copolymers were <25 kDa), a polymer that can be synthesized to high molecular weight polymer would strengthen the understandings of the relationship between molecular weight and rigidity. Also, because the synthesis of PCHD is arduous, a polymer where a library of homopolymer microstructures and molecular weights can be synthesized would be helpful so that the Kuhn segment length can be determined. This would be useful to verify my claims of the molecular models introduced for PCHD in Chapter 3. In a different approach, packing differences between PCHDs of different microstructure should be evaluated as thin films. With silane end-capped PCHD polymers grafted onto silicon wafers, relationships between chain microstructure and film thickness, a parameter known to be affected by chain packing, can be studied effectively.

II. As with miktoarm star copolymers, a systematic variation in both architecture and composition was achieved during synthesis of PS-PI stars. In this study, only PI selective solvents were used for understanding phase behavior of the star copolymers in solution. Several studies have pointed out interesting morphologies for PS-PI linear diblock copolymers in PS selective solvents, such as alkyl phthalates. Thus, studies in PS-selective solvents of different selectivity (toward PS) and at different compositional asymmetries would be useful for understanding self-assembly of topologically-complex copolymers. Further, it has been shown that PS-PI diblock copolymers undergo anomalous micellization with variation of temperature. Carrying out studies of the effect of temperature on solution self-assembly of PS-PI stars would strengthen the interrelationships between temperature, architecture and composition.

III. Polymer nanocomposites based on PCHD showed clear effects due to rigidity and thermal properties were clearly affected. It would be useful to examine chain dynamics and rheological behavior of these systems. Such studies would add to the current understanding of flow behavior of rigid (semiflexible) polymers and their nanocomposites.

In total, these themes of study would further elaborate links between polymer topology, solution properties and self-assembly, including dispersion-related properties in hybrid nanocomposites. This body of work would help to advance the development of mechanically stiff and thermally stable materials for demanding or high temperature applications.

List of References

1. Hamley, I. Nanotechnology of soft materials. *Angewandte Chemie International Edition,* **2003***, 42*, 1692.
2. Ober, C. K. Persistence pays off. *Science,* **2002***, 296*, 859.
3. Whitesides, G. M. and Grzybowski, B. Self-assembly at all scales. *Science,* **2002***, 295*, 2418.
4. Tirrell, M. Modular materials by self-assembly. *AIChE Journal,* **2005***, 51*, 2386.
5. Gelain, F.; Horii, A. and Zhang, S. Designer self-assembling peptide scaffolds for 3-D tissue cell cultures and regenerative medicine. *Macromolecular Bioscience,* **2007***, 7*, 544.
6. Machado, V. G.; Baxter, P. N. W. and Lehn, J.-M. Self-assembly in self-organized inorganic systems: a view of programmed metallosupramolecular architectures. *Journal of the Brazilian Chemical Society,* **2001***, 12*, 431.
7. Ozin, G. A.; Hou, K.; Lotsch, B. V.; Cademartiri, L.; Puzzo, D. P.; Scotognella, F.; Ghadimi, A. and Thomson, J. Nanofabrication by self-assembly. *Materials Today,* **2009***, 12*, 12.
8. Darling, S. Directing the self-assembly of block copolymers. *Progress in Polymer Science,* **2007***, 32*, 1152.
9. Lodge, T. P. Block copolymers: past successes and future challenges. *Macromolecular Chemistry and Physics,* **2003***, 204*, 265.
10. Higgins, A. M. and Jones, R. A. Anisotropic spinodal dewetting as a route to self-assembly of patterned surfaces. *Nature,* **2000***, 404*, 476.
11. Albert, J. N. and Epps, T. H. Self-assembly of block copolymer thin films. *Materials Today,* **2010***, 13*, 24.
12. Yang, X.; Wan, L.; Xiao, S.; Xu, Y. and Weller, D. K. Directed block copolymer assembly assembly versus electron beam lithography for bit-patterned media with areal density of 1 Terabit/inch^2 and beyond. *ACS Nano,* **2009***, 3*, 1844.

13. Stoykovich, M. P. and Nealey, P. F. Block copolymers and conventional lithography. *Materials Today,* **2006***, 9*, 20.

14. Jones, R. A. Polymer interfaces and the molecular basis of adhesion. *Current Opinion in Solid State and Materials Science,* **1997***, 2*, 673.

15. Holdcroft, S. Patterning pi-conjugated polymers. *Advanced Materials,* **2001***, 13*, 1753.

16. Tsang, E. M.; Zhang, Z.; Shi, Z.; Soboleva, T. and Holdcroft, S. Considerations of macromolecular structure in the design of proton conducting polymer membranes: graft versus diblock polyelectrolytes. *Journal of the American Chemical Society,* **2007***, 129*, 15106.

17. Kumar, S. K. and Krishnamoorti, R. Nanocomposites: structure, phase behavior, and properties *Annual Review of Chemical and Biomolecular Engineering,* **2010***, 1*, 37.

18. Alexandridis, P. Amphiphilic copolymers and their applications. *Current Opinion in Colloid and Interface Science,* **1996***, 1*, 490.

19. Olsen, B. D. and Segalman, R. A. Self-assembly of rod--coil block copolymers. *Materials Science and Engineering: R: Reports,* **2008***, 62*, 37.

20. Chen, J.; Thomas, E.; Ober, C. and Hwang, S. Zigzag morphology of a polystyrene-b-poly(hexyl isocyanate) rod-coil block copolymer. *Macromolecules,* **1995***, 28*, 1688.

21. Chen, J.; Thomas, E.; Ober, C. and Mao, G. Self-assembled smectic phases in rod-coil block copolymers. *Science,* **1996***, 273*, 343.

22. Chen, X. L. and Jenekhe, S. A. Supramolecular self-assembly of three-dimensional nanostructures and microstructures: microcapsules from electroactive and photoactive rod-coil-rod triblock copolymers. *Macromolecules,* **2000***, 33*, 4610.

23. De Gans, B.; Wiegand, S.; Zubarev, E. and Stupp, I. A light scattering study of the self-assembly of dendron rod-coil molecules. *The Journal of Physical Chemistry B,* **2002***, 106*, 9730.

24. He, P.; Li, X.; Deng, M.; Chen, T. and Liang, H. Complex micelles from the self-assembly of coil-rod-coil amphiphilic triblock copolymers in selective solvents. *Soft Matter,* **2010***, 6*, 1539.

25. Jenekhe, S. A. and Chen, X. L. Self-assembled aggregates of rod-coil block copolymers and their solubilization and encapsulation of fullerenes. *Science,* **1998***, 279*, 1903.

26. Jenekhe, S. A. and Chen, X. L. Supramolecular photophysics of self-assembled block copolymers containing luminescent conjugated polymers. *The Journal of Physical Chemistry B,* **2000***, 104*, 6332.

27. Roberts, M. F. and Jenekhe, S. A. Molecular composites of rigid-rod polymers in the matrix of flexible-coil polymers. Preparation of thin-film nonlinear optical materials via soluble complexes. *Chemistry of Materials,* **1990***, 2*, 629.

28. Surin, M.; Marsitzky, D.; Grimsdale, A. C.; Müllen, K.; Lazzaroni, R. and Leclère, P. Microscopic morphology of polyfluorene-poly(ethylene oxide) block copolymers: Influence of the block ratio. *Advanced Functional Materials,* **2004***, 14*, 708.

29. Vriezema, D. M.; Hoogboom, J.; Velonia, K.; Takazawa, K.; Christianen, P.; Maan, J.; Rowan, A. E.; Nolte, R. J. Vesicles and polymerized vesicles from thiophene-containing rod--coil block copolymers. *Angewandte Chemie International Edition,* **2003***, 115*, 796.

30. Wu, J.; Pearce, E. M.; Kwei, T.; Lefebvre, A. A. and Balsara, N. P. Micelle formation of a rod-coil diblock copolymer in a solvent selective for the rod block. *Macromolecules,* **2002***, 35*, 1791.

31. Xia, Y.; Sun, Z.; Shi, T.; Chen, J.; An, L. and Jia, Y. Self-assembly of rod-terminally tethered three-armed star-shaped coil block copolymer: Investigation of the presence of the branching in the coil to the self-assembled behavior. *Polymer,* **2008***, 49*, 5596.

32. Milner, S. T. Chain architecture and asymmetry in copolymer microphases. *Macromolecules,* **1994***, 27*, 2333.

33. Davis, J. L. Solution and surface properties of architecturally and compositionally complex block copolymer and their binary mixtures. *University of Tennessee-Knoxville, University of Tennessee-Knoxville,* **2015.**

34. Riess, G. Micellization of block copolymers. *Progress in Polymer Science,* **2003***, 28*, 1107.

35. Hu, H.; Gopinadhan, M. and Osuji, C. O. Directed self-assembly of block copolymers: A tutorial review of strategies for enabling nanotechnology with soft matter. *Soft Matter,* **2014***, 10*, 3867.

36. Matsen, M. W. and Bates, F. S. Unifying Weak- and Strong-Segregation Block Copolymer Theories. *Macromolecules,* **1996***, 29*, 1091.

37. Bang, J.; Jain, S.; Li, Z.; Lodge, T. P.; Pedersen, J. S.; Kesselman, E. and Talmon, Y. Sphere, cylinder, and vesicle nanoaggregates in polystyrene-b-isoprene diblock copolymer solutions. *Macromolecules,* **2006***, 39*, 1199.

38. Kesselman, E.; Talmon, Y.; Bang, J.; Abbas, S.; Li, Z. and Lodge, T. P. Cryogenic transmission electron microscopy imaging of vesicles formed by a polystyrene-polyisoprene diblock copolymer. *Macromolecules,* **2005***, 38*, 6779.

39. Lodge, T. P.; Pudil, B. and Hanley, K. J. The full phase behavior for block copolymers in solvents of varying selectivity. *Macromolecules,* **2002***, 35*, 4707.

40. Zhulina, E. B.; Adam, M.; LaRue, I.; Sheiko, S. S. and Rubinstein, M. Diblock copolymer micelles in a dilute solution. *Macromolecules,* **2005***, 38*, 5330.

41. Pryamitsyn, V. and Ganesan, V. Self-assembly of rod--coil block copolymers. *The Journal of Chemical Physics,* **2004***, 120*, 5824.

42. Khanna, K.; Varshney, S. and Kakkar, A. Miktoarm star polymers: advances in synthesis, self-assembly, and applications. *Polymer Chemistry,* **2010***, 1*, 1171.

43. Iatrou, H.; Willner, L.; Hadjichristidis, N.; Halperin, A. and Richter, D. Aggregation phenomena of model PS/PI super-H-shaped block copolymers. Influence of the architecture. *Macromolecules,* **1996***, 29*, 581.

44. Sotiriou, K.; Nannou, A.; Velis, G. and Pispas, S. Micellization behavior of PS-(PI)-3 miktoarm star copolymers. *Macromolecules,* **2002***, 35*, 4106.

45. Hinestrosa, J. P.; Alonzo, J.; Osa, M. and Kilbey, S. M. Solution behavior of polystyrene-polyisoprene miktoarm block copolymers in a selective solvent for polyisoprene. *Macromolecules,* **2010***, 43*, 7294.

46. Hinestrosa, J. P.; Uhrig, D.; Pickel, D. L.; Mays, J. W. and Kilbey II, S. M. Hydrodynamics of polystyrene-polyisoprene miktoarm star copolymers in a selective and a non-selective solvent. *Soft Matter,* **2012***, 8*, 10061.

47. Di Cola, E.; Lefebvre, C.; Deffieux, A.; Narayanan, T. and Borsali, R. Micellar transformations of poly (styrene-b-isoprene block copolymers in selective solvents. *Soft Matter,* **2009***, 5*, 1081.

48. Voulgaris, D.; Tsitsilianis, C.; Esselink, F. and Hadziioannou, G. Polystyrene/poly (2-vinyl pyridine) heteroarm star copolymer micelles in toluene: morphology and thermodynamics. *Polymer,* **1998***, 39*, 6429.

49. Hadjichristidis, N.; Iatrou, H.; Pispas, S. and Pitsikalis, M. Anionic polymerization: high vacuum techniques. *Journal of Polymer Science Part A: Polymer Chemistry,* **2000***, 38*, 3211.
50. Zhou, F. and Huck, W. T. Surface grafted polymer brushes as ideal building blocks for "smart" surfaces. *Physical Chemistry Chemical Physics,* **2006***, 8*, 3815.
51. Roberts, M. F. and Jenekhe, S. A. Molecular composites of rigid-rod polymers in the matrix of flexible-coil polymers. Preparation of thin-film nonlinear optical materials via soluble complexes. *Chemistry of Materials,* **1990***, 2*, 629.
52. Schadler, L. S.; Kumar, S. K.; Benicewicz, B. C.; Lewis, S. L. and Harton, S. E. Designed interfaces in polymer nanocomposites: A fundamental viewpoint. *MRS Bulletin,* **2007***, 32*, 335.
53. Lin, B.; Martin, T. B. and Jayaraman, A. Decreasing polymer flexibility improves wetting and dispersion of polymer-grafted particles in a chemically identical polymer matrix. *ACS Macro Letters,* **2014***, 3*, 628.
54. Hong, K. & Mays, J. W. 1,3-cyclohexadiene polymers. 1. Anionic polymerization. *Macromolecules,* **2001***, 34*, 782.
55. Hong, K. & Mays, J. W. 1,3-Cyclohexadiene Polymers. 3. Synthesis and characterization of Poly (1,3-cyclohexadiene-block-styrene). *Macromolecules,* **2001***, 34*, 3540.
56. Natori, I. & Sato, H. Aggregation of poly (1,3-cyclohexadiene): effects of molecular weight and polymer chain structure. *Journal of Polymer Science Part B: Polymer Physics,* **2006***, 44*, 1442.
57. Kunlun Hong, M. P. & Mays, J. Thermal properties of 1,3-cyclohexadiene, Invited talk.
58. Burchard, W. Solution properties of branched macromolecules. *Advances in Polymer Science,* **1999**, 143, 113.

59. Burchard, W. Static and dynamic light scattering from branched polymers and biopolymers Light scattering from polymers. *Advances in Polymer Science,* **1983**, *43*, 1.

60. Chu, B. Laser light scattering: Basic principles and practice. *Dover Publications, Inc.,* **2007**.

61. Schärtl, W. Light scattering from polymer solutions and nanoparticle dispersions. *Springer Science & Business Media,* **2007**.

62. Russo, P. Dynamic light scattering, Louisiana State University, Baton Rouge, **2009**.

63. Provencher, S. W. CONTIN: A general purpose constrained regularization program for inverting noisy linear algebraic and integral equations. *Computer Physics Communications, North-Holland,* **1982***, 27*, 229.

64. Koppel, D. Analysis of macromolecular polydispersity in intensity correlation spectroscopy: The method of cumulants. *The Journal of Chemical Physics, AIP Publishing,* **1972***, 57*, 4814.

65. Cui, H.; Hodgdon, T. K.; Kaler, E. W.; Abezgauz, L.; Danino, D.; Lubovsky, M.; Talmon, Y. & Pochan, D. J. Elucidating the assembled structure of amphiphiles in solution via cryogenic transmission electron microscopy. *Soft Matter,* **2007***, 3*, 945.

66. Hamley, I. W. The physics of block copolymers. *Oxford University Press* **1998**, 417.

67. Whitesides, G. M.; Boncheva, M. Beyong molecules: Self-assembly of mesoscopic and macroscopic components. *Proceedings of the National Academy of Sciences,* **2002**, *99*, 4769.

68. Batrakova, E. V; Li, S; Li, Y; Alakhov, VY; Elmquist, W. F; Kabanov, A. V. Distribution kinetics of a micelle-forming block copolymer pluronic P85. *Journal of Controlled Release,* **2004**, *100*, 389.

69. Kabanov A.V.; Alakhov, V. Y. Pluronic block copolymer as novel polymer therpeutics for drug and gene delivery. *Journal of Controlled Release,* **2002**, *82*, 189.

70. Emoto, K.; Nagasaki, Y.; Iijima, M.; Kato, M.; Kataoka, K. Preparation of non-fouling

surface through the coating with core-polymerized block copolymer micelles having aldehyde-ended PEG shell. *Colloids and Surfaces B: Biointerfaces,* **2000**, *18*, 337.

71. Pitsikalis M, S.-K. E., Hadjichristidis N. Block copolymers of styrene and stearyl methacrylate. Synthesis and micellization properties in selective solvents. *Macromolecules,* **2000**, *33*, 5460.
72. Riess, G. Micellization of polystyrene-b-polyethylene oxide block copolymers. *ACS Polymer Preparation,* **1982**, *23*, 19.
73. Booth, C.; Yu, G. E.; Nace, V. M. Block copolymers of ethylene oxide and 1,2-butylene oxide. *Amsterdam: Elsevier,* **2000**, 57, 86.
74. Alexandridis, P.; Yang, L. Micellization of polyalkoxyalkylene block copolymers in formamide. *Macromolecules*, **2000**, *33*, 3382.
75. Pochan, D.; Gido, S.; Pispas, S.; Mays, J.; Ryan, A.; Fairclough, P.; Hamley, I.; Terrill, N. *Macromolecules*, **2006**, *39*, 4460.
76. Yang, L.; Alexandridis, P.; Steytler, D. C.; Kositza, M. J.; Holzwarth, J. F. Small-angle neutron scattering investigation of the temperature-aggregation behavior of block copolymer pluronic P64 in aqueous solution. *Langmuir,* **2000**, *16*, 8555.
77. Flory, P. J. Statistical thermodynamics of semiflexible chain molecules *Proceedings of the Royal Society A,* **1956**.
78. Jenkhe, S. A.; Chen, L. Self-assembly of ordered microporous materials from rod-coil block copolymers. *Science,* **1998**, *283*, 372.
79. Ray, J. G.; Naik, S. S.; Hoff, E. A.; Johnson, A. J.; Ly, J. T.; Easterling, C. P.; Patton, D. L.; Savin, D. A. Stimuli-responsive peptide-based ABA-triblock copolymers: Unique morphology transitions with pH. *Macromolecular Rapid Communications,* **2012,** *33,* 819.

80. Ray, J.; Ly, J. T.; Savin, D. Peptide-based lipid mimetics with tunable core properties via thio-alkyne chemistry. *Polymer Chemistry*, **2011**, *2*, 1536.

81. Chécot, F.; Lecommandoux, S.; Gnanou, Y.; Klok, H. A. Water-soluble stimuli-responsive vesicles from peptide-based diblock copolymers. *Angewandte Chemie International Edition,* **2002**, *41*, 8.

82. Chécot, F.; Brûlet, A.; Oberdisse, J.; Gnanou, Y.; Mondain-Monval, O.; Lecommandoux, S. Structure of polypeptide-based diblock copolymers in solution: stimuli responsive vesicles and micelles. *Langmuir*, **2005**, *21*, 4308.

83. Kukula, H.; Schlaad, H.; Antonietti, M.; Förster, S. The formation of polymer vesicles or "peptosomes" by polybutadiene-b-poly(L-glutamate) in dilute aqueous solution. *Journal of American Chemistry Society*, **2002**, *124*, 1658.

84. Rodríguez-Hernández, J.; Lecommandoux, S. Reversible inside−out micellization of pH-responsive and water-soluble vesicles based on polypeptide diblock copolymers. *Journal of American Chemistry Society*, **2005**, *127*, 2026.

85. Schilli, C.; Zhang, M.; Rizzardo, E.; Thang, S.; Chong, Y. K.; Edwards, K.; Karlson, G.; Müller, A. A new double-responsive block copolymer synthesized via RAFT polymerization: poly(*N*-isopropylacrylamide)-*block*-poly(acrylic acid). *Macromolecules*, **2004**, *37*, 7861.

86. Sedlak, M. The ionic strength dependence of the structure and dynamics of polyelectrolyte solutions as seen by light scattering: The slow mode dilemma. *The Journal of Chemical Physics*, **1996**, *105*, 10123.

87. Yun, S. I.; Terao, K.; Hong, K.; Melnichenko, Y. B.; Wignall, G. D.; Britt, P. F.; Mays, J. W. Solution properties of 1,3-cyclohexadiene polymers by laser light scattering and small-angle

neutron scattering. *Macromolecules,* **2005,** *39,* 897.

88. Paradiso, S. P; Delaney, K. T; Garcia-Cervera, C. J; Ceniceros, H. D; Fredrickson, G. H. Block copolymer self-assembly during rapid solvent evaporation: Insights into cylinder growth and stability. *ACS Macro Letters,* **2014**, *3*, 16.
89. Kim, SH; Misner, M. J; Xu, T; Kimura, M; Russell, T. P. Highly oriented and ordered arrays from block copolymers via solvent evaporation. *Advanced Materials,* **2004**, *16*, 226.
90. Hahm S. J. and Siberner, S. J. Cylinder alignment in annular structures of microphase-separated polystyrene-*b*-poly(methyl methacrylate). *Langmuir,* **2000**, *16,* 4766.
91. Hamley, I. W; Connell, S. D; Collins, S. In situ atomic force microscopy imaging of adsorbed block copolymer micelles. *Macromolecules,* **2004***, 37,* 5337.
92. Peng, B; Chu, X; Li, Y; Li, D; Chen, Y. Adsorption kinetics and stability of polyethylene oxide-*block*-polystyrene micelles on polystyrene surface. *Polymer*, **2013**, *54*, 5779.
93. Meiners, J. C; Ritzi, A; Rafailovich, M. H; Sokolov, J; Mlynek, G; Krausch, M. G. Two-dimensional micelle formation of polystyrene-poly(vinyl pyridine) diblock copolymers on mica surfaces. *Applied Physics*, **1995**, *A61*, 519.
94. Nick, L; Kindermann, A; Furmann, J. Morphological studies of spin-coated films of polystyrene-block-poly(methyl methacrylate) copolymers by atomic force microscopy. *Colloid Polymer Science*, **1994**, *272*, 367.
95. Sharabi, Z.; Martan, M.; Jagur-Grondinski, J. Stereochemistry of poly(1,3-cyclohexadienes). NMR investigation of effects due to the solvent medium and to the mechanism of polymerization. *Macromolecules*, **1982**, *15*, 1167.
96. Kataoka, K. A. Harada, A. Y. Nagasaki, Y. Block copolymer micelles for drug delivery: design, characterization and biological significance. *Advanced Drug Delivery Reviews* **2001**,

47, 113.

97. Yokoyama, M.; Miyauchi, M.; Yamada, N.; Okano, T.; Sakurai, Y.; Kataoka, K; Inoue, S. Polymer micelles as novel drug carrier: Adriamycin-conjugated polyethylene glycol)-poly(aspartic acid) block copolymer *Journal of Controlled Release,* **1990**, *11*, 269.
98. Yokoyama, M. Lnoue, S.; Kataoka, K.; Yui, N.; Sakurai, Y. Preparation of adriamycin-conjugated polyethylene glycol)-polyaspartic acid) block copolymer. A new type of polymeric anticancer agent. *Macromolecular Chemistry Rapid Communication,* **1987**, *8*, 431.
99. Yokoyama, M.; Miyauchi, M.; Yamada, N.; Okano, T.; Sakurai, Y.; Kataoka, K; Inoue, S. Characterization and anticancer activity of the micelle-forming polymeric anticancer drug Adriamycin-conjugated poly(ethylene glycol)-poly(aspartic acid) block copolymer. *Cancer Research,* **1990**, *50*, 1693.
100. Bates, F. S.; Hillmyer, M. A.; T. P. Lodge, T. P.; Bates, C. M.; Fredrickson, G. H. Multiblock polymers: Panacea or Pandora's box? *Science*, **2012**, *336,* 434.
101. Hadjichristidis, N. Pitsikalis, M.; Pispas, S.; Iatrou, H. Polymers with complex architecture by living anionic polymerization. *Chemistry Reviews,* **2001**, *101*, 3747.
102. Li, Z., Hillmyer, M. A.; Lodge, T. P. Morphologies of multicompartment micelles formed by ABC miktoarm star terpolymers. *Langmuir*, **2006**, *22*, 9409.
103. Pispas, S.; Hadjichristidis, N.; Potemkin, I.; Khokhlov, A. Effect of architecture on the micellization properties of block copolymers: A_2B miktoarm stars vs AB diblocks. *Macromolecules*, **2000,** *33,* 1741.
104. Pispas, S.; Poulos, Y.; Hadjichristidis, N. Micellization behavior of $(PS)_8(PI)_8$ miktoarm (Vergina) star copolymers. *Macromolecules*, **1998,** *31,* 4177.
105. Uhrig, D.; Mays, J. Experimental techniques in high-vacuum anionic polymerization.

Journal of Polymer Science: Part A: Polymer Chemistry, **2005**, *43*, 6179.

106. Bornani, K. R.; Wang, X.; Davis, J.; Wang, X.; Wang, W.; Hinestrosa, J. P.; Mays, J.; Kilbey, S. M. Impact of chain microstructure on solution and thin film self-assembly of PCHD-based semiflexible/flexible diblock copolymers. *Soft Matter*, **2015**, *11***,** 6509.

107. Zhulina, E. B.; Borisov, O. V. Effect of block copolymer architecture on morphology of self-assembled aggregates in solution. *ACS Macro Letters,* **2013**, *2*, 292.

108. Kumar, S. K.; Jouault, N., Benicewicz, B. and Neely, T. Nanocomposites with polymer grafted nanoparticles. *Macromolecules*, **2013**, *46*, 3199.

109. Schadler L. S.; Kumar S. K.; Benicewicz, B.; C.; Lewis, S. L.; Harton, S. E. Designed interfaces in polymer nanocomposites: a fundamental viewpoint. *MRS Bulletin,* **2007**, *32*, 335.

110. Rittigstein P.; Torkelson J. M. Polymer-nanoparticle interfacial interactions in polymer nanocomposites: confinement effects on glass transition temperature and suppression of physical aging. *Journal of Polymer Science: Part B,* **2006**, *44*, 2935.

111. Akcora, P.; Liu, H.; Kumar, S. K.; Moll, J.; Li, Y.; Benicewicz, B. C.; Schadler, L. S.; Acehan, D.; Panagiotopoulos, A. Z.; Pryamitsyn, V. and Ganesan, V. Anisotropic self-assembly of spherical polymer-grafted nanoparticles. *Nature materials*, **2009**, *8*, 354.

112. Harton S. E.; Kumar S. K. Mean-field theoretical analysis of brush-coated nanoparticle dispersion in polymer matrices. *Journal of Polymer Science: Part B,* **2008**, *46*, 351.

113. Meli L.; Arceo, A.; Green, P. F. Control of the entropic interactions and phase behavior of athermal nanoparticle/homopolymer thin film mixtures. *Soft Matter,* **2009***, 5*, 533.

114. Martin, T. B. and Jayaraman, A. Identifying the ideal characteristics of the grafted polymer chain length distribution for maximizing dispersion of polymer grafted nanoparticles in a

polymer matrix. *Macromolecules*, **2013**, *46*, 9144.

115. Trombly, D. M. and Ganesan, V. Curvature effects upon interactions of polymer-grafted nanoparticles in chemically identical polymer matrices. *The Journal of Chemical Physics*, **2010**, *133*, 154904.
116. Nair, N.; Wentzel, N. and Jayaraman, A. Effect of bidispersity in grafted chain length on grafted chain conformations and potential of mean force between polymer grafted nanoparticles in a homopolymer matrix. *The Journal of Chemical Physics*, **2011**, *134*, 194906.
117. Martin, T. B.; Dodd, P.M. and Jayaraman, A. Polydispersity for tuning the potential of mean force between polymer grafted nanoparticles in a polymer matrix. *Physical Review Letters*, **2013**, *110*, 018301.
118. Martin, T. B. and Jayaraman, A. Polydisperse homopolymer grafts stabilize dispersions of nanoparticles in a chemically identical homopolymer matrix: an integrated theory and simulation study. *Soft Matter*, **2013**, *9*, 6876.
119. Rungta, A.; Natarajan, B.; Neely, T.; Dukes, D.; Schadler, L.S. and Benicewicz, B.C. Grafting bimodal polymer brushes on nanoparticles using controlled radical polymerization. *Macromolecules*, **2012**, *45*, 9303.
120. Ganesan, V.; Khounlavong, L. and Pryamitsyn, V. Equilibrium characteristics of semiflexible polymer solutions near probe particles. *Physical Review Letters*, **2008**, *78*, 051804.
121. Padmanabhan, V.; Frischknecht, A. L. and Mackay, M.E. Effect of chain stiffness on nanoparticle segregation in polymer/nanoparticle blends near a substrate. *Macromolecular Theory and Simulations*, **2012**, *21*, 98.

122. Xu, M.; Zhao, Q.; Zhang, C.; Du, Z. and Mi, J. Integral Equation Prediction of Surface-Induced Layering Transition of Polymer Nanocomposites. *The Journal of Physical Chemistry C*, **2013**, *117*, 19409.

123. Zhang, D.; Jiang, Y.; Wen, X. and Zhang, L. Phase separation and crystallization of binary nanoparticles induced by polymer brushes. *Soft Matter*, **2013**, *9*, 1789.

Appendices

Appendix A Chapter 4: Solution Self-assembly of Polystyrene-b-Polyisoprene Miktoarm Star Copolymers: Effect of Architecture and Conformational Asymmetry

A.1 Zimm plots of PS_n-PI_n miktoarm star copolymers in n-hexane

SLS measurements were carried out as detailed in the experimental section of Chapter 4. Zimm plots were constructed using the ALV software.

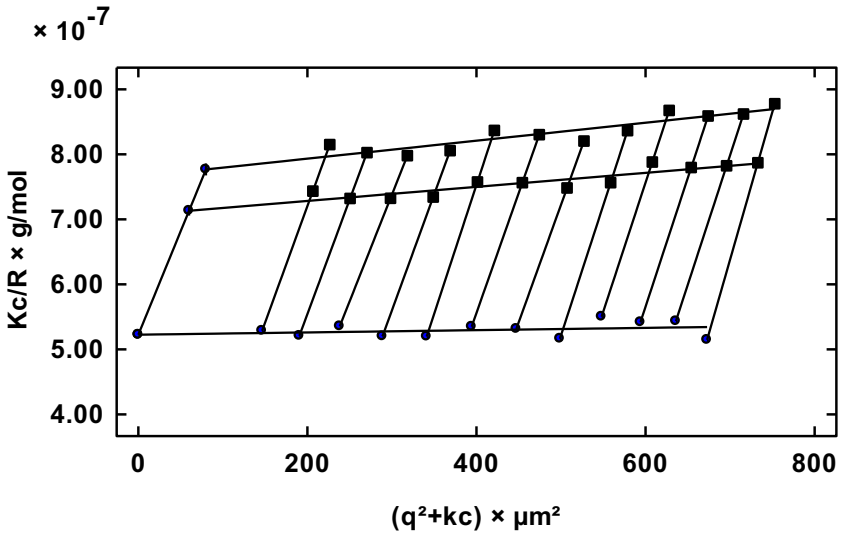


Figure A-1. Zimm plot for PS_1-PI_1 (15k-15k) in n-hexane, a selective solvent for the outer PI blocks. Measurements were made at c = 7.5 and 10.0 mg mL^{-1} and a dn/dc value of 0.181 mL g^{-1} was used in the analysis.[40] In addition to R_g and $M_{w,app}$ values reported in the dissertation, the second virial coefficient , $A_2 = 1.3\times10^{-8}$ mol dm^3 g^{-2}, was determined.

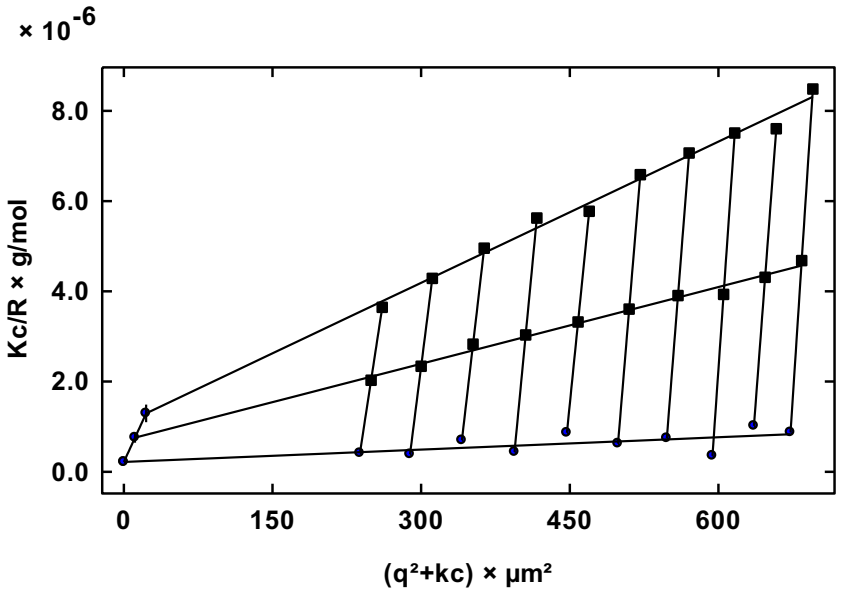


Figure A-2. Zimm plot for PS_1-PI_1 (15k-30k) in n-hexane, a selective solvent for the outer PI blocks. Measurements were made at c = 7.5 and 10.0 mg mL^{-1} and a dn/dc value of 0.185 mL g^{-1} was used in the analysis.[40] In addition to R_g and $M_{w,app}$ values reported in the dissertation, the second virial coefficient , $A_2 = 3.2\times10^{-8}$ mol dm^3 g^{-2}, was determined.

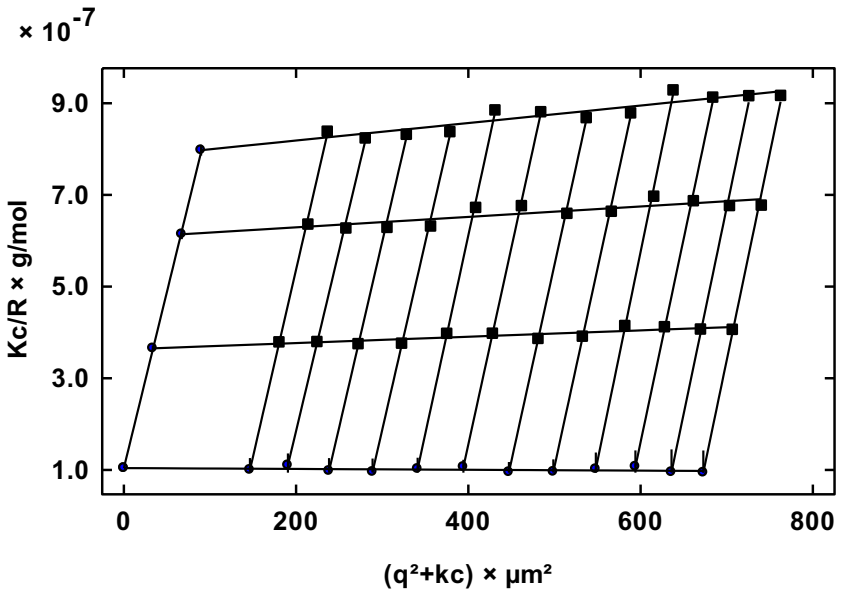


Figure A-3. Zimm plot for PS_2-PI_2 (30k-30k) in n-hexane, a selective solvent for the outer PI blocks. Measurements were made at c = 7.5, 10.0 and 15.0 mg mL^{-1} and a dn/dc value of 0.187 mL g^{-1} was used in the analysis.[40] In addition to R_g and $M_{w,app}$ values reported in the dissertation, the second virial coefficient, $A_2 = 1.7\times10^{-8}$ mol dm^3 g^{-2}, was determined.

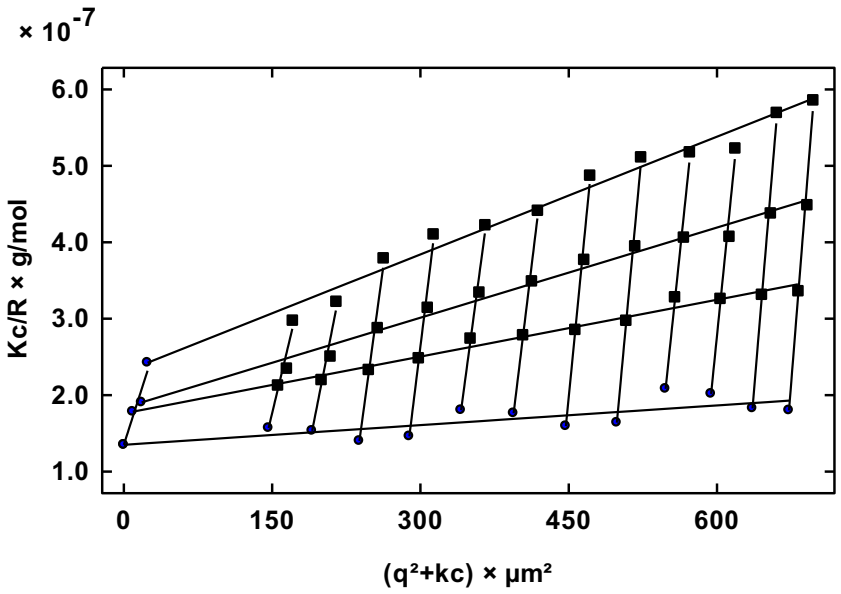


Figure A-4. Zimm plot for PS_2-PI_2 (30k-60k) in n-hexane, a selective solvent for the outer PI blocks. Measurements were made at c = 7.5, 10.0 and 15.0 mg mL^{-1} and a dn/dc value of 0.189 mL g^{-1} was used in the analysis.[40] In addition to R_g and $M_{w,app}$ values reported in the dissertation, the second virial coefficient , $A_2 = 2.3\times10^{-8}$ mol dm^3 g^{-2}, was determined.

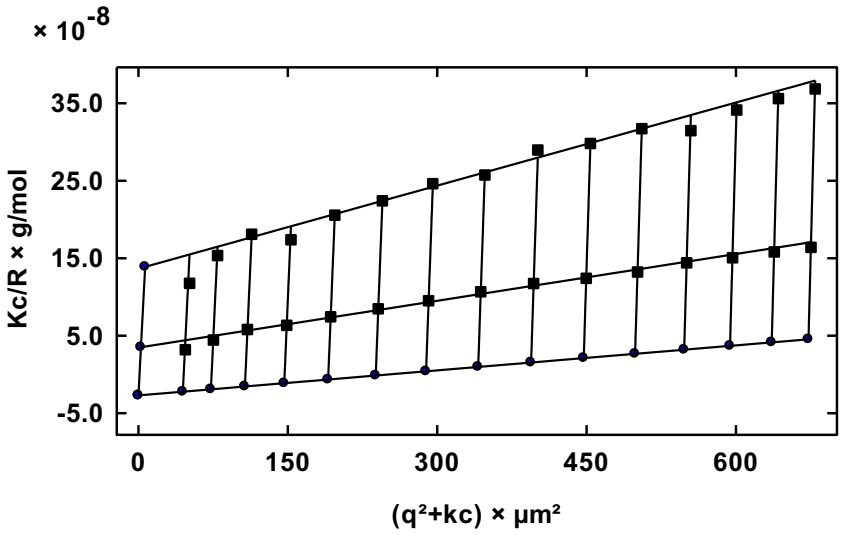


Figure A-5. Zimm plot for PS_4-PI_4 (60k-60k) in n-hexane, a selective solvent for the outer PI blocks. Measurements were made at c = 15.0 and 20.0 mg mL^{-1} and a dn/dc value of 0.195 mL g^{-1} was used in the analysis.[40] In addition to R_g and $M_{w,app}$ values reported in the dissertation, the second virial coefficient , $A_2 = 5.5\times10^{-9}$ mol dm^3 g^{-2}, was determined.

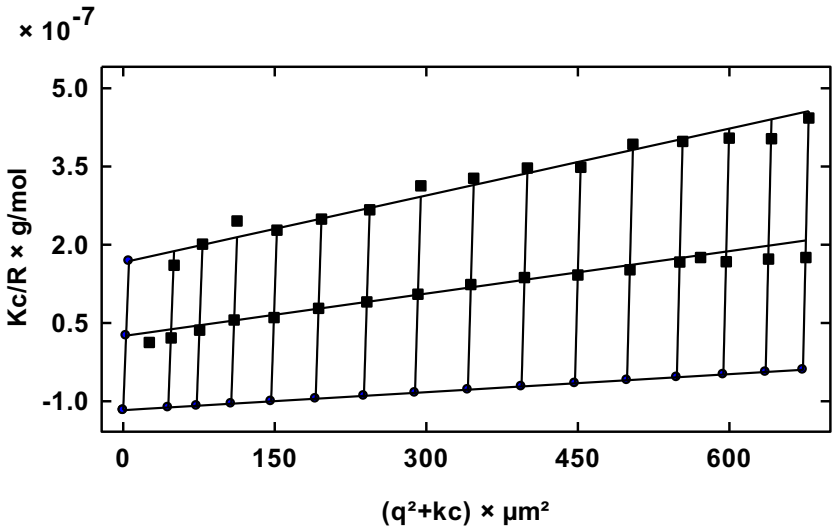


Figure A-6. Zimm plot for PS_4-PI_4 (60k-120k) in n-hexane, a selective solvent for the outer PI blocks. Measurements were made at c = 7.5 and 15.0 mg mL^{-1} and a dn/dc value of 0.196 mL g^{-1} was used in the analysis.[40] In addition to R_g and $M_{w,app}$ values reported in the dissertation, the second virial coefficient , $A_2 = 9.5\times10^{-8}$ mol dm^3 g^{-2}, was determined.

A.2 Calculation of the radius of the core, R_{core} and surface area per macromolecule, S at the interface of spherical micelles formed from PS_n-PI_n star copolymers:

Calculated values of R_{core} and S are presented in Table 4-3 of chapter 4. They were calculated based on the model of Zhulina et al. for spherical micelles.[40] An example of the calculation is presented below:

For a spherical model, aggregation number, Q, is related to the dimensionless core radius, r_3, by the following equation:[40,107]

$$Q = \frac{4\pi r_3^3 \varphi}{3N_{PS}n_{PS}} \qquad \text{(A-1)}$$

Where,

φ is the volume fraction of PS in the core,

N_{PS} is the degree of polymerization of the PS block.

n_{PS} is the number of arms of the PS block.

a_{PS} is the size of styrene monomer, which is set equal to 5.0 Å.

r_3 is the dimensionless core radius, and is equal to R_{core}/a_{PS}.

Using Q determined by analysis of static light scattering DATA allows R_{core} for the stars TO BE calculated by assuming a volume fraction of solvent in the core. This allows the area per chain, S, to be calculated by:[40,46,107]

$$S = a_{PS}^3 \frac{3N_{PS}n_{PS}}{\varphi R_{core}} \qquad \text{(A2)}$$

The values of R_{core} for various core volume fraction, φ, are presented in the Table below. For the diblocks, 4-arm and 8-arm stars, the values of n_{PS} = 1, 2 and 4, respectively are used for calculation. With monomer size of PS, a_{PS} = 5.0 Å and N_{PS} = 16900/104 = 161, calculated values of R_{core} at various φ values are presented in Table A1.

Table A-1. Summary the changes in the size of the core (R_{core} with different solvent volume fractions in the core for star copolymers in n-hexane.

Sample ID	M_w (kg mol^{-1})	R_{core} with a volume fraction, φ (nm)			
		$\varphi = 0.5$	$\varphi = 0.6$	$\varphi = 0.7$	$\varphi = 0.8$
PS_1-PI_1	15k-15k	8.5	8.0	7.2	6.7
PS_1-PI_1	15k-30k	6.4	6.0	5.4	5.1
PS_2-PI_2	30k-30k	8.8	8.2	7.5	7.0
PS_2-PI_2	30k-60k	7.8	7.3	6.7	6.2
PS_4-PI_4	60k-60k	9.4	8.9	8.0	7.5
PS_4-PI_4	60k-120k	8.8	8.3	7.5	7.0

Appendix B – Chapter 5: Utilizing Chain Entropy to Control Dispersion and Thermal Properties of Polymer Nanocomposites based on Poly(1,3-cyclohexadiene) Polymers

B.1 TEM images of PCHD-grafted silica nanoparticles before and after annealing in matrices of PCHD and PS.

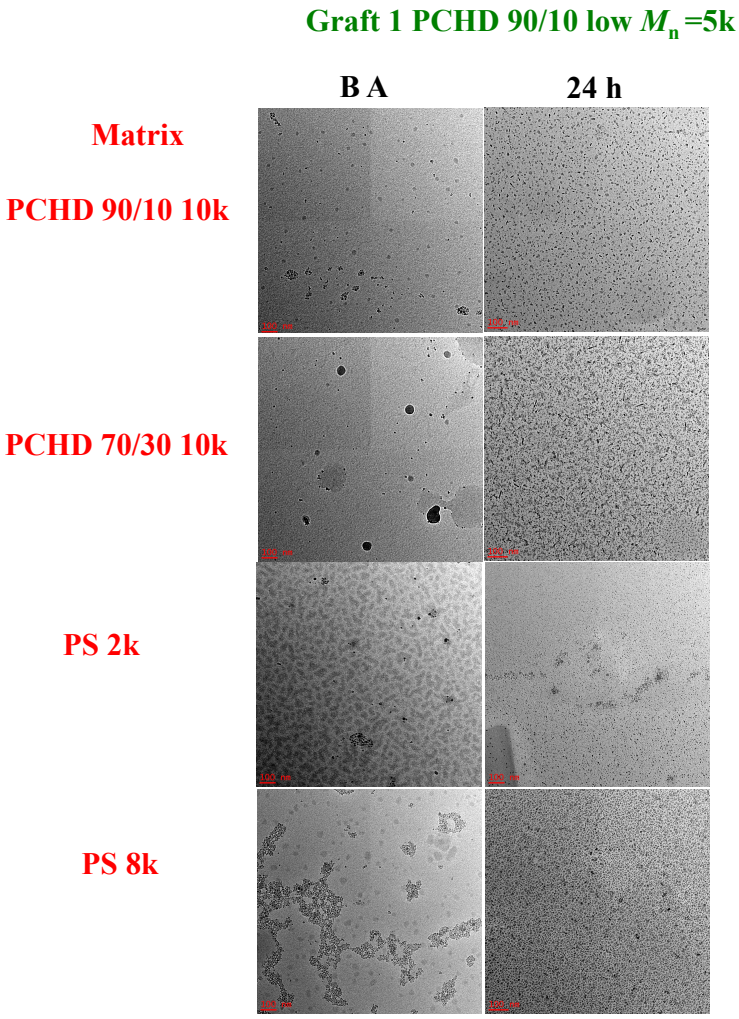


Figure B-1. Images depicting the distribution of low molecular weight PCHD-grafted Si nanoparticles (90/10 chain microstructure in matrices of varying molecular weight and flexibility. BA refers to "before annealing", and annealing was done at 150˚C for 24 h.

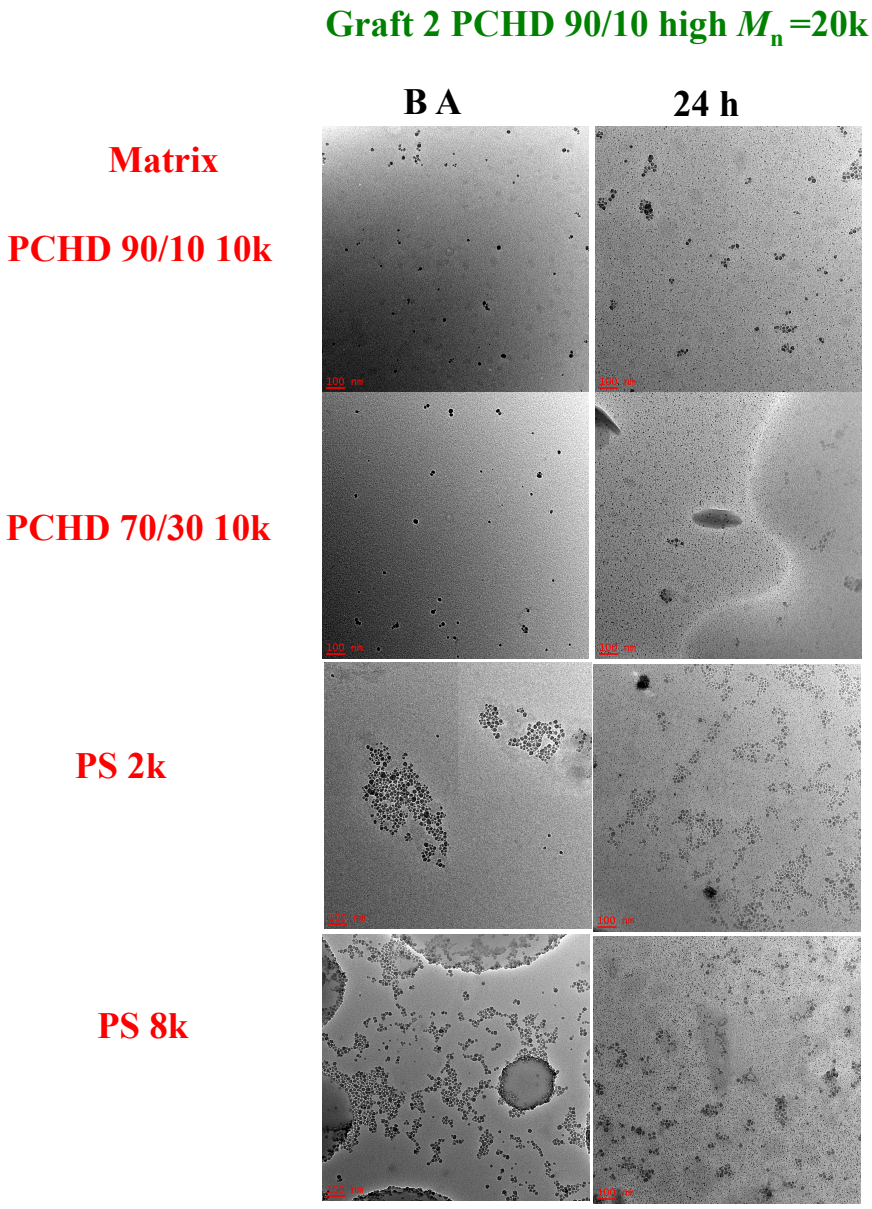


Figure B-2. Images depicting the distribution of high molecular weight PCHD-grafted Si nanoparticles (90/10 chain microstructure in matrices of varying molecular weight and flexibility. BA refers to "before annealing", and annealing was done at 150˚C for 24 h.

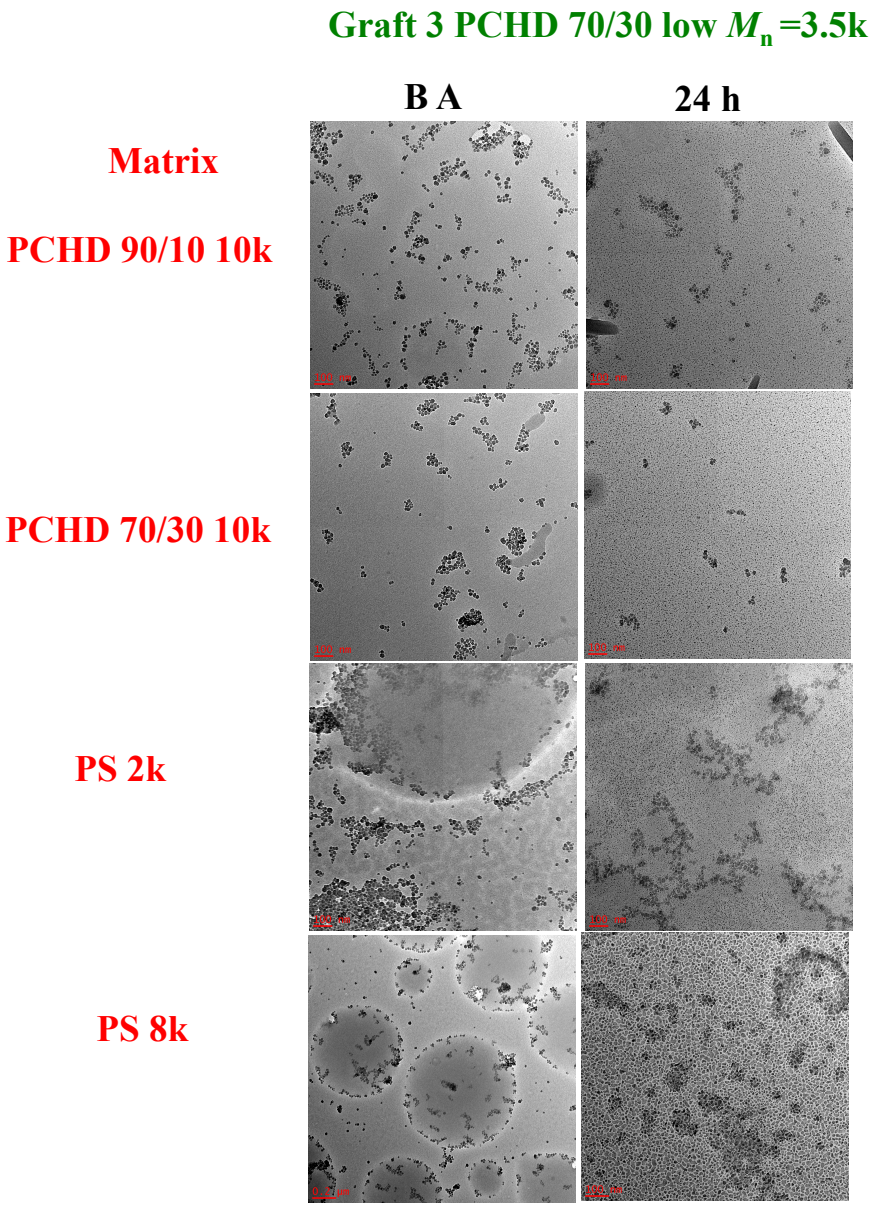


Figure B-3. Images depicting the distribution of low molecular weight PCHD-grafted Si nanoparticles (70/30 chain microstructure in matrices of varying molecular weight and flexibility. BA refers to "before annealing", and annealing was done at 150˚C for 24 h.

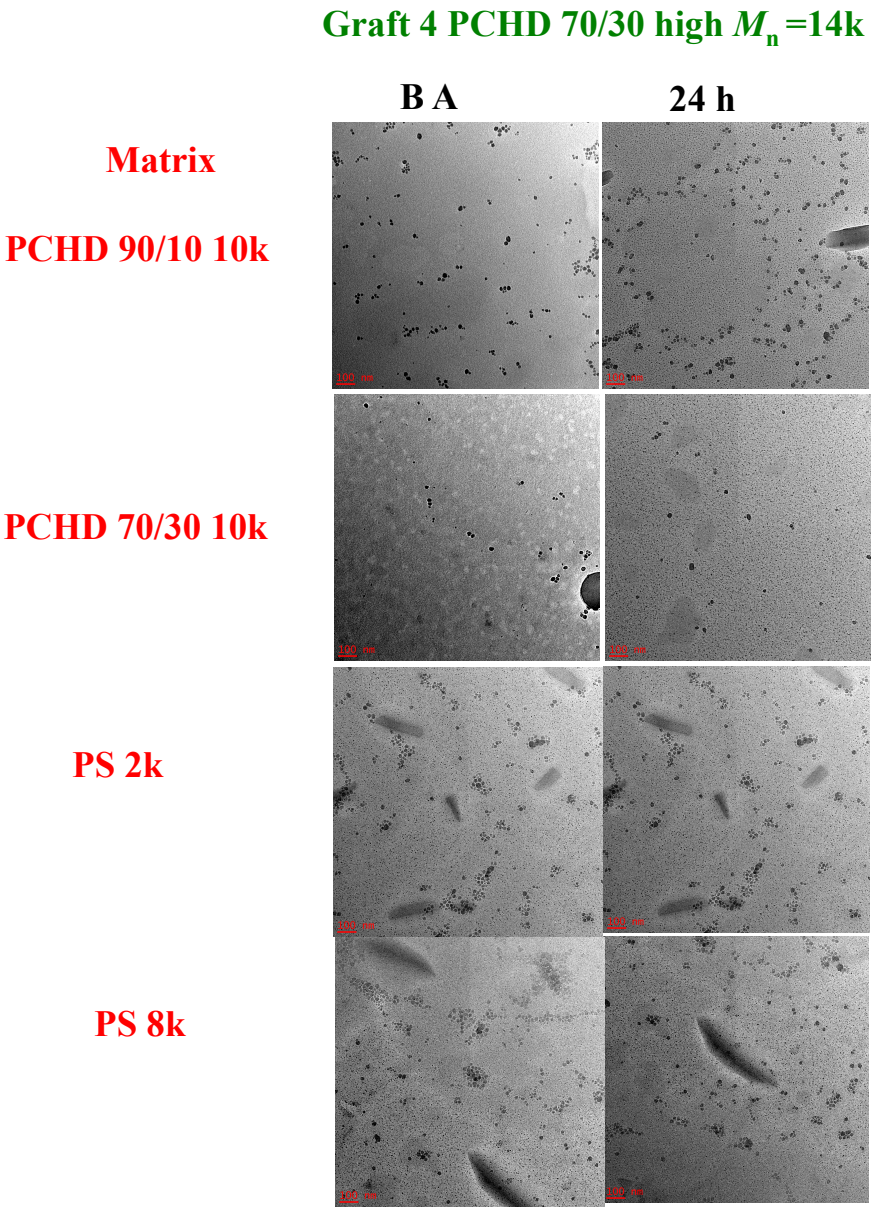


Figure B-4. Images depicting the distribution of high molecular weight PCHD-grafted Si nanoparticles (70/30 chain microstructure in matrices of varying molecular weights and flexibility. BA refers to "before annealing", and annealing was done at 150˚C for 24 h.

Vita

Kamlesh R Bornani was born and raised in the metropolitan of Mumbai, India. Kamlesh attended A. M. K. Premier School and after scoring well in SSC board exams, he was placed at G. N. Khalsa College where, he spent two years of Junior College (high school) studying science based courses. Following this, he was placed in R. N. Ruia College affiliated with Mumbai University, where his focus was studying Chemistry, Plant Science, and Microbiology. In 2008, he graduated with a major in Chemistry and scored 79% to achieve his Bachelor of Science (BSc.) degree from Mumbai University. As his interest in Chemistry grew, he continued to pursue his studies in the same department, graduating with Master of Science (MSc.) in Analytical chemistry in 2010. He aspired to take up Ph.D studies and travelled to the United States to pursue the same. At the University of Tennessee-Knoxville, under the guidance of Prof. S. Michael Kilbey II, his research focus shifted toward polymer science, where spent his time working on understanding the impact of macromolecular design on self-assembly properties of block copolymers through utilization of various characterization tools.